Theoretical and Computational Studies on Thrombus Formation and Multiphase Characteristics of Blood Flow

Submitted in partial fulfillment of the requirements for

the degree of

Doctor of Philosophy

In

Mechanical Engineering

Wei-Tao Wu

B.S., Refrigeration and Cryogenics Engineering, Xi'an Jiaotong University (2011)
M.S., Mechanical Engineering, Carnegie Mellon University (2013)

Carnegie Mellon University
Pittsburgh, PA

April, 2015

To my family

Acknowledgement

I would like to express my sincere gratitude to my advisors, Prof. James F. Antaki, Prof. Mehrdad Massoudi and Prof. Nadine Aubry. They not only gave me guidance on technical and scientific part of my study, but also shared their research philosophy, which was incredibly valuable, with me. Their rich experience in research helped me overcome various difficulties in my study.

I am grateful to my thesis committee members, Prof. Sheng Shen and Prof. Shi-Chune Yao for their valuable comments and feedback on my work. I am also very grateful that Prof. Yao and Prof. Shen provided me a lot of help and suggested me what to do when I felt confused about my life and research.

I would like to thank Dr. Fang Yang and Megan Jamiolkowski for providing experimental data for pump fluid field analysis and thrombus project. I am also indebted to Dr. Jingchun Wu for training me the skills of pump simulation, which greatly accelerated my work. I also would like to thank all members in our research group.

I also would like to express my deepest gratitude to my parents, my old brother for their generous and selfless support, and continuous encouragement. I would not be able to achieve any of these without their support.

Finally, this work was supported by NIH grant 1 R01 HL089456 and dean's fellowship.

Abstract

In this thesis several blood related problems are studied: 1. Malaria-infected, the removal of parasitized red blood cells (pRBCs) using a magnetic force; 2. A new mathematical model for thrombus growth, which incorporates the thrombus-blood interaction, shear induced platelets activation, shear induced platelets embolization and deposited platelets stabilization, is developed, and a successful direct numerical prediction of thrombus formation in an axial blood pump is obtained. According to our knowledge, this is the first time such a study has been performed ; 3. Based on the application of Mixture Theory (or Theory of Interacting Continua), a multiphase model for blood flow is derived, and a new viscosity term, which considers the effect of shear stress and volume fraction of RBCs, is introduced.

First, a blood filter system, *mPharesis*™ system, that will allow the removal of toxic malaria-infected, parasitized RBCs (pRBCs or i-RBCs) from circulation using magnetic force is studied. The problem is modeled as a multi-component flow system using CFD-DEM method, where plasma is treated as a Newtonian fluid, the RBCs and pRBCs are modeled as soft-sphere solid particles which move under the influence of the plasma, other RBCs and the magnetic field. The simulation results show that for a channel with nominal height of 100 microns the addition of upstream constriction of 80% improved the stratification by 111% (from 28% to 139%); and a downstream diffuser reduced remixing, hence improved efficiency of stratification to 260%.

Second, based on the Sorenson's model of thrombus formation [1, 2], a new mathematical model describing the process of thrombus growth is developed. In this model the blood is treated as a Newtonian fluid, and the transport and reactions of the chemical and biological species are modeled using CRD (convection-reaction-diffusion) equations. A computational fluid dynamic

(CFD) solver for the mathematical model is developed using the libraries of OpenFOAM®. Applying the CFD solver, several representative benchmark problems are studied: rapid thrombus growth in vivo by injecting Adenosine diphosphate (ADP) using iontophoretic method and thrombus growth in rectangular microchannel with crevices. Very good agreements between the numerical and the experimental results validate the model and indicate its potential to study a host of complex and practical problems in the future. Then applying the model, thrombus growth in an axial blood pump is studied. First, the flow field analysis in the blood pump is studied using visualization and numerical simulations. Then applying the thrombus model, a direct prediction of the thrombus growth is performed. The simulation shows a very good agreement with clinical observations. For reducing the computational cost, a dimensionally-reduced model is also developed, based on the complete thrombus model. The dimensionally-reduced model shows good capability to predict the thrombus deposition in blood pump as well.

And finally, for describing the multiphase characteristics of blood, using the framework of Mixture Theory, a two-fluid model is applied, where the plasma is treated as a Newtonian fluid and the red blood cells (RBCs) are treated as a shear-thinning fluid. A computational fluid dynamic (CFD) simulation incorporating the constitutive model is implemented using OpenFOAM® where benchmark problems including a sudden expansion and various driven slots and crevices are studied numerically. The numerical results exhibit good agreement with the experimental observations with respect to both the velocity field and the volume fraction distribution of the RBCs.

Contents

List of Tables

List of Figures

Chapter 1 Introduction

1.1 Motivation

In this thesis three projects are studied: 1. Simulation of malaria-infected, parasitized red blood cells (pRBCs) removal using magnetic force; 2. Development of mathematical model for thrombus growth and direct prediction of thrombus deposition in an axial blood pump; 3. Multiphase modeling of blood flow using Mixture Theory and RBCs induced platelet transport.

1.1.1Malaria infected RBCs separation

Malaria is a parasitic disease transmitted by the bite of an infected mosquito, which places an unacceptable burden on the health and economic development of billions of people across more than 100 countries. The World Health Organization (WHO) estimates that each year approximately 300 million malaria episodes occur globally resulting in nearly one million deaths, 85% of which are children under five years of age [3]. The majority of the deaths are caused by the *Plasmodium falciparum*, the most deadly of the five malaria parasite species that infect humans. These infections quickly progress to *severe malaria*, a leading cause of pediatric morbidity, hospitalization, and mortality in Sub-Saharan Africa[4, 5]. It is responsible for more than 200,000 cases of fetal loss and more than 10,000 maternal deaths annually [6]. *Severe malaria* also occurs in 5% of the nearly 30,000 imported malaria cases by travelers from endemic areas (range 1-38%) [7, 8]. Even when managed aggressively with intravenous antimalarial chemotherapies (artesunate or quinine) mortality rates remain as high as 40% for parasitic load above 20%[6, 7, 9]. Extracorporeal systems currently used to accelerate the *i-RBC* clearance *(e.g., COBE Spectra® Apheresis System, CaridianBCT)* are not engineered to

selectively separate *i-RBCs* from healthy RBCs: to remove the infected *RBCs*, 70%-95% of the healthy blood is wasted. Studies of Paul et al. [10] have shown that the malaria-infected, parasitized RBCs (pRBCs) behave like paramagnetic particles in a magnetic field. Therefore, it is possible to separate and remove the pRBCs by using a magnetic force. This is precisely the motivation for the proposed *mPharesis*™ system: that will allow the removal of toxic *i-RBCs* from circulation with minimal or no requirement of healthy blood.

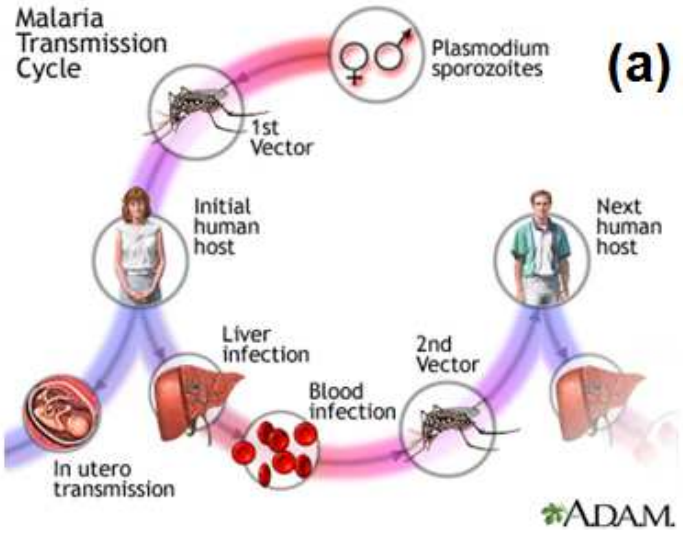

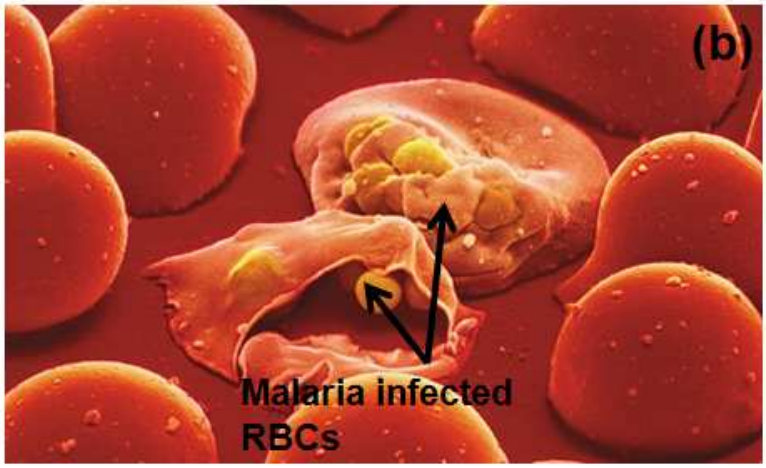

Figure 1.1 (a) Malaria transmission cycle; (b) Malaria parasites infect two blood cells.[11, 12]

1.1.2 Thrombus model development and thrombus growth in an axial blood pump

Thrombus model development

A thrombus usually refers to a blood clot anchored to damaged vascular walls. The thrombus formation in the coronary can lead to heart attacks [13-15], and the formatted thrombus can be transported to the brain by blood circulation causing cardiogenic strokes [16]. Heart attacks and strokes have been the leading cause of death in developed countries [15, 17, 18]. Thrombus generation in blood related medical devices can heavily reduce the efficiency and lead to device malfunction. For ventricular assist devices (VADs), pump thrombus is one of the main causes of morbidity, which further leads to the risk of sudden death of patients or requiring surgery to replace the device [19, 20]. In order to understand the thrombus phenomenon, and also the development of blood wetted medical devices, an accurate mathematical model for predicting thrombogenicity is urgently needed.

Figure 1.2 Infarct in the kidney of a sheep resulting from the implantation of a pediatric ventricular assist device. [21]

Thrombus growth in an axial blood pump

In the United States cardiovascular disease is the leading cause of death and claims one of every 2.6 lives. Expenditures for this disease exceed $500 billion per year.[22, 23] At end stage of cardiovascular disease, cardiac transplantation represents the only restorative therapy for the patient; however, the supply of donor organs is very limited. As a consequence, the waiting time for a transplant continues to increase and now exceeds several months.[24] Ventricular assist devices (VADs) have emerged as a salvage therapy, serving as a "bridge to transplant" by providing mechanical circulatory support until the patient can be transplanted.[25] Moreover, continuous flow pumps have been investigated by many researchers as long-term ventricular assist devices (VADs) for patients with heart failure in recent years.[26-33] However, serious complications, such as bleeding and stroke, jeopardize the quality of life of patients, and may require pump exchange or result in death due to pump thrombus (PT).

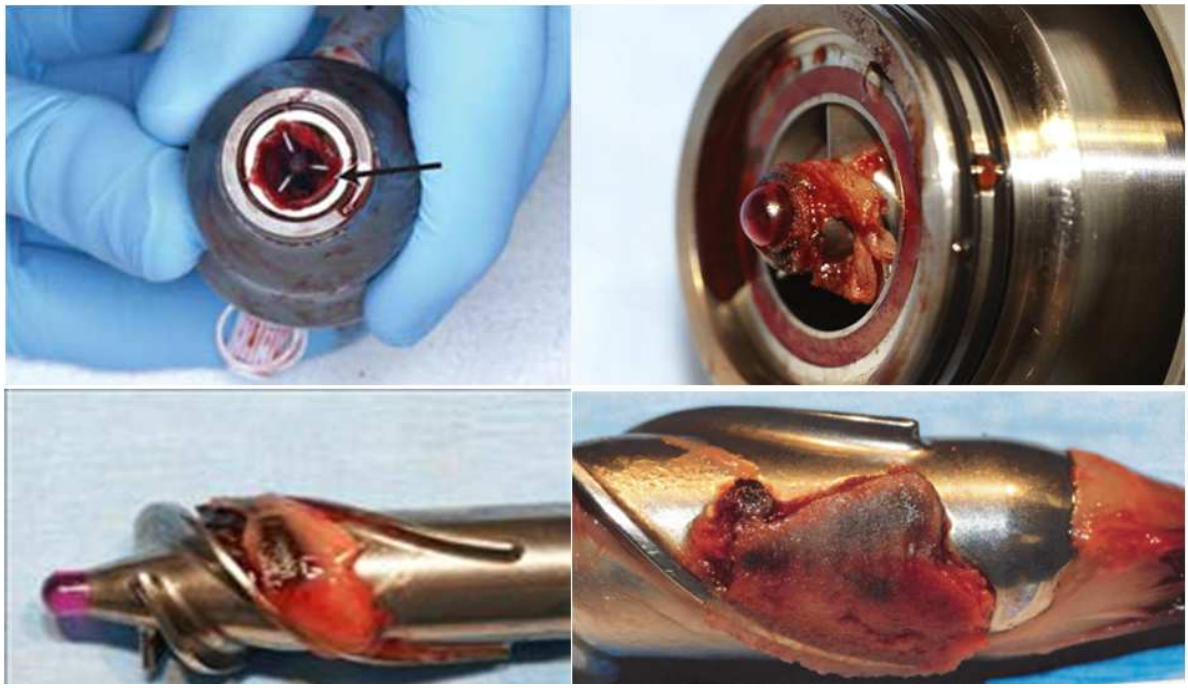

Figure 1.3 Representative thrombus in an axial blood pump. [34]

1.1.3 Multiphase modeling of blood flow

Thrombus formation procedure is closely related to various hemodynamic fields, such as shear rate, shear stress, distribution of the RBCs (red blood cells) which further influence the distribution of the platelets because of particles collision [35-39]. It is known that the thrombus initiation and growth near the walls of the vessels or the medical devices is strongly influenced by the number density of the platelets near the walls [40]. It is also well known that in blood flow, due to the complex mutual interactions between particles and plasma, such as drag and lift force, and interactions between particles, such as collisions, the RBCs tend to accumulate near the centerline of the blood vessels, called the *Fahraeus-Lindquist* effect, while the platelets tend to move away from the center of the blood vessels and accumulate near the walls of the vessels [41-43]. Through many mesoscale computational studies, the distribution of the platelets is believed to be mainly due to the collisions between the RBCs and the platelets [40, 41, 44]. Direct measurements indicate that when the RBCs are introduced, the platelet transport to vessel walls increase several hundred times [41, 45-48], which means that the multiphase characteristics of blood , such as velocity and volume fraction fields of the RBCs, have major impact on platelets distribution. This is an important factor in the cascade of events responsible for coagulation and/or thrombus. For modeling the RBCs induced platelets transportation, a multiphase model for blood flow is necessary.

Blood is a unique multi-component fluid whose composition affects the rheological properties that are responsible for its vital physiological functions. Its primary constituents are flexible, discoid red blood cells (RBCs) (approximately 45% volume fraction) suspended within essentially a Newtonian plasma [49]. In the context of blood-wetted medical devices, the trafficking of RBCs within the plasma greatly contributes to both safety and efficacy.

Accordingly the design of improved cardiovascular devices requires an accurate model of these phenomena. Conversely, the inadequacies of current models stifle our ability to design these devices with any confidence [50].

In the past several decades, investigations of blood flow in micro-scale channels have revealed several important phenomena due to the complex rheological properties of blood. In vessels with diameters ranging from approximately 0.05 to 1.5 mm, blood exhibits a thin layer adjacent to the wall that is depleted of RBCs [51]. This depletion of RBCs near the wall causes the hematocrit of branch vessels to be depleted – a phenomenon known as *plasma-skimming* [51-54]. In summary, it is evident that blood flow at micro-scale exhibits more complex behavior and acts as a multi-component material, which cannot be described by a single phase model. Motivated by the observation of the plasma-skimming phenomenon, various multiphase models for blood have been developed. The Immersed Boundary Method (IBM) combined with the Lattice Boltzmann Method (LBM) is a useful method for investigating the complex behavior of blood in micro-scale flows, particularly due to the deformation, cluster formation and collisions of the RBCs [55-57]. Although the IBM-LBM method has been very useful in displaying the complex behavior of blood, it is prohibitive for many practical problems due to its high computational cost. An alternative method consists of the so-called two-fluid or Eulerian-Eulerian two phase model [58]. In the literature, two methods based on continuum mechanics have been widely used: the Mixture Theory (or the theory of interacting continua) [59] and the Averaging Method [60]. In this work the Mixture Theory is applied as a basis for deriving a two-phase model for blood [61].

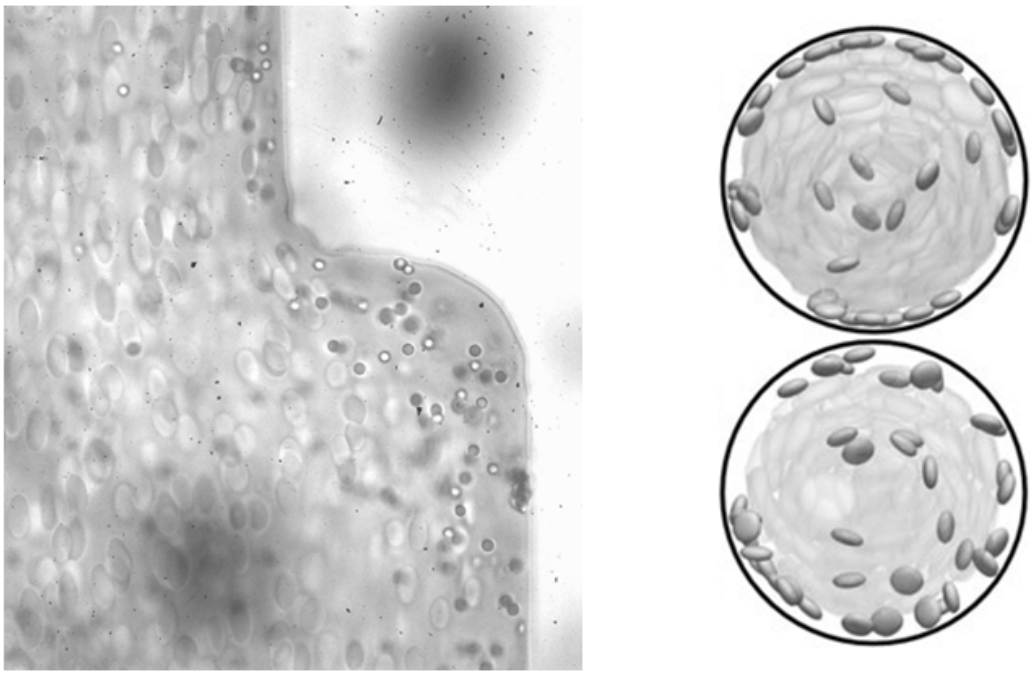

Figure 1.4 (a) Platelets non-uniform distribution in sudden expansion channel by experiment [62]; (b) Platelets non-uniform distribution in blood vessel by mesoscale simulation. [44]

1.2 Thesis overview

The thesis is organized as follows. In chapter 2, a blood filter system, *mPharesis*™ system, that will allow the removal of toxic *i-RBCs* from circulation using magnetic force is considered . The problem is studied computationally by modeling it as a multi-component flow system using CFD-DEM method. The simulation results suggest that our proposed design, a rectangular channel with a constriction and a diffuser after the constriction, highly improves the separation efficiency. In chapter 3, based on the Sorenson's model [1, 2], a mathematical model describing the process of thrombus growth is developed. Several representative benchmark problems are studied for validating the model. In chapter 4, thrombus formation in an axial blood pump is studied. Flow field analysis in the blood pump is done before applying the mathematical model developed in chapter 3, in order to predict the thrombus growth in blood pump . For reducing the

computational cost, a dimensionally-reduced thrombus model is developed, based on the complete model developed in chapter 3. In chapter 5, using the framework of mixture theory a multiphase model for blood flow is developed. Finally, a summary of this thesis work and a future work plans are presented in Chapter 6.

Chapter 2 Optimization of microfluidic channels for magnetic separation of malaria-infected red blood cells

2.1 Introduction

Malaria afflicts 300 to 500 million people worldwide and consumes 40% of the health expenditures of over 100 countries. The proposed *mPharesis*™ system allows the removal of toxic *i-RBCs* from circulation with minimal or no requirement of donor blood.

In the mPharesis™ (magnetic aphaeresis) system the patient's peripheral blood is continuously withdrawn, purified, and returned to the circulation (Figure 2.1 top). The design of the mPharesis™ filter features a series of cascaded laminar flow channels (Figure 2.1 bottom) through which the infected blood is transported and exposed to a high magnetic field gradient (>1000 T/m), causing the malaria-infected, parasitized RBCs (pRBCs) to migrate or "marginate," where upon they are skimmed off by a side branch (bleed-slit, in Figure 2.1 bottom). The purified blood is then returned to the patient from a return outlet, (C in Figure 2.1 bottom). This design allows continuous filtration, analogous to renal dialysis. The engineering challenge is to optimize the efficiency of this magnetic separator to maintain the overall size of the system within the desired envelope. [63]

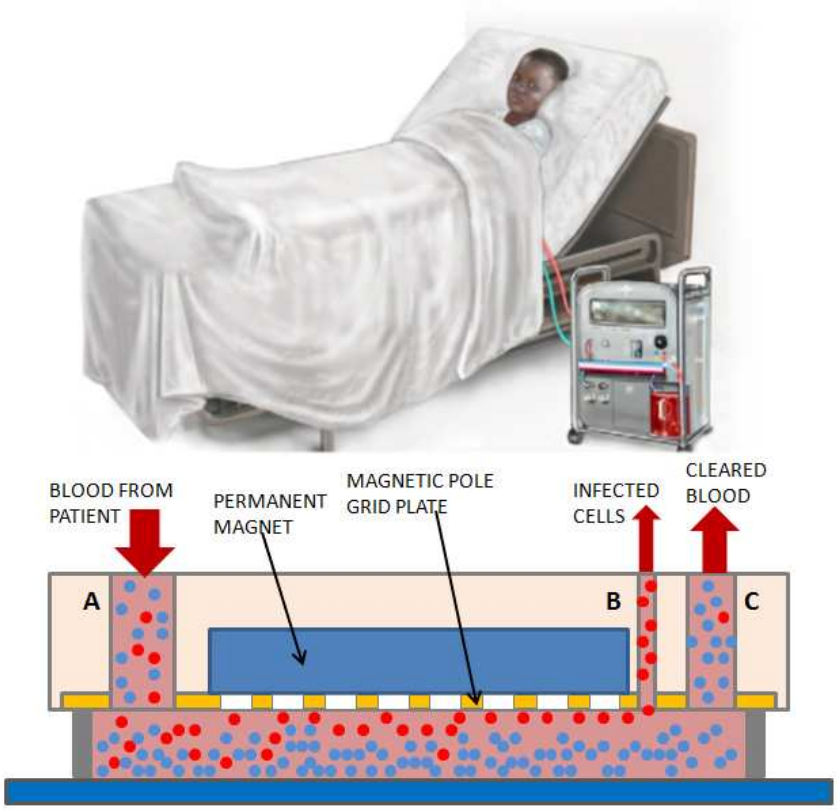

Figure 2.1 The envisioned mPharesis^{TM} system (top) in clinical setting, and (bottom) principle of operation of mPharesisTM filter. (A) Blood inlet, (B) Bleed-slit, (C) Return outlet. [63]

This present study focused on the influence of the geometry of an individual separation channel on the efficiency of magnetic separation. Specifically, it explored the hypothesis that the introduction of a constriction at the entrance of the channel would improve the efficiency compared to a standard parallel-plate channel. The assumption was that since the magnetic force diminishes very rapidly with distance from the magnet poles, it would be advantageous to initially divert the magnetic cells in close proximity to the greatest gradient where they would be retained by the magnetic force. Downstream of the constriction, the non-magnetic healthy cells would diffuse across the height of the channel, while the magnetic cells would remain close to the wall.

For simulating the separation of the pRBCs and RBCs, in the model applied to study the current problem the pRBCs and RBCs should be distinguishable to each other, therefore a solid-fluid multiphase (or multi-component) system has to be applied to model the blood flow system in current work. According to the scale of the problems modeled, the solid-fluid multiphase models may be classified into three distinct types [64]. At the largest scale, such as engineering scale fluidization and pneumatic conveying, the Eulerian (two-fluid) approach is usually applied, in which the solid particles are usually modeled as a complex fluid and two phases are coupled through momentum exchange (interaction) terms, see [65, 66]. When the order of the number of the particles in the system is about or less than $O(10^6)$, we have the discrete element method (DEM). The discrete element method (DEM) is widely used for the understanding of particulate behavior in many industrial applications such as mining, metals manufacturing, and pharmaceutical manufacturing. Applying the CFD-DEM method, Fenech et al. [67] studied the RBC aggregation in shear flow, and Chesnutt and Marshall [68] showed effect of the RBCs collision and aggregation on the large variation in hematocrit throughout the circulatory system by studying the blood flow through a bifurcation. For investigating microscopic behavior of particles, such as deformation, cluster formation and tumbling of RBCs, the Immersed Boundary Method (IBM) combined with the Lattice Boltzman Method (LBM) has become a popular method [56, 57, 69].

In current problem, considering the requirement of distinguishing the pRBCs and RBCs, for applying three-fluid model the constitutive equation of the interaction force between pRBCs and RBCs, which is absence so far, has to be known; For LBM-IBM method, considering that the order of the number of the particles in the system is about $O(10^5)$, the computational cost of applying LBM-IBM method is prohibitively expensive and wasteful. Therefore, in current

chapter, the CFD-DEM method will be applied. In section 2, the governing equation of the CFD-DEM method will be discussed; in section 3, the mPharesis™ (magnetic aphaeresis) system will be introduced in detail; in section 4, the effect of the channel geometries on the pRBCs separation will be studied.

2.2 Governing equations

We use an Eulerian-Lagriangian framework where the continuous phase, i.e., the plasma is modeled as a fluid (the Eulerian approach) and the dispersed phase, i.e., the red blood cells (RBCs) are modeled as particles. The interaction forces between these two components, the external magnetic force, and the contact force, need to be modeled.

Continuous phase (Plasma)

In the absence of thermo-chemical effects, the governing equations consist of the conservation of mass, linear momentum and angular momentum. The equation for the conservation of mass in the Eulerian form reads,

$$\frac{\partial \rho_p}{\partial t} + div\left(\rho_p \boldsymbol{v}_p\right) = 0 \tag{2.1}$$

where subscript p refers to the plasma phase, $\frac{\partial}{\partial t}$ is the derivative with respect to time, *div* is the divergence operator, $\rho_p = \varepsilon \rho_{p0}$, ρ_{p0} is the pure density of the plasma in the reference configuration, ε is the porosity and $\phi = (1 - \varepsilon)$ is the volume fraction (hematocrit) of the RBCs and $\boldsymbol{v}$ is the velocity field. Usually when one CFD mesh contains $O(10^2)$ particles, the porosity can be directly calculated as proposed by Hoomans et al. [70]. However when the size of the particle is in the same order of the CFD mesh, the method by Hoomans may cause numerical

instability. Instead Link et al[71] have proposed a new method, which is applied in our work, for overcoming this difficulty. The balance of the linear momentum can be written as,

$$\rho_p \frac{D^p \boldsymbol{v}_p}{Dt} = div(\boldsymbol{T}_p) + \rho_p \boldsymbol{b}_p + \boldsymbol{F}_{pr} \tag{2.2}$$

where $\frac{D^p \boldsymbol{v}_p}{Dt} = \frac{\partial \boldsymbol{v}_p}{\partial t} + (\nabla \boldsymbol{v}_p)\boldsymbol{v}_p$, $\boldsymbol{T}_p$ stands for the Cauchy stress tensors, $\boldsymbol{F}_{pr}$ represents the interaction forces (exchange of momentum) between the plasma and RBCs, and $\boldsymbol{b}_p$ refers to the body force. The balance of the angular momentum implies that, in the absence of couple stresses, the Cauchy stress tensor is symmetric.

RBCs

The equation of motion for the RBCs is represented by,

$$m_r \frac{D^2 \boldsymbol{x}_r}{Dt} = \boldsymbol{F}_{contact} + \boldsymbol{F}_{pr} + \boldsymbol{F}_{ext} \tag{2.3}$$

where m_r is the mass of RBCs, $\boldsymbol{x}_r$ is the spatial position of RBCs, $\boldsymbol{F}_{contact}$ is the force due to collision with other RBCs or walls, etc., $\boldsymbol{F}_{pr}$ is the interaction force from the continuous phase, i.e., the plasma, and $\boldsymbol{F}_{ext}$ is the force due to external sources, such as gravity, magnetic force, etc. In our study, for $\boldsymbol{F}_{contact}$, we only consider the particle-particle and particle-wall collisions; for $\boldsymbol{F}_{pr}$, only the drag force is included and the drag model by Rusche and Issa [72] is applied; $\boldsymbol{F}_{ext}$ implies that the pRBCs are influenced by the applied magnetic force (an expression for this will be discussed in a later section).

2.3 Constitutive equations

Plasma

In this chapter, we assume that the plasma behaves as a linear viscous fluid

$$\boldsymbol{T}_p = \left[-p(1-\phi) + \lambda_p(1-\phi)tr\boldsymbol{D}_p\right]\boldsymbol{I} + 2\mu_p(1-\phi)\boldsymbol{D}_p \tag{2.4}$$

where p is the pressure of the mixture, λ_p and μ_p are the (constant) first and second coefficients of viscosity of the pure plasma, where $\boldsymbol{D}_p = \frac{1}{2}\left[\left(grad\ \boldsymbol{v}_p\right) + \left(grad\ \boldsymbol{v}_p\right)^T\right]$, '*tr*' stands for the trace of a second order tensor, and $\boldsymbol{I}$ is the identity tensor.

RBCs collision: Soft-sphere model

In general, particle collisions can be handled by two different method : a hard-sphere model [70] and a soft-sphere model [73]. In a hard-sphere system the forces between the particles are not explicitly considered and the trajectories of particles are determined by momentum conserving binary collisions; therefore numerically the hard-sphere models are faster than the soft-sphere models [64]. However, for a more dense system, the hard-sphere model may lead to a drastic kinetic energy, which is called the inelastic collapse [74, 75], and as a result the soft-sphere method is widely used for such a system. The soft-sphere model incorporates multiple particle-particle interactions and the trajectories are determined by integrating Newton's second law. For simulating the blood flow, considering the bulk volume fraction of the RBCs (hematocrit) is about 0.4-0.45, the soft-sphere method is applied in our study.

According to Cundall and Strack [73], the normal component of the contact force, $\boldsymbol{F}_{contact}^{ij,n}$, acting on particle i by particle j (or wall) is,

$$\boldsymbol{F}_{contact}^{ij,n} = -k_n\delta_n\boldsymbol{n}_{ij} - \eta_n\boldsymbol{v}_{r,ij,n} \tag{2.5}$$

where k_n and η_n are the normal spring stiffness and damping coefficients respectively, $\delta_n = \left(R_i + R_j\right) - \left|\boldsymbol{r}_i - \boldsymbol{r}_j\right|$ is the overlap between two RBCs, R is the radius of a RBC, $\boldsymbol{n}_{ij} = \left(\boldsymbol{r}_i - \boldsymbol{r}_j\right)/\left|\boldsymbol{r}_i - \boldsymbol{r}_j\right|$ is the normal unnit vector between two RBCs, $\boldsymbol{v}_{r,ij,n} = \left(\boldsymbol{v}_{r,ij}.\boldsymbol{n}_{ij}\right)\boldsymbol{n}_{ij}$ is the

normal relative velocity, $\boldsymbol{v}_{r,ij} = (\boldsymbol{v}_i - \boldsymbol{v}_j) + (R_i\boldsymbol{\omega}_i + R_j\boldsymbol{\omega}_j) \times \boldsymbol{n}_{ij}$ is the relative velocity, and $\boldsymbol{\omega}$ is the angular velocity. The tangential component of the contact force between the particles is

$$\boldsymbol{F}_{contact}^{ij,t} = \begin{cases} -k_t\delta_t - \eta_t\boldsymbol{v}_{r,ij,t} \text{ for } |\boldsymbol{F}_{contact}^{ij,t}| \le \mu_f|\boldsymbol{F}_{contact}^{ij,n}| \\ -\mu_f|\boldsymbol{F}_{contact}^{ij,n}|\boldsymbol{t}_{ij} \text{ for } |\boldsymbol{F}_{contact}^{ij,t}| > \mu_f|\boldsymbol{F}_{contact}^{ij,n}| \end{cases} \tag{2.6}$$

where k_t, η_t, and μ_f are the tangential spring stiffness, tangential damping coefficient, and friction coefficients, respectively, $\boldsymbol{v}_{r,ij,t} = \boldsymbol{v}_{r,ij} - \boldsymbol{v}_{r,ij,n}$ is the relative tangential velocity, $\boldsymbol{t}_{ij} = \boldsymbol{v}_{r,ij,t}/|\boldsymbol{v}_{r,ij,t}|$ is the tangential unit vector, and δ_t is the tangential displacement and is given by (detail see [64, 76])

$$\delta_t = \begin{cases} \delta_{t0}\boldsymbol{H} + \int_{to}^{t} \boldsymbol{v}_{r,ij,t}dt \text{ for } |\boldsymbol{F}_{contact}^{ij,t}| \le \mu_f|\boldsymbol{F}_{contact}^{ij,n}| \\ -\mu_f|\boldsymbol{F}_{contact}^{ij,n}|\boldsymbol{t}_{ij}/k_t \text{ for } |\boldsymbol{F}_{contact}^{ij,t}| > \mu_f|\boldsymbol{F}_{contact}^{ij,n}| \end{cases} \tag{2.7}$$

$$\boldsymbol{H} = \begin{bmatrix} qh_x^2 + c & qh_xh_y - sh_z & qh_xh_z + sh_y \\ qh_xh_y + sh_z & qh_y^2 + c & qh_yh_z - sh_x \\ qh_xh_z - sh_y & qh_yh_z + sh_x & qh_z^2 + c \end{bmatrix} \tag{2.8}$$

where $\boldsymbol{h} = (\boldsymbol{n}_{ij} \times \boldsymbol{n}_{ij0})/|\boldsymbol{n}_{ij} \times \boldsymbol{n}_{ij0}|$, $c = \cos\varphi$, $s = \sin\varphi$, $q = 1 - c$, $\varphi = \arcsin|\boldsymbol{n}_{ij} \times \boldsymbol{n}_{ij0}|$, δ_{t0} and $\boldsymbol{n}_{ij0}$ are the tangential displacement and normal direction in the previous time step, respectively and μ_f is the frictional coefficient. The mechanism of the particle-wall collision is the same as the particle-particle collision (for detail derivations see [64]). The determination of the stiffness and damping coefficients can be found in [64, 77].

2.4 Magnetic Field and Geometry

According to Han and Frazier [78] and Kim et al. [79], the expression for the magnetic force produced by a ferromagnetic cylindrical wire placed under a uniform external magnetic field, referenced to a coordinate system centered at the wire (x', y') is:

$$\boldsymbol{F}_{magnetic}(x', y')$$

$$= 2k\mu_0(\chi_{rbc} - \chi_p)V_{rbc}a^2H_0^2\frac{(ka^2 + 3(a + y')^2 - x'^2)x'}{(x'^2 + (a + y')^2)^3}\boldsymbol{e}_{x'} \quad (2.9)$$

$$+ 2k\mu_0(\chi_{rbc} - \chi_p)V_{rbc}a^2H_0^2\frac{(ka^2 - 3x'^2 + (a + y')^2)(a + y')}{(x'^2 + (a + y')^2)^3}\boldsymbol{e}_{y'}$$

where $\mathbf{e_x}$' and $\mathbf{e_y}$' are the unit vectors in the x' and y' directions, respectively; $k = \frac{\mu_w - \mu_0}{\mu_w + \mu_0}$=1 here, μ_w and μ_0 are the magnetic permeability of the ferromagnetic wire and free space ,respectively; χ_p and χ_{rbc} are the magnetic susceptibilities of the plasma and the pRBC; V_{rbc} is the volume of the pRBC; and a is the radius of the wire. According to Kim et al. [79], Han and Frazier [78] and Hackett et al. [80], the magnitude of $\boldsymbol{F}_{magnetic}\boldsymbol{e}_x$ is much less than $\boldsymbol{F}_{magnetic}\boldsymbol{e}_y$, and it therefore neglected in this simulation. For conservation of computational cost, we further assume that $\boldsymbol{F}_{magnetic}\boldsymbol{e}_y$ is uniform along the x direction which simplifies the expression as:

$$\boldsymbol{F}_{magnetic}(y') = 2\mu_0(\chi_{rbc} - \chi_p)V_{rbc}a^2H_0^2\frac{(a^2 + (a + y')^2)(a + y')}{((a + y')^2)^3}\boldsymbol{e}_{y'}$$

$$= CV_{rbc}\frac{(a^2 + (a + y')^2)(a + y')}{(a + y')^6}\boldsymbol{e}_{y'} \quad (2.10)$$

where $C = 6.6701e^{-9}\ kg.m/s^2$ and $a = 50e^{-6}\ m$. (See Figure 2.2(a).)

Because the magnitude of the magnetic force decays very quickly, the pRBCs at the farthest (bottom) wall experience significantly less force than those on the top wall (appx 3%). Yet these cells have the farthest to travel to completely stratify the blood. For this reason, we introduce an upstream constriction, shown in Figure 2.2(b) to initially bring all cells in close proximity to the greatest magnetic force. Thereafter, the channel expands to its full height, which permit the RBCs to transport away from the magnetic wall, leaving the pRBCs trapped in a

boundary layer. An added diffuser is introduced to streamline this process. (See Figure 2.2(c).) Without loss of generality, the length of the channels are all specified as 10mm.

The above governing equations were implemented in OpenFOAM, and solved on a PC workstation (Dell T3500.) The initial condition for the simulation is a cell-free domain. At t=0, the cells are injected from the inlet in the ratio of pRBCs:RBCs = 1:9. Additional physical parameters and flow conditions are provided in Table 2.1. Zero pressure is applied at the outlet.

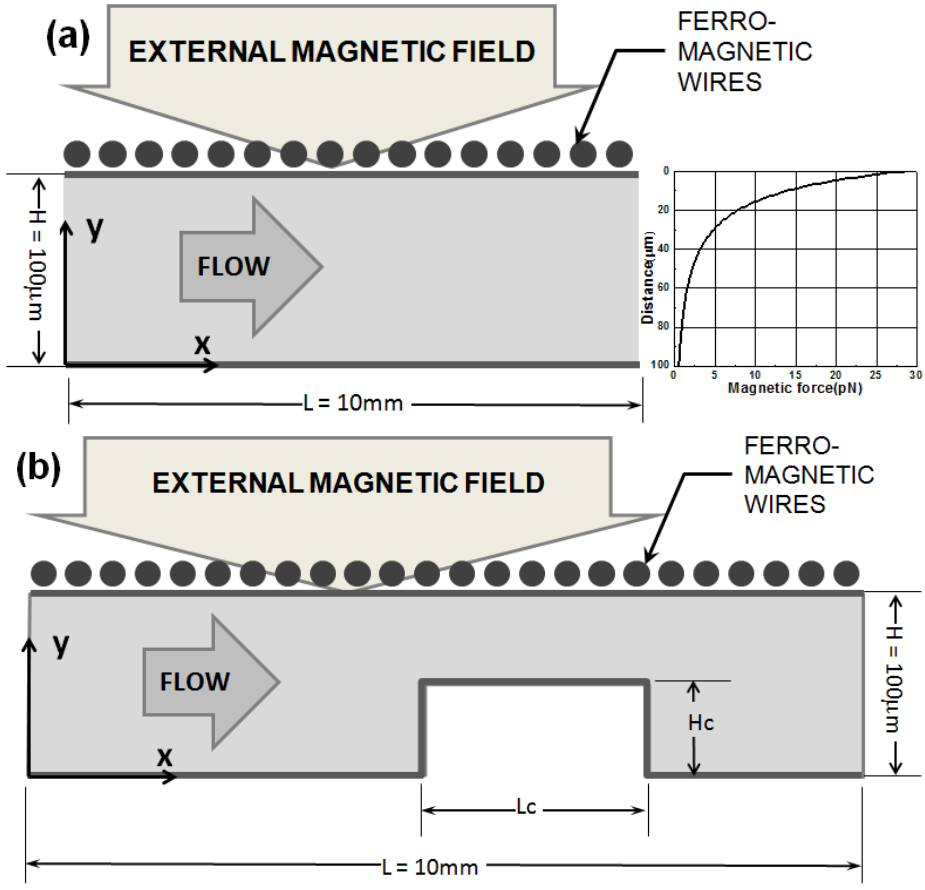

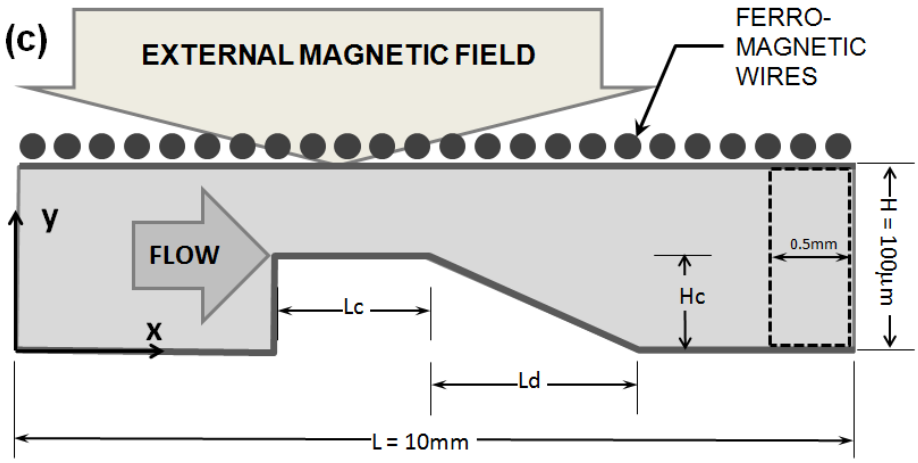

Figure 2.2 (a) Channel without constriction; (b). Channel with constriction. (c). Channel with constriction and diffuser. For all the cases the length of the channels are 10 mm (along x direction), the height of the channel where there is no constriction is $100\mu m$ (along y direction) and the simulation is two dimensional therefore there is no dimension on z direction.

Plasma viscosity	0.96cP
Plasma density	1027 kg/m^3
Diameter of RBCs	8 μm
Young's modules of RBCs	26kPa[81]
Poisson's ratio of RBCs	0.5[81]
Friction coefficient between RBCs and between RBC and wall	0.08 [76]
Hematocrit (Average volume fraction of RBCs)	40%
Bulk inlet velocity (Whole blood)	0.01 m/s

Table 2.1 Physical properties and flow condition. (To economize computational cost the diameter of the RBCs are specified as $8\mu m$.)

2.5 Results

All simulations were run for more than 3s to assure steady state conditions were reached. To account for the discretization of the pRBC and RBC phases, all data shown in the following

sections are averaged from 100 different time steps. Prior to simulations of the various geometries of the channels, a mesh dependency study was first performed using the 10mm-length rectangular channel (Figure 2.2(a)))), and the results are shown in Figure 2.3. It was found that meshes of 18288 and 31248 nodes both closely approximated the theoretical (Newtonian) prediction, therefore a mesh with 18288 nodes was chosen. Mesh dependency studies were confirmed for the other geometries as well.

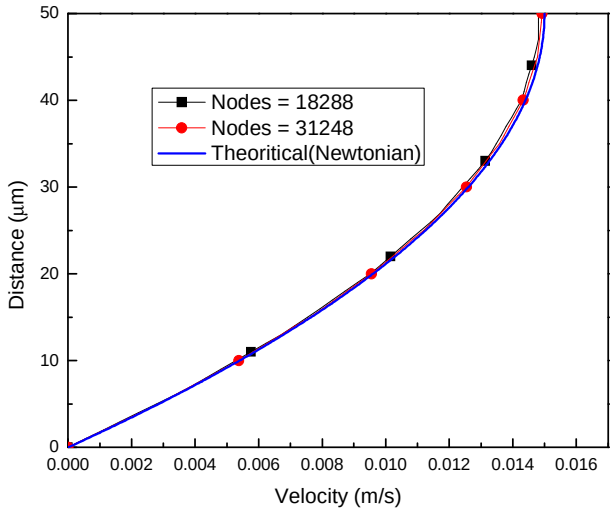

Figure 2.3 Mesh dependency study and model validation.

For quantifying the separation efficiency, the pRBCs density distribution across the channel was evaluated at the outlet. To accommodate the discrete size of the cells, the outlet was discretized into 20 regions, each 5 microns in height. Although the bleed slit was not included in the simulation, the presumption was that the flow exiting the outlet would be split such that the concentrated pRBC layer of blood would be collected, and the remaining blood returned to the patient. (The specific split ratio would be chosen based on clinical considerations, such as availability of blood, risk of anemia, etc.)

Effect of Inlet Constriction H_c

The pRBC distributions are provided in Figure 2.4 for rectangular constriction of 50% and 80%, 2mm in length, and are compared with the baseline (no constriction). Table 2.2 shows the percentage of the pRBCs in the near-wall subzone (20 microns). We defined enrichment efficiency to compare the concentration in this region to the bulk *concentration* of pRBCs,

$$\text{enrichment efficiency} = \frac{\text{pRBC concentration near wall}}{\text{bulk pRBC concentration}} - 1 \tag{2.11}$$

As contrasted to the channel without constriction, which provided very limited enrichment (28%) the channels were markedly more efficient (91.5% and 139% for the 50 micron and 20 micron constriction respectively.)

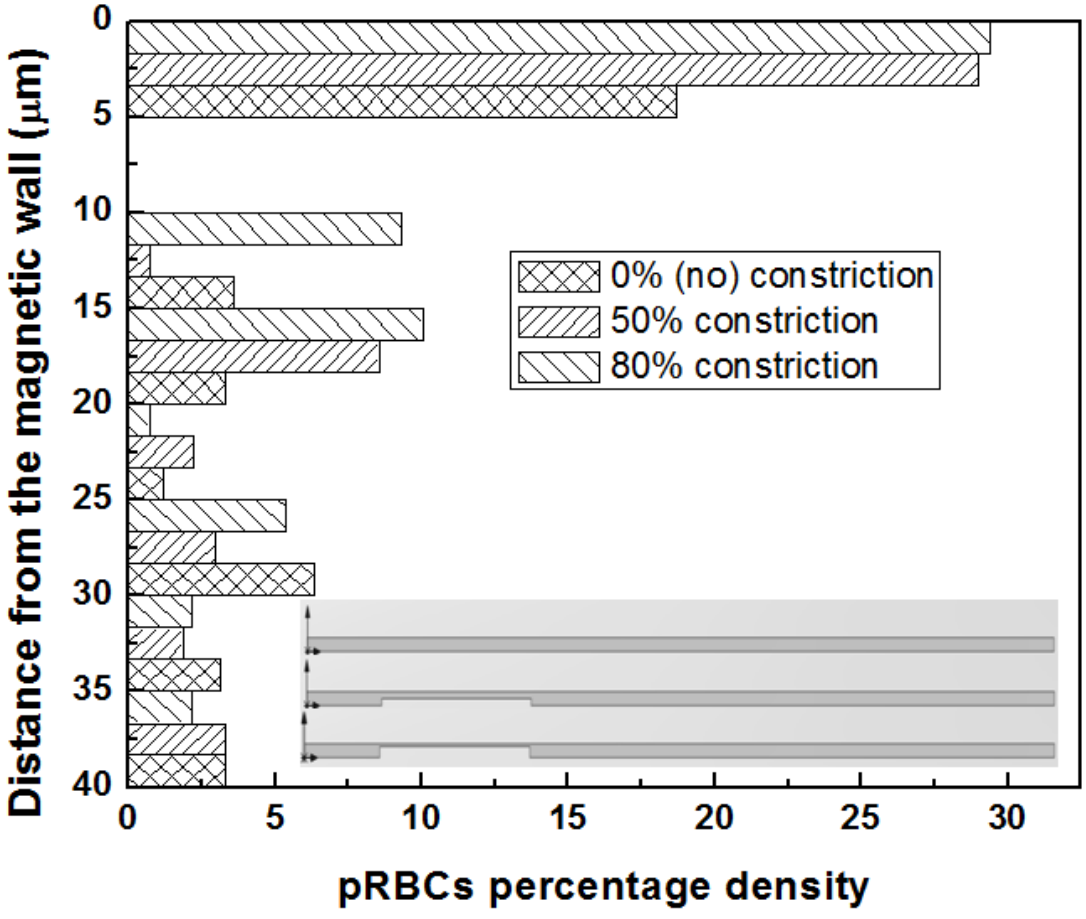

Figure 2.4 Percentage density distribution at the outlet along the y direction, effect of H_c. Percentage density = number of pRBCs in a subzone/total number of pRBCs in all subzones.

Constriction(H_c)	pRBC percentage density	Enrichment
(No constriction)	25.6%	28.0%
50% ($50\mu m$)	38.3%	91.5%
80% ($80\mu m$)	47.8%	139.0%

Table 2.2 Effect of constriction height.

Effect of Constriction Lengths L_c

To evaluate the relative benefit of lengthening the constriction L_c, six (6) different lengths were evaluated (0.2, 0.5, 1.0, 2.0, 4.0 and 8.0 mm) each having a height of 20 micron. These results are provided in Figure 2.5 and Table 2.3. It can be seen that there is a slight improvement with length from 0.2mm up to 4mm, beyond which further extension to 8mm yields diminishing returns.

Length of the constriction(L_c)	Percentage density	Enrichment
8mm	55.3%	176.7%
4mm	55.9%	179.45%
2mm	47.8%	139.05%
1mm	48.8%	143.85%
0.5mm	45.6%	128.05%
0.2mm	40.7%	103.25%

Table 2.3 Effect of constriction length.

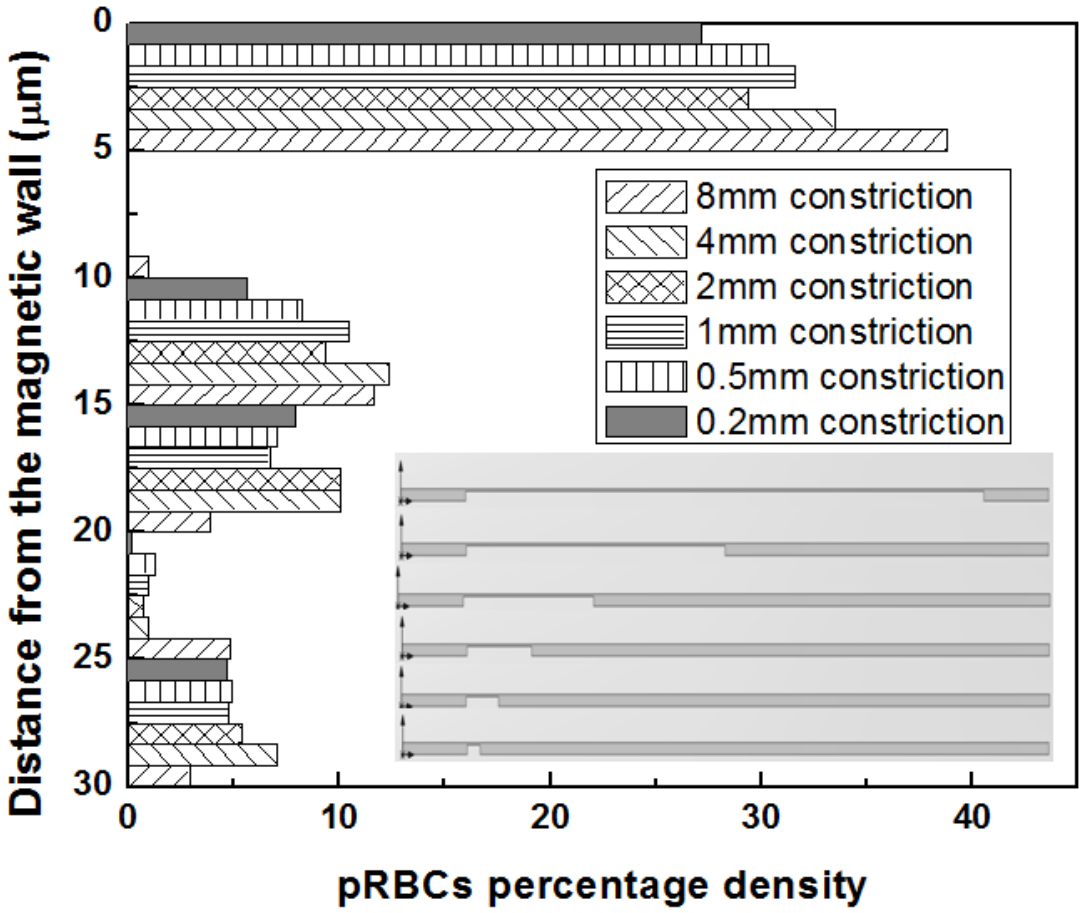

Figure 2.5 Percentage density distribution at the outlet along the y direction, effect of L_c.

Effect of the diffuser after the constriction L_d

Following the constriction, it is desired for the RBCs to gradually advect from the wall, leaving the pRBCs trapped in the magnetic boundary layer. However a sudden expansion may cause a flow disturbance that may draw pRBCs away from the wall. Therefore a tapered diffuser was introduced for the case of $80\mu m$ x 2mm constriction. (See Figure 2.2.). The corresponding results are provided in Figure 2.6 and Table 2.4 which reveals a dramatic improvement (by 121%, from 139% to 260%) by introducing a diffuser of just 1mm. The incremental improvement by extending the diffuser to 2mm was negligible.

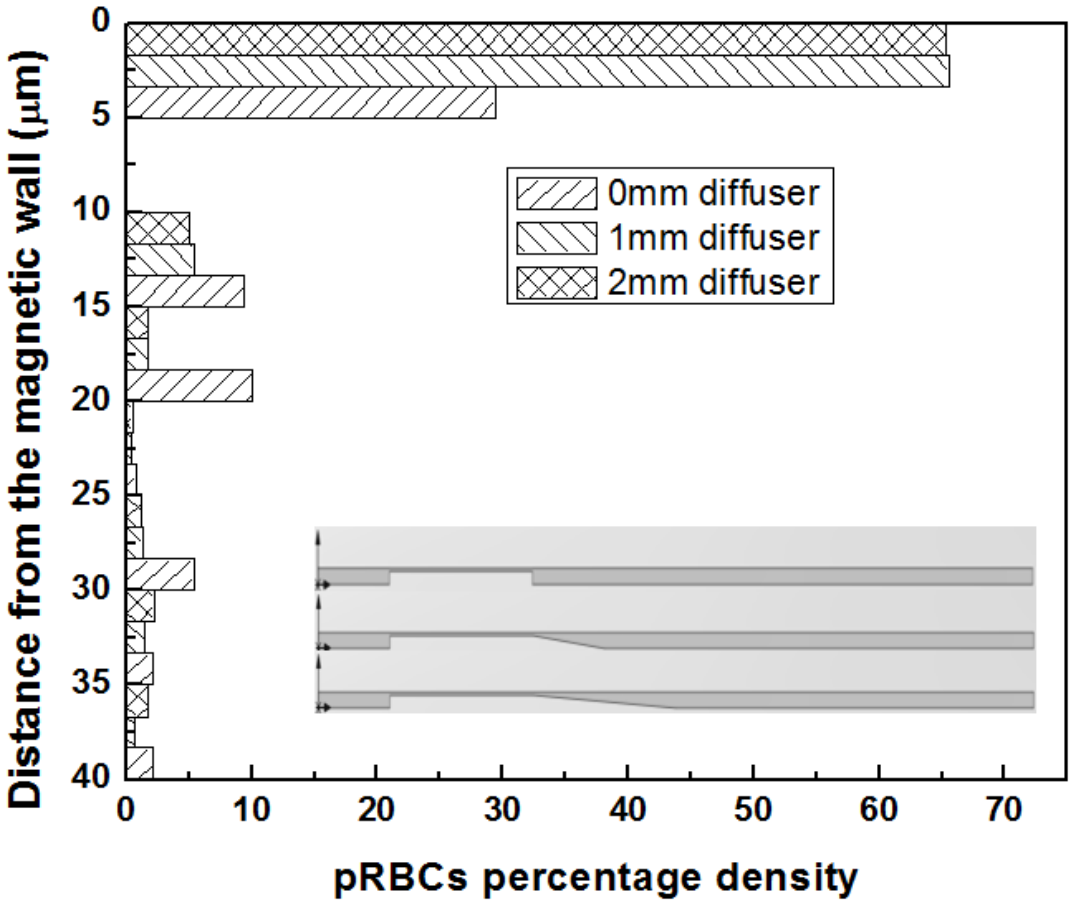

Figure 2.6 Percentage density distribution t the outlet along the y direction, effect of L_d.

Length of the diffuser(L_d)	Percentage density	Enrichment
none (sudden expansion)	47.8%	139.05%
1mm	72.7%	263.4%
2mm	72.1%	260.6%

Table 2.4 Effect of diffuser.

2.6 Discussion

The World Health Organization (WHO) estimates that each year approximately 300 million malaria episodes occur globally resulting in nearly one million deaths, 85% of which are children

under five years of age [82]. Extracorporeal systems currently used to accelerate the *i-RBC* clearance *(e.g., COBE Spectra® Apheresis System, CaridianBCT)* are not engineered to selectively separate *i-RBCs* from healthy RBCs: to remove the infected *RBCs*, 70%-95% of the healthy blood is wasted. This is precisely the motivation for the proposed *mPharesis*™ system: that will allow the removal of toxic *i-RBCs* from circulation with minimal or no requirement of healthy blood.

In this chapter, the CFD-DEM method is applied. For simulating the separation of the pRBCs and RBCs, the pRBCs and RBCs should be distinguished from each other, which implies a solid-fluid multiphase (or multi-component) system has to be applied to model the blood flow system. Therefore, several possible models for current problem can be three-fluid model, CFD-DEM model, and meso-scale simulation such as LBM-IBM (Immersed Boundary Method combined with the Lattice Boltzmann Method). For applying three-fluid model, the constitutive equation of the interaction force between pRBCs and RBCs, which has not been studied so far, has to be known. For LBM-IBM method, considering that the number of the particles in the system is about $O(10^5)$, the computational cost of applying LBM-IBM method is prohibitively expensive and wasteful. Yin et. al[83] studied cell separation using magnetic field with LBM-IBM but the order of the number of the cells simulated is only $O(10^1)$.

Different with the general CFD-DEM, in current work, volume fraction of RBCs, ϕ, is computed using the method introduced by Link et al. [71] for increasing the numerical stability. Because usually when one CFD mesh contains $O(10^2)$ particles, the volume fraction of the fluid can be directly calculated as proposed by Hoomans et al. [70], however when the size of the particle is in the same order of the CFD mesh the method by Hoomans may cause numerical instability.

The current study shows that as the length of the constrictions, L_c, increases, more of the pRBCs concentrate near the magnetic wall, since longer constrictions provides more time for the pRBCs to experience a greater magnetic force field, but it also should be noticed that the improvement is not so dramatic. From the Table 2.3, we also can find that there is no big difference between the 4mm and the 8mm constrictions, which may imply that there is an upper limit to the length which can provide the pRBCs enough time to move toward to and finally contact the magnetic wall.

In addition to the collisions between RBCs, hydrodynamic force (drag force) plays main role preventing pRBCs from concentrating near the magnetic wall after the constriction, which means reducing the hydrodynamic force at the outlet of the constriction may highly improve the separation. Figure 2.4 shows the channel with $H_c = 80\mu m, L_c = 2mm$ constriction has the similar performance to the one with $H_c = 50\mu m, L_c = 2mm$ in the region where y ranges from 90 to $100\mu m$. This is considered to be due to the competition between the hydrodynamic force and magnetic force. Smaller constriction makes pRBCs have larger possibility to experience larger magnetic force which pulls the pRBCs penetrate the streamline, however at the outlet of the constriction the pRBCs also experience a larger drag force, which makes the pRBCs move along the streamline. Therefore, addition of a diffuser at the outlet of $H_c = 80\mu m, L_c = 2mm$ constriction dramatically increases the near wall pRBCs enrichment efficiency from 139% to 260%, also see Figure 2.8(d) and (e) for visual comparison. It can be seen that with such a high pRBCs concentration, shown in Figure 2.8(e), in the neighborhood of the magnetic wall, this is a promising sign for removing the pRBCs without losing or consuming the healthy RBCs.

In current work, we chosen $C = 6.6701e^{-9}\ kg.m/s^2$ and $a = 50e^{-6}\ m$. The practical value of C and a depends on various parameters and conditions which will lead to a magnetic force

smaller or larger than the one applied in current work. According to [78, 84], the y-direction velocity of pRBCs are linearly proportional to the magnetic force (already consider the effect of the drag force), and obviously the x-direction velocity of pRBCs are linearly proportional to the inlet velocity, which implies that increasing the magnetic force and inlet velocity for same times will give the same separation results, also see numerical verification shown in Figure 2.7. Therefore, for experimental design or test consideration, if the practical magnetic force is different with the one applied here, same separation efficiency can be achieved by adjusting the inlet velocity.

Considering we focus on studying the effect of the channel geometry on the separation efficiency, therefore for saving computational cost we assume $\boldsymbol{F}_{magnetic}\boldsymbol{e}_y$ keep constant along x, namely expressed as equation (2.10). Because in practical $\boldsymbol{F}_{magnetic}\boldsymbol{e}_y$ varies along x direction and the magnitude is equal or smaller than the force described by equation (2.10). For achieving same pRBC separation, with same conditions, applying equation (2.9) requires much longer separation channel than equation (2.10) which implies a much larger computational cost.

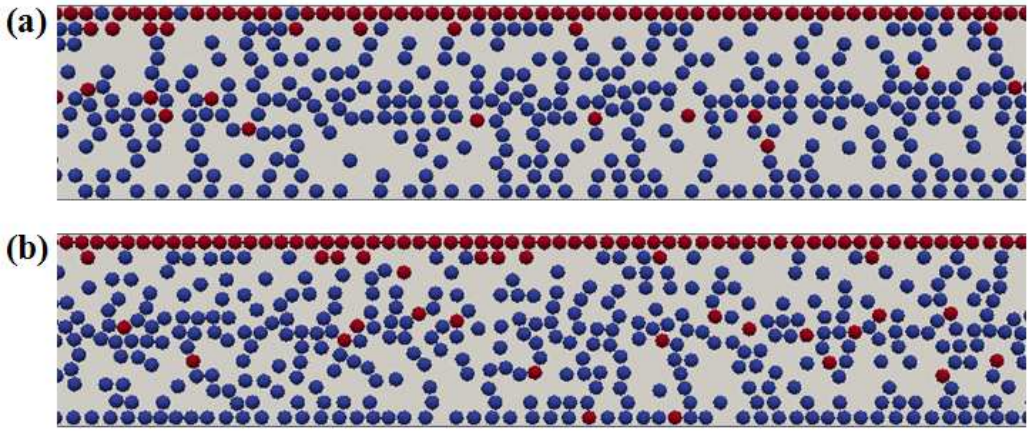

Figure 2.7 Snapshot of RBCs distribution in the channel region near the outlet(see dash-line box in Figure 2.2(b)) using channel with $H_c = 80\mu m, L_c = 2mm$ constriction and $L_d = 2mm$ diffuser. Red: Infected RBCs; Blue:

Normal RBCs. (a) Inlet velocity is 0.01m/s, $C = -3.375e^{-9}\ kg.m/s^2$, see equation (2.10); (b) Inlet velocity is 0.001m/s, $C = -3.375e^{-10}\ kg.m/s^2$.

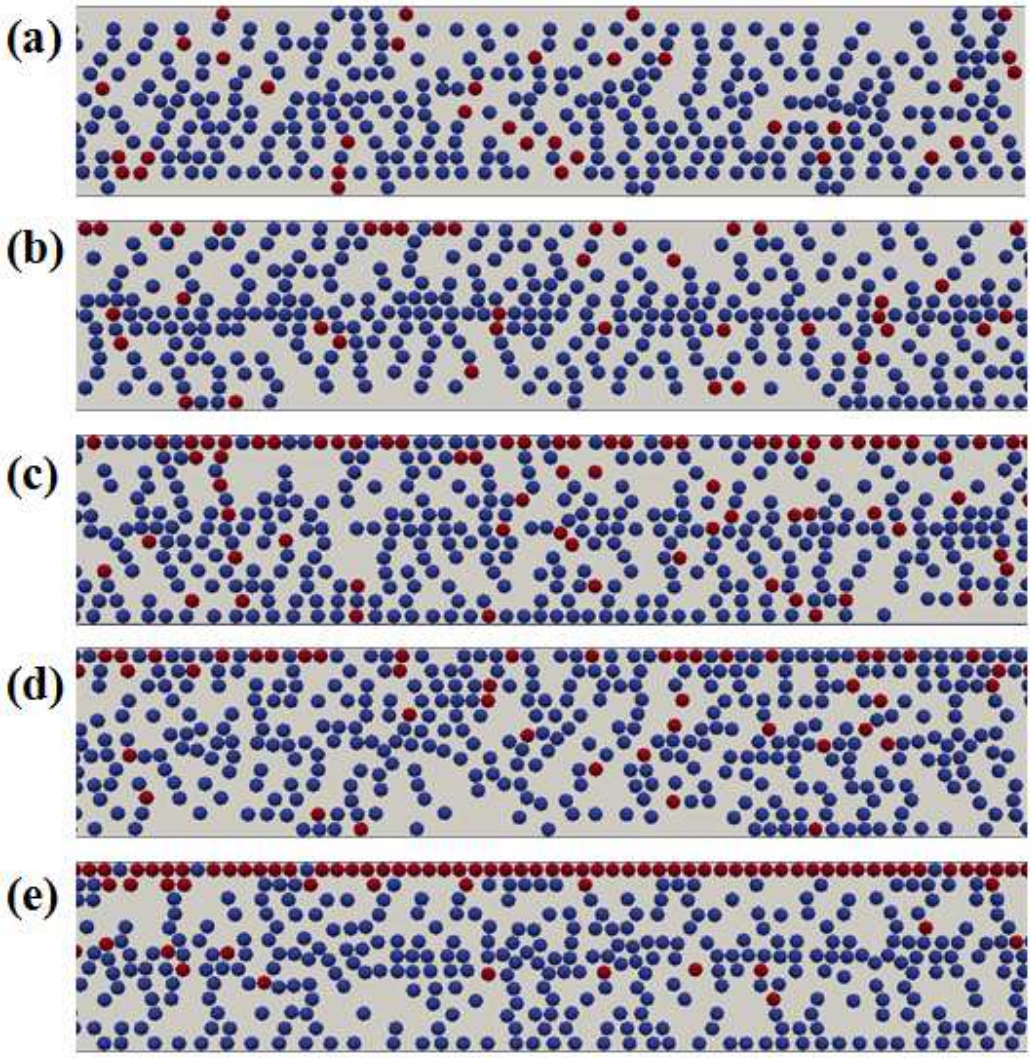

Figure 2.8 Snapshot of RBCs distribution in the channel region near the outlet, namely from x=9.5mm to x=10mm(outlet), see dash-line box in Figure 2.2(b). Red: Infected RBCs; Blue: Normal RBCs. (a) Channel without constriction and diffuser; (b) Channel with $H_c = 50\mu m, L_c = 2mm$ constriction and no diffuser; (c) Channel with $H_c = 50\mu m, L_c = 2mm$ constriction and $L_d = 2mm$ diffuser; (d) Channel with $H_c = 80\mu m, L_c = 2mm$ constriction and no diffuser; (e) Channel with $H_c = 80\mu m, L_c = 2mm$ constriction and $L_d = 2mm$ diffuser.

2.7 Summary

In this chapter, a malaria infected RBCs (pRBCs) separation system is studied and channels with constriction/constrictions and a diffuser after constriction are suggested as promising designs for such a separation system. The CFD-DEM approach (Eulerian-Lagrangian) is applied to model the blood flow. The plasma is treated as a Newtonian fluid (as the Eulerian phase), and the RBCs are treated as soft spheres (as the Lagrangian phase); furthermore the pRBCs are influenced by the magnetic field while the healthy RBCs are not.

Through the numerical studies, we find that channels without any features, namely the rectangular channel, only has a little improvement on the pRBCs separation [see Table 2.2], while channels with constriction/constrictions and a diffuser can significantly increase the separation efficiency (also see Figure 2.8 for comparison on separation efficiency among different channel designs). From Figure 2.8(e), we can find that when using a channel with $20\mu m$ height constriction and 2mm length diffuser, almost all the pRBCs are concentrated in the neighborhood of the magnetic wall and can be easily removed by adding a side branch channel. We also proved that increasing or decreasing the flow rate and the magnetic force by same times gives almost exact same separation efficiency, which implies our results gives general information for other various different cases, such as different particles with different magnetic field.

Therefore it should be emphasized that the channel with a diffuser after a constriction is a promising design for practical application. Furthermore, through these simulation studies we also find that channels with longer constriction show a moderately better separation efficiency, while channels with multi-constrictions have similar performance to the single constriction. Therefore

a channel with long constriction or multi-constrictions should be chosen carefully considering the higher pressure drop that it requires for smooth operations.

Chapter 3 A three dimensional thrombus growth model

3.1 Introduction

Thrombus formation in the coronary artery can lead to heart attacks [13-15], and thrombus can be transported to the brain by blood circulation causing cardiogenic strokes [16]. Heart attacks and strokes have been the leading cause of death in developed countries [15, 17, 18]. Furthermore, the thrombus generation in blood related medical devices can heavily reduce the efficiency and lead to device malfunction. Thrombus generation is a complex phenomenon, related to various hemodynamics and biomechanical processes, which generally can be classified into two main sub-processes: platelet activation, aggregation and coagulation [40]. In the early stages of thrombus formation, the platelets play a major role, where thrombus formation is initiated with the activation of the platelets exposed to unfavorable high shear rates or high concentration of chemical agonists; the activated platelets will aggregate and release agonists activating more unactivated platelets [41, 85-87].

3.2 Thrombus formation

Bizzozero in 1882 first recognized that during the procedure of thrombus formation the platelets are the predominant antagonists [15, 88]. Recent studies have revealed most of the complex biological reactions during thrombus formation [15, 89-91], which leads to the possibility of accurately describing the thrombus formation by developing mathematical models [87, 92]. Figures 1-3 show the major biological reactions of thrombus formation. Figure 3.1(a) shows the backbone of the thrombus system involving several cascade reactions, and Figure 3.1(b) and Figure 3.1(c) show the feed-forward and feedback loops promoting and inhibiting coagulation

reactions respectively. For a detailed discussion of the reactions and interactions see [91]. Positive and negative feedback loops, which involve numerous chemical species and reactions, compete with each other and also coupled with flow fields, are the most essential processes which need to be considered to accurately describe thrombus formation. Therefore, it can be seen that a comprehensive description of thrombus generation requires a model which can describe complex cascade reactions, such as platelets activation, platelet-platelet aggregation, platelet-surface(wall) adhesion, transportation of the platelets and chemical species in flow, and the interaction between the formed thrombus and the flow field [1, 2]. The large number of chemical species and the complexity of cascade reactions make it very difficult to synthesize a coherent picture of coagulation dynamics using traditional laboratory approaches [91].

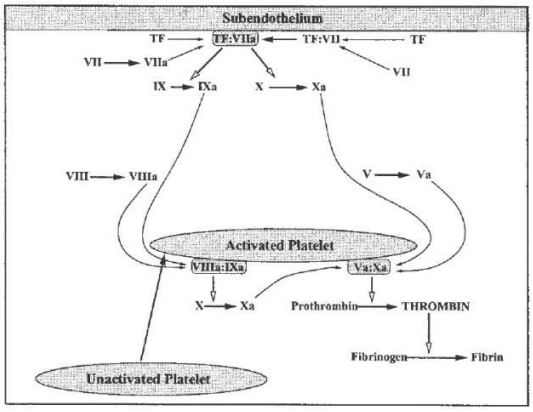

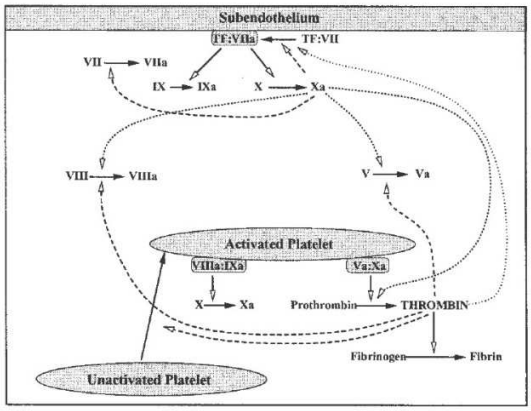

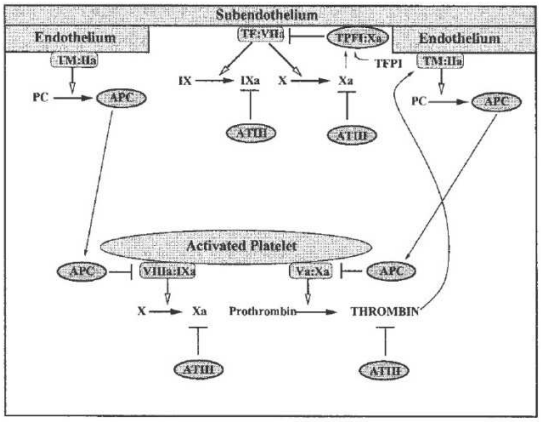

Figure 3.1 Backbone of the thrombus formation reaction system (upper left). Enzymatic feedback during thrombus formation (upper right). Chemical inhibition during thrombus formation (lower). [91]

One of the most popular tools modeling and understanding the mechanisms of thrombus formation is CRD (convection-reaction-diffusion) and CRD-like equations. One of the most comprehensive continuum CRD-like blood clotting model is the one introduced by Kuharsky & Fogelson [91]**.** The 'Kuharsky and Fogelson (KF) model' considers coagulation biochemistry, platelets activation, platelets deposition and the effect of the thrombus formation on the flow field; This procedure is shown in Figure 3.1. The KF model mainly describes the thrombus growth when there exists an exposed subendothelium by taking into account plasma-phase, subendothelial-bound and platelet-bound enzymes and zymogens as well as the activated and unactivated platelets, by considering the physical and chemical platelet and coagulation events that occur in a thin layer, called the reaction zone, just above a small vascular injury [93], which is not applicable for many practical cases, such as flow in various complex blood related medical devices. Sorensen et al. [1, 2] formulated another representative model based on CRD equations that platelet-biomaterial surface, which includes factors such as collagen and subendothelium, platelet-platelet adhesion, platelet activation by a weighted linear combination of agonist concentrations, agonist release and synthesis by the activated platelets, platelet-phospholipid-dependent thrombus generation, and thrombus inhibition by heparin [1, 2]. In Sorensen's model, the platelets are activated only by the agonists, ADP, thrombus and TxA_2. ADP is released by the unactivated platelets when activated, thrombus and TxA_2 are synthesized due to activated platelets, and the platelets-surface adhesion is modeled by some proper boundary flux conditions. All the parameters in Sorensen's model are available from experimental literatures or by fitting the experimental data. Shortcomings of this model are that it does not consider 1. the shear induced platelets activation which can be essential for blood flow in medical devices where the

exposed subendothelium does not exist, 2. the shear induced platelets activation which is essential for devices like blood pump, 3. The interaction between formatted thrombus and blood flow.

3.3 Mathematical model

Our thrombus model mainly includes two groups of equations: the blood flow equations and the convection-diffusion-reaction equations of chemical and biological species.

3.3.1 Blood (RBCs and plasma)

In this part of our work, we treat blood as a Newtonian fluid in practical applications in medical devices, such as blood pump, where the blood shear rate is always larger than 100 s^{-1}.

$$\frac{\partial \rho_f}{\partial t} + div(\rho_f \boldsymbol{v}_f) = 0 \tag{3.1}$$

$$\rho_f \frac{D\boldsymbol{v}_f}{Dt} = div(\boldsymbol{T}_f) + \rho_f \boldsymbol{b}_f - C_2(\boldsymbol{v}_f - \boldsymbol{v}_T) \tag{3.2}$$

where $\boldsymbol{T}_f = [-p(1-\phi)]\boldsymbol{I} + 2\mu_f(1-\phi)\boldsymbol{D}_f$, p is the pressure, μ_f is the dynamic viscosity which is 3.5cP, $\rho_f = (1-\phi)\rho_{f0}$, ρ_{f0} is the density of pure blood which is 1060 kg/m^3, ϕ is the volume fraction of deposited platelets(thrombus) and is defined as the ratio of deposited platelets concentration and maximum platelets concentration in space, $\boldsymbol{b}_f$ is the body force, $\boldsymbol{v}_f$ and $\boldsymbol{v}_T$ are the velocity of blood and the thrombus (Usually $\boldsymbol{v}_T$ is equal to 0m/s, when the wall/surface where thrombus grew from is static, but when the wall/surface is moving, such as the surface of a impeller of a blood pump, the $\boldsymbol{v}_T$ is not equal to 0m/s.), $C_2(\boldsymbol{v}_f - \boldsymbol{v}_T)$ is the resistance force on the blood from the thrombus and $C_2 = 1 \times 10^9$ is a parameter which is chosen by borrowing the idea from drag force and assuming deposited platelets behave like densely compacted particles (see Johnson et al. [94] and Wu et al[66]). Alternatively, the resistance force

can also be treated as a Brinkman-type term using ideas in porous media modeling (see Leiderman and Fogelson [93]).

3.3.2 Thrombus: Chemical and biological species

All chemical and biological species are assumed to be different, and described by convection-diffusion-reaction equations [1, 2]

$$\frac{\partial [C_i]}{\partial t} + div\big(\boldsymbol{v}_f \cdot [C_i]\big) = div(D_i \cdot \nabla [C_i]) + S_i \tag{3.3}$$

where D_i refers to the diffusivity of species i in blood; $[C_i]$ is the concentration of species i; and S_i is a reaction source term for species i. The species considered in the current model are: 1. normal(unactivated) resting platelets, [RP]; 2. activated resting platelets, [AP]; 3. platelet-granule-released, $[a_{pr}]$, and platelets synthesized platelet agonists, $[a_{ps}]$, which can be inhibited via first-order reactions; 4. prothrombus, [PT]; 5. thrombus, [T], generated from prothrombus on platelet phospholipid membranes; and 6. ATIII, [AT], which inhibits thrombus and whose action is catalyzed by heparin via the kinetic model of Griffith. Table 3.1 lists the appropriate form for the source terms S_i, along with the abbreviation and the units used for $[C_i]$, for each species included in the model. Besides the species introduced above, we also have three other species (deposited platelets), namely deposited unactivated/activated platelets, $[RP_d]$/$[AP_d]$, and stabilized deposited activated platelets, $[AP_s]$, which do not have convection and diffusion terms,

$$\frac{\partial [C_i]}{\partial t} = S_i \tag{3.4}$$

The source terms, the abbreviation and units used for these three species are listed in Table 3.2. At the boundary, platelet-surface adhesion and all the other species reactions are modeled by surface-flux boundary conditions. Here similar to the reaction terms in the internal domain, the

negative flux implies consumption and the positive flux implies generation. Following the ideas of Sorenson et al. [1, 2], the expressions and description of the species boundary conditions are listed in Table 3.3. The value or the expression and the description of all the source terms and parameters are summarized in the Appendix for easy understanding.

Table 3.1. Model species and reaction source terms.

Species	$[C_i]$ abbreviation	S_i form
Unactivated Resting PLT	[RP]	$-k_{apa}[RP] - k_{spa}[RP] + f_{emb}[RP_d] - k_{rpd}[RP]$
Activated PLT	[AP]	$k_{apa}[RP] + k_{spa}[RP] + f_{emb}[AP_d] - k_{apd}[AP]$
PLT-released agonists (ADP)	$[\mathrm{a_{pr}}]$	$\lambda_j\left(k_{apa}[RP] + k_{spa}[RP] + k_{apa}[RP_d] + k_{spa}[RP_d] + \theta k_{rpd}[RP]\right) - k_{1,j}[\mathrm{a_{pr}}]$
PLT-synthesized agonists (TxA_2)	$[\mathrm{a_{ps}}]$	$s_{pj}([AP] + [AP_d]) - k_{1,j} \cdot [\mathrm{a_{ps}}]$
Prothrombus	[PT]	$-\varepsilon[\mathrm{PT}]\left(\phi_{at}([AP] + [AP_d]) + \phi_{rt}([RP] + [RP_d])\right)$
Thrombus	[T]	$-\Gamma \cdot [T] + [\mathrm{PT}]\left(\phi_{at}([AP] + [AP_d]) + \phi_{rt}([RP] + [RP_d])\right)$
ATIII	[AT]	$-\Gamma \cdot \varepsilon[T]$

Table 3.2. Model species and reaction source terms.

Species	$[C_i]$ abbreviation	S_i form
Deposited Resting PLT	$[\mathrm{RP_d}]$	$(1-\theta)k_{rpd}[RP] - k_{apa}[RP_d] - k_{spa}[RP_d] - f_{emb}[RP_d]$

Deposited Activated PLT	$[AP_d]$	$\theta k_{rpd}[RP] + k_{apd}[AP] + k_{apa}[RP_d] + k_{spa}[RP_d] - (f_{emb} + f_{stb})[AP_d]$
Deposited and stabilized PLT	$[AP_s]$	$f_{stb}[AP_d]$

Table 3.3(a). Species boundary conditions.

Species $[C_i]$	j_i form	Description
[RP]	$-Sk_{rpdb}[RP] + f_{embb}[RP_d]$	Consumption due to [RP]-Surface adhesion; Generation due to shear embolization.
[AP]	$-Sk_{apdb}[AP] + f_{embb}[AP_d]$	Consumption due to [AP]-Surface adhesion; Generation due to shear embolization.
$[a_{pr}]$	$\lambda_j(k_{apa}[RP_d] + k_{spa}[RP_d] + \theta Sk_{rpdb}[RP])$	Generation due to agonists and shear activation of $[RP_d]$; Generation due to surface contact activation of [RP]-Surface adhesion.
$[a_{ps}]$	$s_{pj}[AP_d]$	Platelet-synthesized generation due to $[AP_d]$
[PT]	$-\varepsilon[\mathrm{PT}](\phi_{at}[AP_d] + \phi_{rt}[RP_d])$	Consumption due to thrombus, [T], generation.
[T]	$[\mathrm{PT}](\phi_{at}[AP_d] + \phi_{rt}[RP_d])$	Generation from prothrombus [PT] due to deposited platelets.
[AT]	0.0	No reaction flux

Table 3.3(b) Species boundary conditions.

$[RP_d]$	$\int_0^t (1-\theta)Sk_{rpdb}[RP] - k_{apa}[RP_d] - k_{spa}[RP_d] - f_{embb}[RP_d]dt$	Generation due to [RP]-Surface adhesion; Consumption due to agonists and shear activation; Consumption due to shear embolization.
$[AP_d]$	$\int_0^t Sk_{apdb}[AP] + \theta Sk_{rpdb}[RP] + k_{apa}[RP_d] + k_{spa}[RP_d] - (f_{embb} + f_{stb})[AP_d]dt$	Generation due to [AP]-Surface adhesion; Generation due to surface contact activation of [RP]-Surface adhesion; Generation due to agonists and shear activation of [RP]; Consumption due to shear embolization and stabilization.
$[AP_s]$	$\int_0^t f_{stb}[AP_d]\,dt$	Generation due to stabilization.

3.4 Results and discussion

A CFD solver for the mathematical model described above is developed using the solvers and the libraries of OpenFOAM®, a C++ toolbox for the development of customized numerical solvers, and pre-/post-processing utilities for the solution of continuum mechanics problems, including computational fluid dynamics (CFD) [95]. The values and the expressions for all the material parameters used here are summarized in the Appendix. For each geometry studied, the domain is discretized as hexahedral meshes using ICEM. In each of the cases, mesh-dependence studies were performed to assure insensitivity to the mesh size.

Platelets deposition in blood vessel with ADP injection: the effect of the mean velocity on the shape of the deposited platelets

Begent and Born [96] and Born and Richardson [97] studied the effect of the mean velocity on the shape of the platelet thrombi produced by Iontophoresis of ADP *in vivo* in hamsters. The schematic of the simulated blood vessel is shown in Figure 3.2. The inlet velocity is $800\mu m/s$ and $1800\mu m/s$. The reaction rates and the embolization rate for current case are $k_{ra} = 7.0 \times 10^{-7}\mathrm{m/s}$, $k_{aa} = 2.5 \times 10^{-5}\mathrm{m/s}$ and $k_{emb} = 0.9 \times 10^{-6}\mathrm{m/s}$; and the embolization rate and the platelets deposition rate at the ADP injecting spot, where the vessel is injured, are $k_{embb} = 1.0 \times 10^{-5}\mathrm{m/s}$, $k_{rpdb} = 4.0 \times 10^{-7}\mathrm{m/s}$ and $k_{apdb} = 4.0 \times 10^{-4}\mathrm{m/s}$. It should be emphasized that in current case the effect of the boundary parameters on the shape of the thrombus is moderate, compared with the parameters, such as k_{ra}, k_{aa} and so on. All the other general parameters see Appendix. The inlet [RP] and [AP] are 5×10^{14} and 5×10^{12}. Figure 3.4 and Figure 3.5 show a snapshot of thrombus at different time steps. It can be seen that thrombus grow towards both upstream and downstream, which agrees with the experimental observation by Begent and Born [96] [see Figure 3.6]. The upstream growth may be due to the capture of the incoming platelets and the relatively low shear rates; while the platelets needed for the downstream growth are supplied by the platelets in the flow and also removed platelets by shear from the neighboring upstream. Figure 3.7 shows the comparison of the height versus the length of the thrombus observed experimentally and the numerically. From the figures, we can find that the model clearly catches the effect of the mean velocity on the shape of the thrombi and agree with the experiments very well. The curve in Figure 3.7 quantitatively validates our model and simulation.

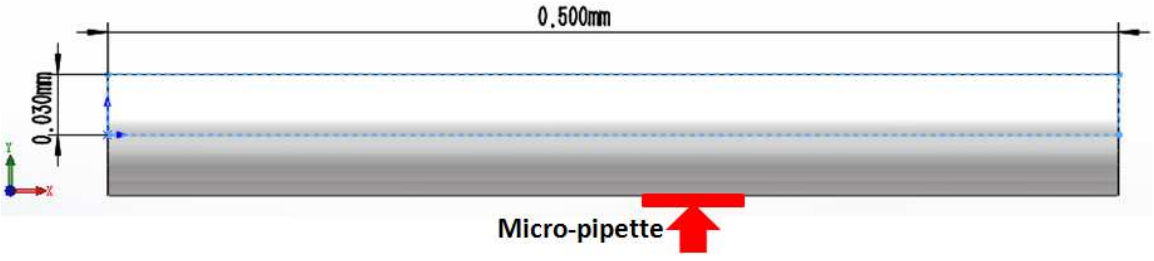

Figure 3.2 Schematic of the simulated blood vessel. The diameter of the simulated blood vessel is 0.06mm and the length is 0.5mm. The ADP injection part locates at the bottom vessel wall and its diameter is $3\mu m$ which is the diameter of the micro-pipette injecting the ADP using iontophoretic method. [96, 97] In this problem, we set only the injection spot area, which is injured, is highly adhesive to the unactivated and activated platelets; Reset of the healthy vessel wall is little adhesive to the platelets, because normal and healthy blood vessel is able to produce inhibiting agonist resisting platelets deposition.

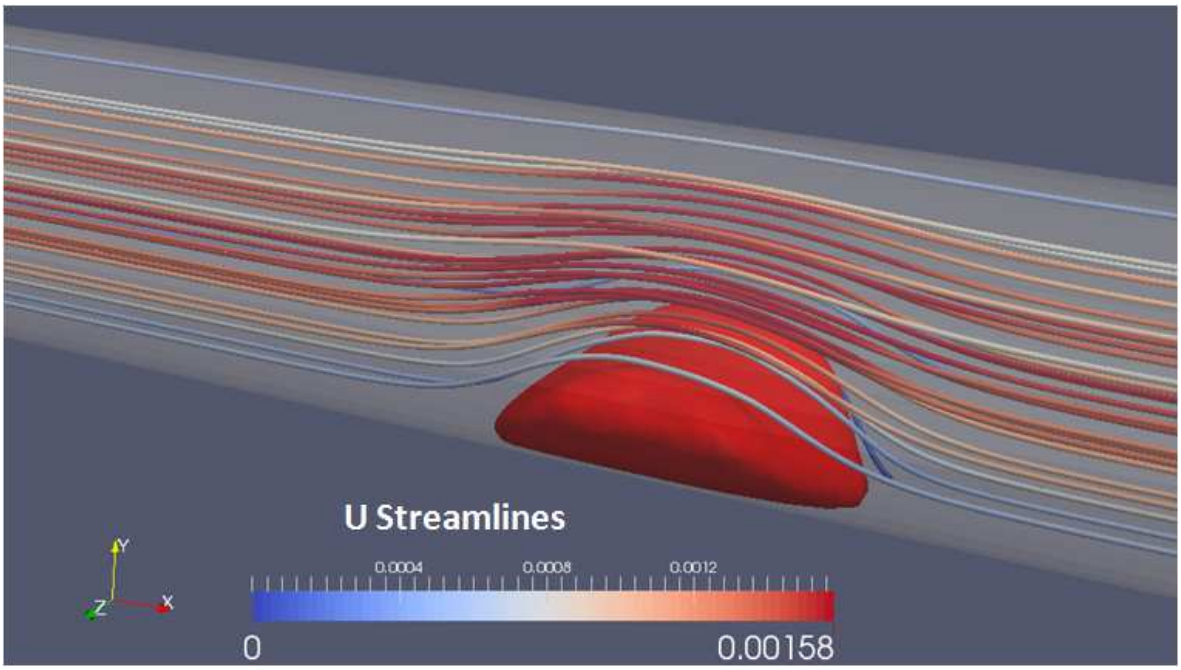

Figure 3.3 (a) Snapshots of thrombus and streamline after simulated for 450s at mean velocity $800\mu m/s$. The red body is the thrombus, and it is plotted in the region where the volume fraction of the deposited thrombus is larger than 0.3.

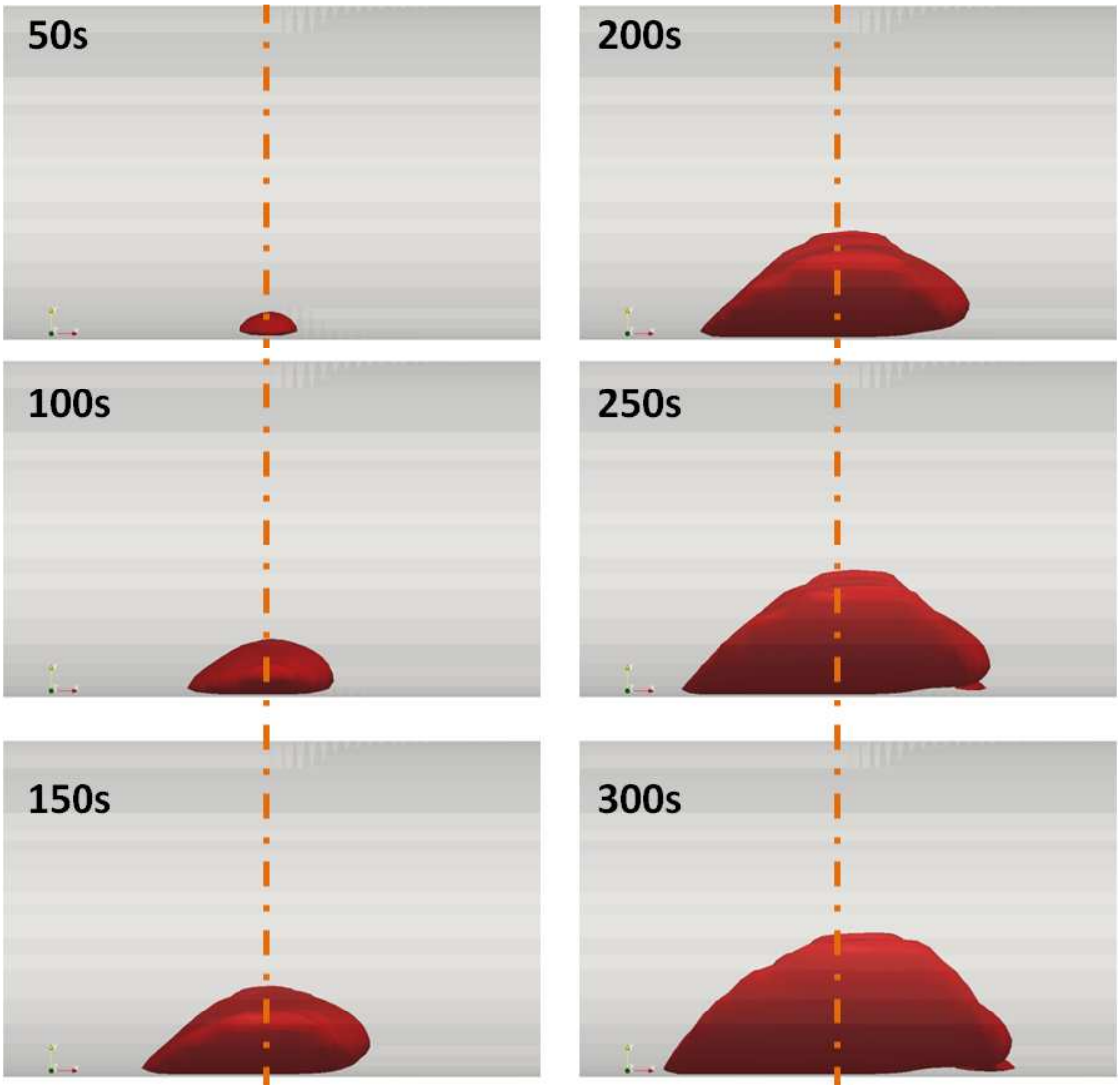

Figure 3.4 Procedure of the thrombus growth at mean velocity $800 \mu m/s$.

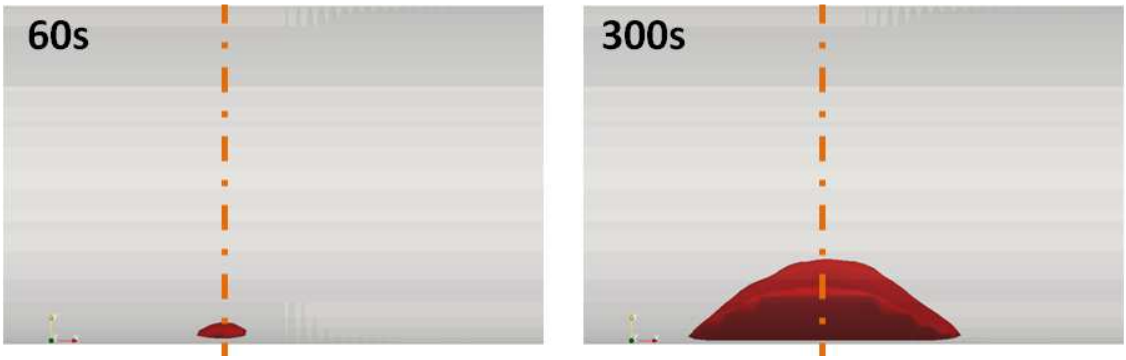

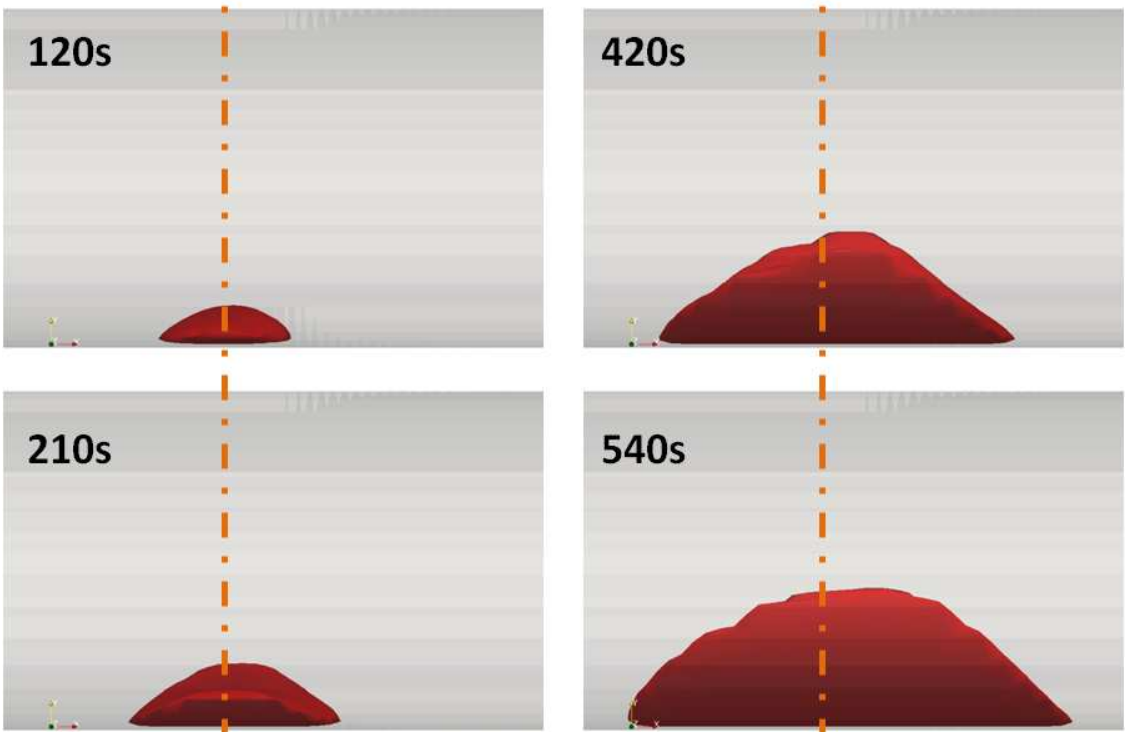

Figure 3.5 Procedure of the thrombus growth at mean velocity $1800 \mu m/s$.

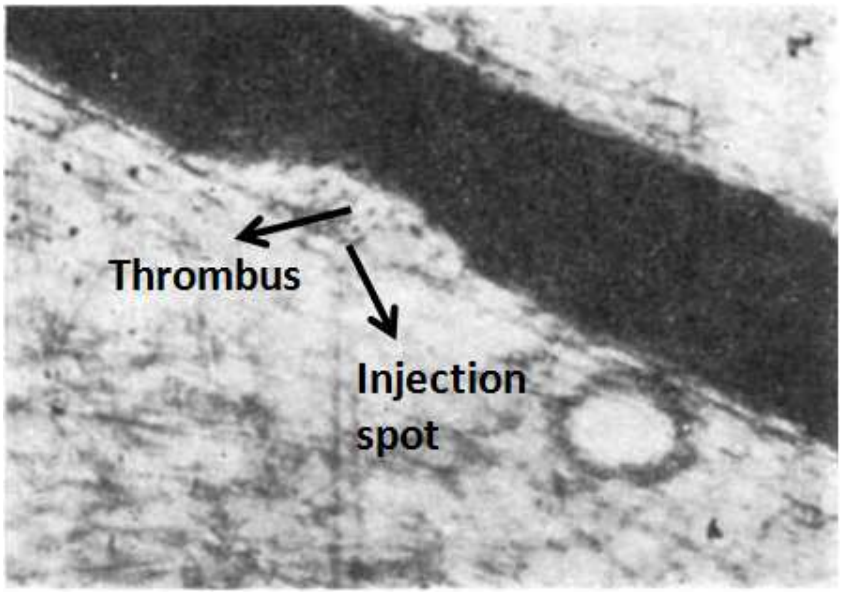

Figure 3.6 Snapshot of the thrombus created and measured by Begent and Born [96].

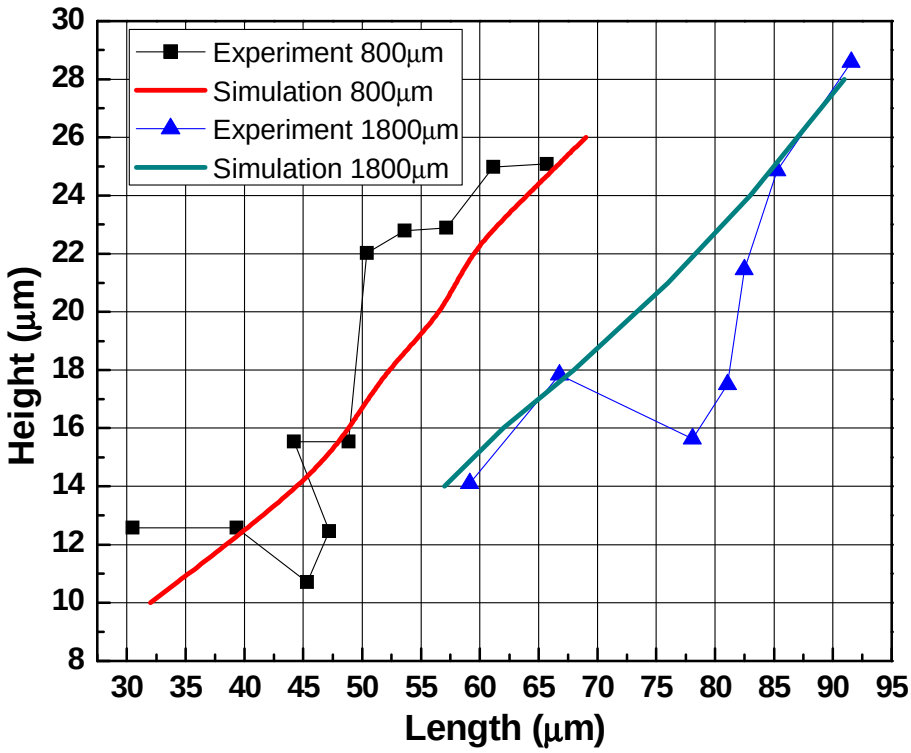

Figure 3.7 Thrombus height VS length by numerical simulation and experiments. Experimental data is from [96, 97].

Figure 3.8 shows the streamlines and a snapshot of different species fields on the radial-axial slice plane. Figure 3.8(a), the streamlines indicate that in the region occupied by the thrombus no fluid flows. This produces vessel stenosis if these newly created thrombus stabilizes. Figure 3.8(b) indicates that near the surface of the thrombus the shear rate is much higher than other places and it will become greater as the size of the thrombus increases which implies that the platelets deposition will be more difficult due to shear embolization. Figure 3.8(c)-(h) show that agonists concentrate near the surface of the thrombus and they activate the resting platelets and make them maintain a high concentration there, which supports the thrombus propagation.

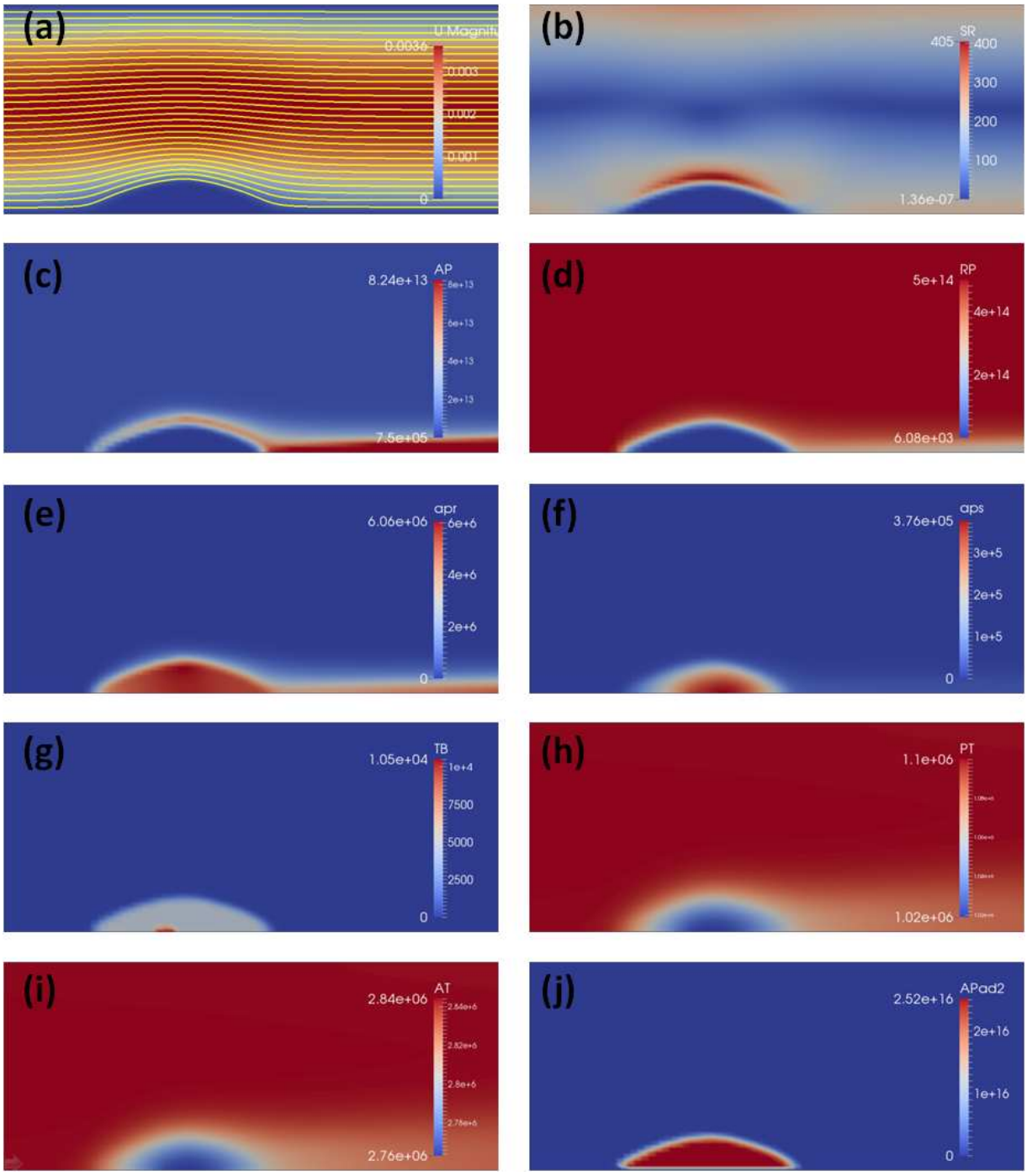

Figure 3.8 The streamline, shear rate and different species fields on the radial-axial slice plane: (a) Streamline; (b) Shear rate field; (c) Activated platelets; (d) Unactivated resting platelets; (e) PLT-released agonists (ADP); (f) PLT-synthesized agonists (TxA_2); (g) Thrombus; (h) Pro-thrombus; (i) ATIII; (j) Deposited activated platelets (thrombus). The plane penetrates the middle of the ADP injection spot. The mean velocity is $1800\mu m/s$ and the time step is 450s.

Platelets deposition in rectangular channel with a crevice

A further benchmark problem, namely, a rectangular channel with a crevice, will be studied. This is motivated by a persistent problem involved in most blood wetted devices, namely the seams and joints between component parts of a device or flow circuit which are predisposed to thrombus deposition (See Figure 3.9). It should be noted that in the previous study, the experiments were performed on mouse, while in the current study the experimental material is the human blood which implies that the model parameters may be moderately different.

It is widely believed that the platelets deposition rate is similar for all mammalian. Therefore the parameters, such as the embolization rate, $k_{emb} = 0.9 \times 10^{-6}\mathrm{m/s}$, and the platelets deposition rates, $k_{ra} = 7.0 \times 10^{-7}\mathrm{m/s}$ and $k_{aa} = 2.5 \times 10^{-5}\mathrm{m/s}$, obtained in the previous simulation are applied in current case. The embolization rate and wall-platelets deposition rates, which varies depending on the wall property, are chosen to be different to the previous case, $k_{embb} = 1.4 \times 10^{-5}\mathrm{m/s}$,, $k_{rpdb} = 1.0 \times 10^{-20}\mathrm{m/s}$ and $k_{apdb} = 2.0 \times 10^{-5}\mathrm{m/s}$. The inlet [RP] and [AP] is 3×10^{14} and 1×10^{13}.

Figure 3.10 shows the concentration field for the deposited platelets of based on the numerical predictions and the experiments, after simulation has run for 600s. It can be observed that a very good agreement is achieved. At the region B shown in Figure 3.10 (rear corner of the crevice), numerous platelets deposited. Furthermore, there is a lot of deposited platelets at the wall neighboring to the rear corner, which is counterintuitive, because both numerical and experimental results show that plane wall at the upstream of the crevices does not have serious platelets deposition. In other words, the platelets deposition at the walls located immediately after the crevices should contribute to the crevice which provides the nidus for platelets

activation and also provides the activated platelets for platelets deposition at the downstream wall of the crevice. Those platelets which are activated in the crevices by shear, agonists or contact with the deposited platelets will not be totally captured in the crevices.

Through the experimental and numerical results, the enhancement of the crevices on the thrombus formation can be clearly seen. As mentioned previously, these kinds of crevices exists widely in various blood wetted devices as the seams and joints which become potential sites for thrombus. In addition, from the experimental results, it also can be seen that at the entrance regions near the corner of the crevices some thrombus are also deposited; this is observed in our simulations, as well. This further validates our mathematical model.

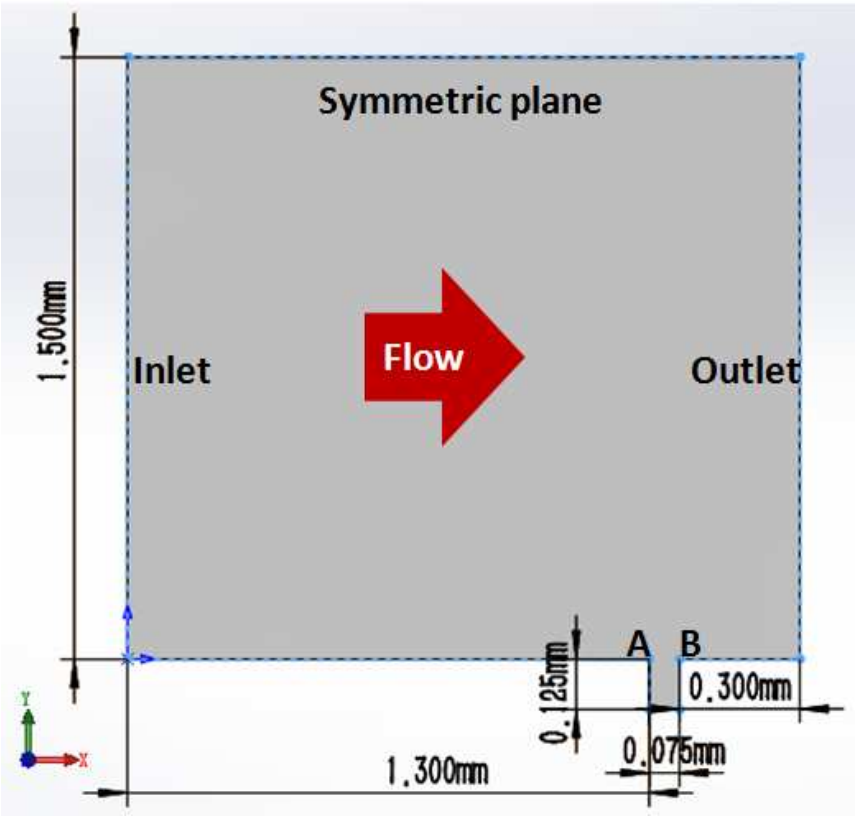

Figure 3.9 Schematic of the rectangular channel with a crevice. The half of the channel height is 1.5mm, the total length of the channel is 1.6075mm and the depth is 0.1mm. The height and length of the crevice is 0.125mm and

0.075mm. The inlet velocity is 0.0173m/s (Re=32.30). A: upstream corner of the crevice; B: rear corner of the crevice.

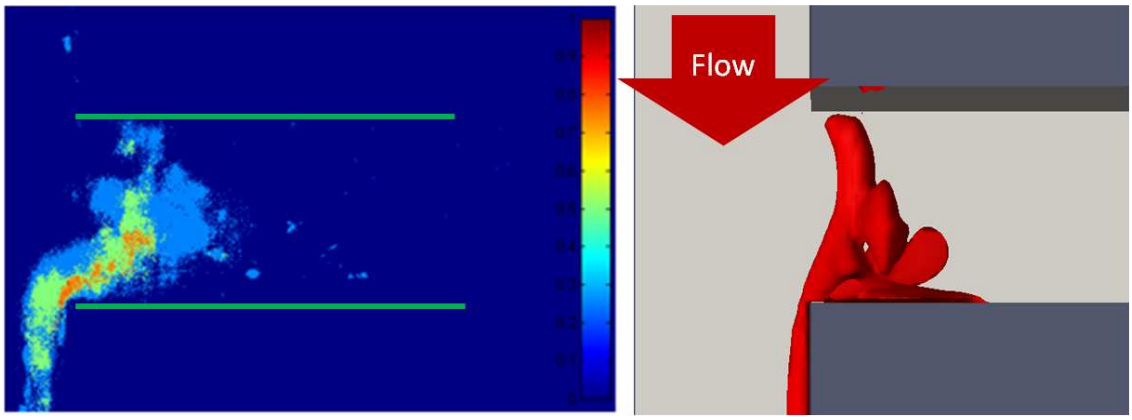

Figure 3.10 (a) Thrombus concentration field by experiment after 600s; (b) Thrombus concentration field by numerical simulation at 600s.

Figure 3.11 shows a few snapshots of the thrombus concentration field at different time steps. From the figures, it can be seen that the thrombus growth starts form the corner and wall centre of crevices. As time passes , at the rear corner, the amount of the accumulated deposited platelets become more dominant. This may be because at the rear corner, except for the platelets which were activated locally, a lot of platelets are activated without being deposited at the beginning corner and are transported to the rear corner where they are captured. This makes the growth rate of the thrombus at the rear corner much faster. When the deposited thrombus at the rear corner accumulates to a certain, rather large value the agonists produced by those deposited platelets become dense enough to activate the unactivated surrounding platelets. In this region, the amount of the platelets activated by agonists will be much larger than those activated by the shear stress, which indicates an even much faster thrombus deposition at the rear corner.

At the downstream wall of the rear corner, gradually the thrombus is growing, which is an unexpected result since plane wall at the upstream of the crevices does not have serious platelets deposition. Here we should emphasize again that a crevice plays a very important role (as the

nidus) in the thrombus formation in the blood wetted devices. If there are no crevices, the thrombus growth may be very slow. The slow or no growth of thrombus is indeed great news for those who need to use blood wetted devices.

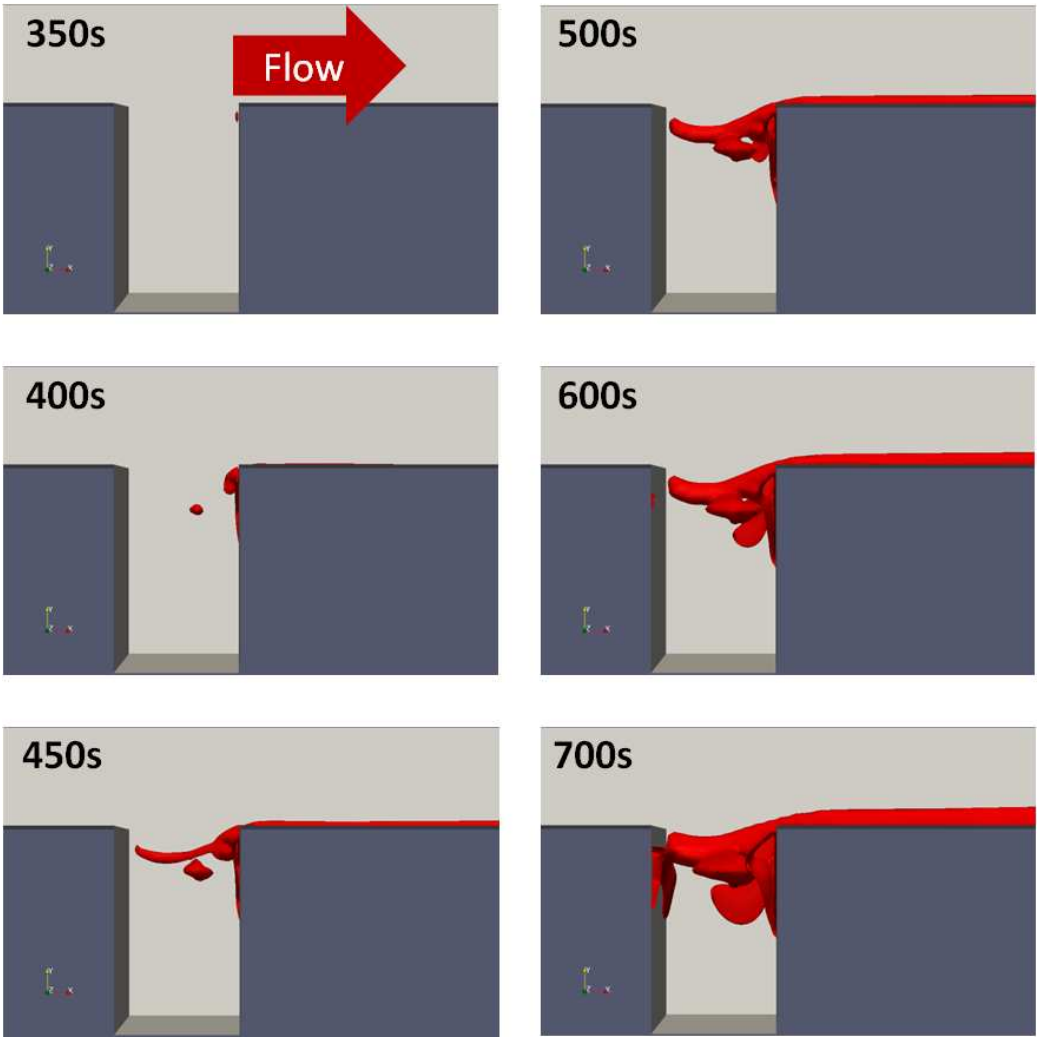

Figure 3.11 Evolution of thrombus growth in rectangular crevice.

Figure 3.12 shows the streamline and snapshot of computation fields of different species. From the figures, it can be seen that in surrounding areas of the thrombus, including those in and out of the crevices, the concentration of the activated platelets is high. These activated platelets, except those which are consumed locally, are transported to the downstream, such as the rear of the

thrombus, see Figure 3.12. These activated platelets cause the thrombus to become larger and also propagate further downstream.

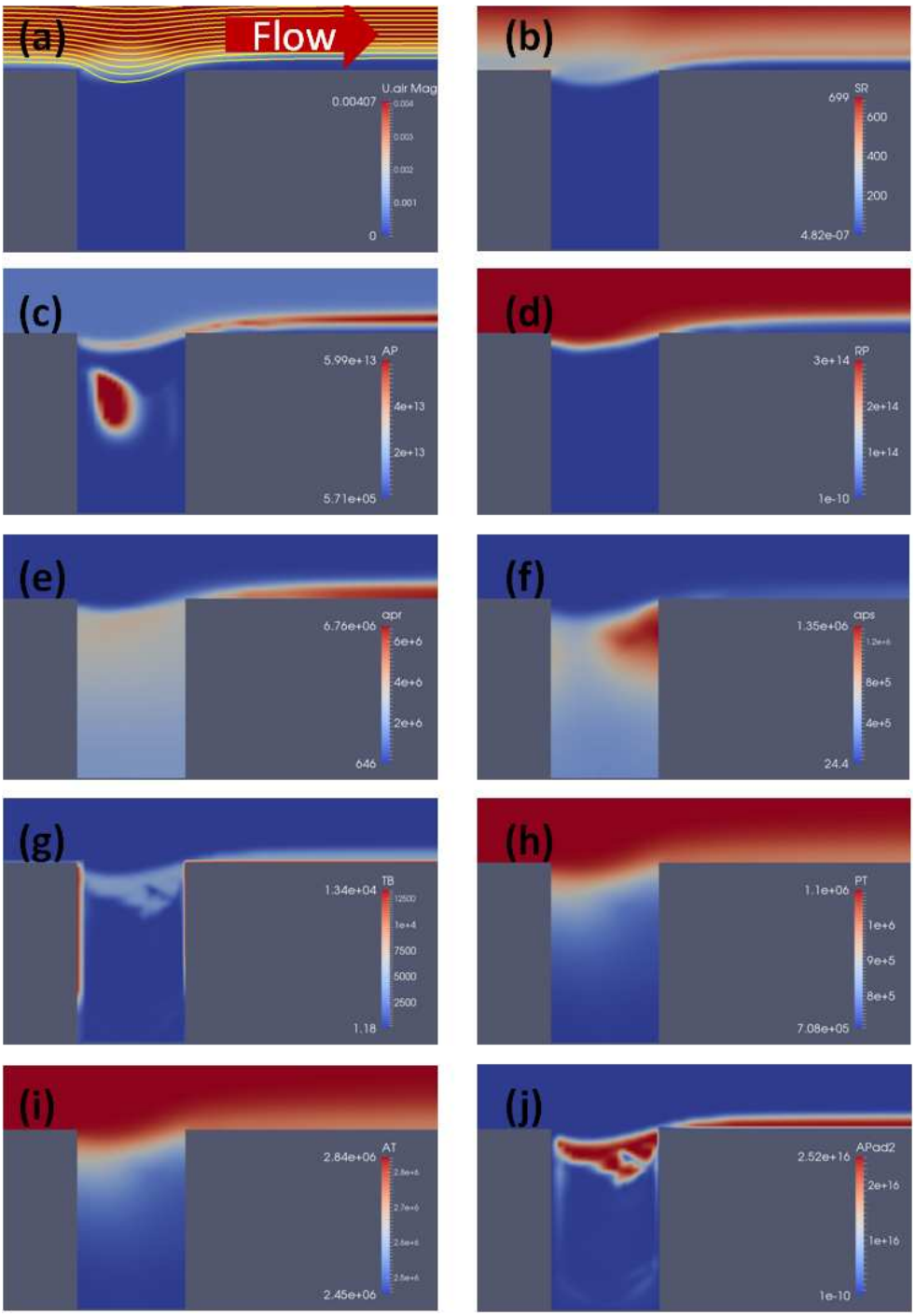

Figure 3.12 The streamline, shear rate and different species fields on the x-y slice plane at depth z=10μm: (a) Streamline; (b) Shear rate field; (c) Activated platelets; (d) Unactivated resting platelets; (e) PLT-released agonists (ADP); (f) PLT-synthesized agonists (TxA_2); (g) Thrombus; (h) Pro-thrombus; (i) ATIII; (j) Deposited activated platelets (thrombus). The time step is 700s.

3.5 Summary

In this chapter, based on the Sorenson's model [1, 2], a mathematical model for describing the process of thrombus growth is developed. The model includes blood flow modeled as a single phase Newtonian fluid, and transport and reactions of thrombus growth which is modeled by convection-diffusion-reaction (CDR) equations. The advantage of using CDR equations is their continuity, which enables their applicability to complex and practical thrombus related problems, such as those observed in medical devices likes blood pumps. Our model systematically considers the three thrombus growth processes : 1. Initiation, which considers the platelets-boundary (wall) deposition; 2. Propagation which looks at the agonists activation of platelets and platelets-deposited platelets deposition; and 3. Stabilization which account for newly deposited platelets that are converted to be solid like colt which cannot be removed by hydrodynamic force. The model also includes the interaction between the thrombus and blood flow: 1. thrombus resists the flow; and 2. the shear stress removes the newly deposited platelets on the surface of thrombus. We applied this model to two representative benchmark problems a blood vessel with ADP injection and a rectangular channel with a crevice. The numerical results show very good agreements with the experimental data which encourages future study of other practical problems, such as cardiovascular devices.

3.6 Appendix

Appendix 1.1 Value, expression and description of the parameters, coefficient and reaction source terms.

Table 3.4. Species units, coefficient of species diffusion and initial condition. γ is the local shear rate. For more detail see Sorenson[1, 2] and Goodman[98].

Species	Species units	$D_i(m^2s^{-1})$	Initial (inlet) condition in blood
[RP]	PLT m^{-3}	$1.58 \times 10^{-13} + 6.0 \times 10^{-13}\gamma$	$1.5 \times 10^{14} - 3.0 \times 10^{14}$(Human) $1.9 \times 10^{14} - 10.0 \times 10^{14}$(Mouse)
[AP]	PLT m^{-3}	$1.58 \times 10^{-13} + 6.0 \times 10^{-13}\gamma$	$0.01[\mathrm{RP}] - 0.05[\mathrm{RP}]$
$[a_{pr}]$	nmol m^{-3}	2.57×10^{-10}	0.0
$[a_{ps}]$	nmol m^{-3}	2.14×10^{-10}	0.0
[PT]	nmol m^{-3}	3.32×10^{-11}	1.1×10^{6}
[T]	Um^{-3}	4.16×10^{-11}	0.0
[AT]	nmol m^{-3}	3.49×10^{-11}	2.844×10^{6}
$[RP_d]$	PLT m^{-3}	N/A	0.0
$[AP_d]$	PLT m^{-3}	N/A	0.0
$[AP_s]$	PLT m^{-3}	N/A	0.0

Table 3.5. Value or expression and description of reaction terms and parameters in current chapter.

Terms	Value or expression	units	Description
k_{apa}	$\begin{cases} 0, \Omega < 1.0 \\ \frac{\Omega}{t_{ct}}, \Omega \geq 1.0 \\ \frac{1}{t_{act}}, \frac{\Omega}{t_{ct}} \geq \frac{1}{t_{act}} \end{cases}$	(s^{-1})	Platelets activation due to agonists; t_{ct} is the characteristic time, which can be used for adjusting the activation rate, and here we choose $t_{ct} = 1s$ as provided Sorenson [1, 2]; $k_{apa} = \frac{1}{t_{act}}, \frac{\Omega}{t_{ct}} \geq \frac{1}{t_{act}}$ implies the reaction cannot be faster than physical platelets activation procedure and 99%

			platelets will be activated during the activation procedure if the agonists or shear stress is large enough. t_{act} is the characteristic time; t_{act} is suggested to range from 0.1s to 0.5s considering the results by Frojmovic et. al [99] and Richardson [100].
Ω	$\sum_{j=1}^{n_a} w_j \frac{a_j}{a_{j,crit}}$	(N/A)	a_j refers to the concentration of ADP, TxA_2 and Thrombus. Value of w_j and $a_{j,crit}$ see Table 3.6
k_{spa}	$\frac{1}{t_{ct,spa}}$ $= \begin{cases} \frac{1}{4.0 \times 10^6 \tau^{-2.3}}, t_{ct,spa} > t_{act} \\ \frac{1}{t_{ct,spa}}, t_{ct,spa} < t_{act} \end{cases}$	(s^{-1})	Platelet activation due to shear stress, τ. Expression $t_{ct,spa} = 4.0 \times 10^6 \tau^{-2.3}$ was provided by Goodman[98] and Hellums[86].
k_{rpd}	$div(k_{pd,f}\vec{\boldsymbol{n}})k_{ra}$	(s^{-1})	Unactivated platelets - deposited activated platelets ([RP]-[AP_d]), deposition rate. f refers to the face of a mesh cell and $\vec{\boldsymbol{n}}$ is the unit normal to the face. Detail about how this term is calculated are provided in Appendix 1.2.
k_{ra}	To be determined, depends on blood material.	($m\ s^{-1}$)	Constant related to k_{rpd}.
k_{apd}	$div(k_{pd,f}\vec{\boldsymbol{n}})k_{aa}$	(s^{-1})	Activated platelets-deposited activated platelets ([AP]-[AP_d]) deposition rate. Detail about how this term is calculated are

			provided in Appendix 1.2.
k_{aa}	To be determined, depends on blood material.	(m s^{-1})	Constant related to k_{apd}.
f_{emb}	$k_{emb} div(k_{emb,f}\vec{n})$ $\cdot (1 - exp(-0.0095\tau))$	s^{-1}	Platelet embolization due to shear stress; Expression $exp(-0.0095\tau)$ was suggested by Goodman[98].
$k_{emb,f}$	$k_{emb,f} = \begin{cases} 1, & k_{pd,f} > 0 \\ 0, & k_{pd,f} = 0 \end{cases}$	(N/A)	
k_{emb}	To be determined, depends on blood material.	ms^{-1}	Platelet shear embolization related constant.
f_{embb}	$\frac{k_{embb}}{Dia_{PLT}}$ $\cdot (1 - exp(-0.0095\tau))$	s^{-1}	Platelet embolization in boundary due to shear stress. $Dia_{PLT} = 2.78 \times 10^{-6} m$ is the diameter of platelets.
k_{embb}	To be determined, depends on blood material.	ms^{-1}	Platelet shear embolization related constant.
PLT_{max}	$\frac{PLT_{s,max}}{Dia_{PLT}}$	PLT m^{-3}	The maximum concentration of platelets in space. $PLT_{s,max} = 7 \times 10^{10} PLT m^{-2}$ is the total capacity of the surface for platelets; $Dia_{PLT} = 2.78 \times 10^{-6} m$.
λ_j	2.4×10^{-8}	nmol PLT^{-3}	The amount of agonist j released per platelet.
θ	1.0	(N/A)	Platelets activation by contact.
$k_{1,j}$	0.0161	(s^{-1})	The inhibition rate of agonist.
s_{pj}	9.5×10^{-12}	nmol PLT^{-3}	The rate of synthesis of an agonist.
ε	9.11×10^{-3}	nmol U^{-1}	Unit conversion. From NIH units to SI

			units.
ϕ_{at}	3.69×10^{-15}	$\mathrm{m^3\ nmol^{-1}\ PLT^{-1}\ U\ s^{-1}}$	Thrombus generation rate on the surface of activated platelets
ϕ_{rt}	6.5×10^{-16}	$\mathrm{m^3\ nmol^{-1}\ PLT^{-1}\ U\ s^{-1}}$	Thrombus generation rate on the surface of unactivated platelets
Γ	$\frac{k_{1,T}[H][AT]}{\alpha K_{AT} K_T + \alpha K_{AT} \varepsilon[T] + [AT]\varepsilon[T]}$	$(\mathrm{s^{-1}})$	Griffith's template model for the kinetics of the heparin-catalyzed inactivation of thrombus by ATIII.
$k_{1,T}$	13.333	$(\mathrm{s^{-1}})$	A first-order rate constant.
$[H]$	2.09×10^6	$\mathrm{nmol\ m^{-3}}$	Heparin concentration
α	1.0	(N/A)	A factor to simulate a change in affinity of heparin for ATIII when it is bound to thrombus or for thrombus when it is bound to ATIII.
K_{AT}	0.1×10^6	$\mathrm{nmol\ m^{-3}}$	The dissociation constant for heparin/ATIII.
K_T	3.50×10^4	$\mathrm{nmol\ m^{-3}}$	The dissociation constant for heparin/thrombus.
S	$1 - \frac{[RP_{db}] + [AP_{db}] + [AP_{sb}]}{PLT_{s,max}}$	(N/A)	Percentage of the wall (boundary) not been occupied by deposited platelets.
k_{rpdb}	To be determined, depends on blood material.	$(\mathrm{m\ s^{-1}})$	Unactivated platelets-boundary(wall) deposition rate.
k_{apdb}	To be determined, depends on blood material.	$(\mathrm{m\ s^{-1}})$	Activated platelets-boundary(wall) deposition rate.

f_{stb}	0.0	(s^{-1})	Deposited activated platelets stabilization rate.
ϕ	$\frac{RP_d + AP_d + AP_s}{PLT_{max}}$	(N/A)	Volume fraction of deposited platelets

Table 3.6. Threshold concentration of that agonist for platelet activation and agonist-specific weight. For more detail see Sorenson [1, 2] and Goodman[98].

Species	$a_{j,crit}$	w_j
ADP($[a_{pr}]$)	$2.00 \times 10^6 \text{nmol m}^{-3}$	1
TxA_2($[a_{ps}]$)	$0.60 \times 10^6 \text{nmol m}^{-3}$	3.3
Thrombus([T])	$0.01 \times 10^6 \text{Um}^{-3}$	220

Appendix 1.2 Unactivated/activated platelets-deposited activated platelets deposition rate

k_{rpd} and k_{apd} represent the unactivated/activated platelets-deposited activated platelets deposition rate. In other words, the rate of the resting unactivated/activated platelets captured by the deposited activated platelets. The k_{rpd} of cell 5 is calculated as, see Figure 3.13 (assume cell 1, 2 and 3 are the boundary cells having boundary face B1, B2 and B3.),

$$k_{rpd} = div\left(k_{pd,f}\vec{\boldsymbol{n}}\right)k_{ra}$$

f refers to the faces shared by cells 2-5, 4-5, 5-6 and 5-8. Considering that thrombus tends to grow layer by layer otherwise it may be easily cleaned by hydrodynamic force, we assume that when the volume fraction of the deposited platelets of a cell is larger than some value (here chosen as 0.8 which is a little larger than 0.74 (the maximum packing of sphere), considering the non-uniform size of platelets which leads to higher possible maximum packing), this cell is able

to influence the neighbor cells, $k_{pd,f} = \frac{[RP_d]_f + [AP_d]_f + [AP_s]_f}{PLT_{max}} > 0$. $\frac{[RP_d]_f + [AP_d]_f + [AP_s]_f}{PLT_{max}}$ represents the percentage of the area occupied by deposited activated platelets at that mesh surface and those deposited activated platelets are going to capture incoming platelets. We also consider that in some zone where the velocity of the fluid is extremely slow, the thrombus may not grow layer by layer but more loosely, therefore we also set that current cell is able to influence the neighbor cells when $\left|(1-\phi)(\boldsymbol{v}_f - \boldsymbol{v}_T)\right|$ is smaller than some value, which means effect of the fluid on the thrombus is small and the thrombus is stable. For instance, using cell 2 as considered cell, if volume fraction of cell 2 is smaller than 0.8 and if $\left|(1-\phi)(\boldsymbol{v}_f - \boldsymbol{v}_T)\right|$ of cell 2 is larger than $1 \times 10^{-6} m/s$, $k_{pd,f}$ of the faces shared by cells 1-2, 2-3 and 2-5 will be considered as $k_{pd,f} = 0$ which implies $k_{pd,f}$ related to cell 2 is ignored. In addition, this is not applied to the boundary faces.

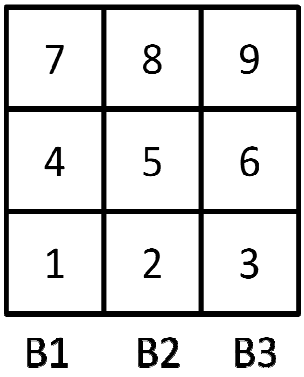

Figure 3.13 Schematic of cells and faces of a mesh.

Chapter 4 Direct prediction of thrombus formation in an axial flow blood pump

4.1 Introduction

VADs have significantly contributed to improve survival in end stage heart failure patients and have now been implanted over in about 10,000 patients worldwide.[101] However, the complication rates associated VADs especially for thromboembolism, infection, and bleeding have limited wider adoption of VADs.[102] Serious complications, such as bleeding and stroke, jeopardizes the quality of life of patients, and may require pump exchange or result in death due to pump thrombus (PT). Initially developed when transplant waiting times were less than 30 days, pulsatile VADs are now regularly used to support patients for over 1 year.[103] Consequently, durability issues have arisen in these long-term support cases. More recently rotary VADs have been developed due their superior durability, lack of valves, absence of a compliance chamber or requirement for external venting, and their smaller size, which reduces infection potential and provides better anatomic fit in smaller patients.[27, 104, 105]

As opposed to pulsatile VADs, which generate flow through the compression of a blood-containing chamber in the same manner as the native heart, a rotary VAD generates flow through the rapid rotation of an impeller, imparting momentum to the blood. The rotational flow pattern is susceptible to the formation of vortices and the development of turbulence. Previous research indicates that fluid dynamic conditions have a close relation with thromboembolic complications.[106] The formation of vortices in close proximity to artificial surfaces promotes blood clotting and thrombus deposition.[107] This suggests that the fluid path should be

optimized to avoid exposure of blood elements to long residence times and elevated shear stress. Thus, the aim of this research is to perform an examination of the flow conditions within a VAD under clinically relevant flow conditions. The data resulting from this study may be used to avoid conditions which may increase the probability of thrombus formation in rotary pumps, providing better patient support and improved outcomes.

This chapter analyzes the flow field in an axial blood pump using visualization and numerical simulation, and applied the model developed in chapter 3 to directly predict the thrombus growth. In section 4, based on the mathematical model used in section 3, a dimensionality-reduced model is developed for economizing the computational cost, which is essential for blood pump engineering design and optimization.

4.2 Flow field analysis by numerical simulation and high-speed visualization in axial flow blood pump

The purpose of this study is to examine the flow field under clinically relevant pulsatile conditions by high-speed videography and numerical simulation.

4.2.1 Material and methods

Mathematical model and numerical setup

Different to the problems in purely inertial frame, an axial pump, like Heartmate II, always has one stage, namely rotator or impeller, which should be modeled in rotational frame. In inertial frame, the incompressible Navior-Stokes equations reads,

$$\frac{d\boldsymbol{v}_{f,I}}{dt} = \frac{\partial \boldsymbol{v}_{f,I}}{\partial t} + \mathrm{div}\left(\boldsymbol{v}_{f,I} \otimes \boldsymbol{v}_{f,I}\right) = -\nabla\left(p/\rho_f\right) + \nu \cdot \mathrm{div}\left(\nabla\left(\boldsymbol{v}_{f,I}\right)\right) \tag{4.1}$$

$$\mathrm{div}(\boldsymbol{v}_{f,I}) = 0 \tag{4.2}$$

where $\boldsymbol{v}_{f,I}$ refers to the velocity in inertial frame or absolute velocity, p is the pressure, ρ_f is the density of the fluid and ν is the kinematic viscosity. Consider the relationship between the velocity in inertial and rotational frame is,

$$\boldsymbol{v}_{f,I} = \boldsymbol{v}_{f,R} + \boldsymbol{\omega} \times \boldsymbol{r} \tag{4.3}$$

where $\boldsymbol{v}_{f,R}$ is the velocity in rotating frame or relative velocity, $\boldsymbol{\omega}$ is the angular velocity of the rotating stage and $\boldsymbol{r}$ is the space vector between the considered point and rotating origin. Then the incompressible Navior-Stokes equations in rotational frame with relative velocity reads,

$$\begin{aligned} &\frac{\partial \boldsymbol{v}_{f,R}}{\partial t} + \frac{d\boldsymbol{\omega}}{dt} \times \boldsymbol{r} + \mathrm{div}(\boldsymbol{v}_{f,R} \otimes \boldsymbol{v}_{f,R}) + 2\boldsymbol{\omega} \times \boldsymbol{v}_{f,R} + \boldsymbol{\omega} \times \boldsymbol{\omega} \times \boldsymbol{r} \\ &= -\nabla(p/\rho_f) + \nu \cdot \mathrm{div}\left(\nabla(\boldsymbol{v}_{f,R})\right) \end{aligned} \tag{4.4}$$

$$\mathrm{div}(\boldsymbol{v}_{f,R}) = 0 \tag{4.5}$$

And the incompressible Navior-Stokes equations, which is applied in developing CFD solver, in rotational frame with absolute velocity reads,

$$\frac{\partial \boldsymbol{v}_{f,R}}{\partial t} + \frac{d\boldsymbol{\omega}}{dt} \times \boldsymbol{r} + \mathrm{div}(\boldsymbol{v}_{f,R} \otimes \boldsymbol{v}_I) + \boldsymbol{\omega} \times \boldsymbol{v}_I = -\nabla(p/\rho_f) + \nu \cdot div\left(\nabla(\boldsymbol{v}_{f,I})\right) \tag{4.6}$$

$$\mathrm{div}(\boldsymbol{v}_{f,I}) = 0 \tag{4.7}$$

For steady state flow, in inertial frame,

$$\mathrm{div}(\boldsymbol{v}_{f,I} \otimes \boldsymbol{v}_{f,I}) = -\nabla(p/\rho_f) + \nu \cdot \mathrm{div}\left(\nabla(\boldsymbol{v}_{f,I})\right) \tag{4.8}$$

$$\mathrm{div}(\boldsymbol{v}_{f,I}) = 0 \tag{4.9}$$

in rotational frame,

$$\mathrm{div}(\boldsymbol{v}_{f,R} \otimes \boldsymbol{v}_{f,I}) + \boldsymbol{\omega} \times \boldsymbol{v}_I = -\nabla(p/\rho_f) + \nu \cdot \mathrm{div}\left(\nabla(\boldsymbol{v}_{f,I})\right) \tag{4.10}$$

$$\mathrm{div}(\boldsymbol{v}_{f,I}) = 0 \tag{4.11}$$

The blood analogue was treated as a Newtonian fluid which has the viscosity of 3.5 cP and density of 1.08g/cm^3. The simulation was performed using CFX, ANSYS, Inc., Canonsburg, PA. The geometry and mesh are shown in Figure 4.1. The computational domain was by divided to be three different stages: 1: the straightener vane, 2: impeller and 3: diffuser, see Figure 4.1. Except stage 2 and hub of stage 3 rotating at 9000 rpm, all the other parts including the shroud of the stage 2 are considered in stationary frame. The $k-\omega$ model was applied to account for the turbulence, and the interface coupling between rotational and stationary domains was modeled using the frozen rotor method. At the inlet a fixed velocity profile was applied and outlet pressure boundary condition was set as 0 Pa.

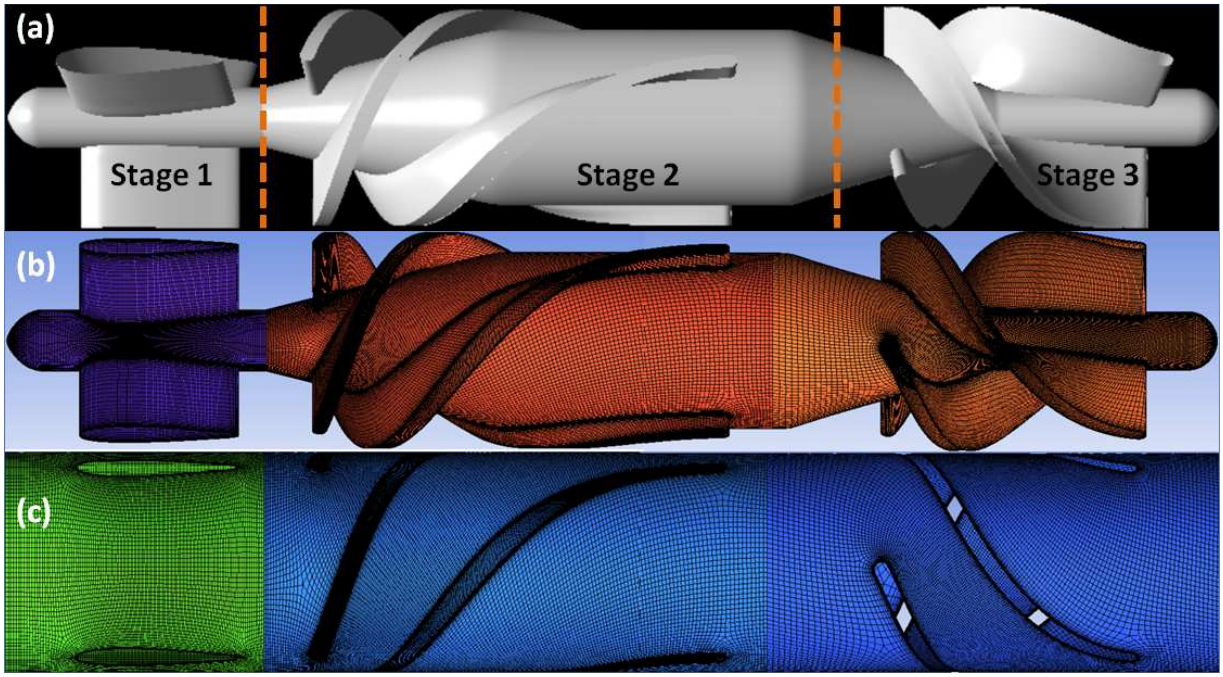

Figure 4.1. (a) Axial pump geometry; (b) Mesh: Hub; (c) Mesh: Shroud. Stage 1: inlet straightener vane; Stage 2: impeller; Stage 3: diffuser.

Experimental setup

As shown in Figure 4.2, a transparent replica of the Heartmate II was made in our lab. The pump fluid path consists of a single axial rotor wrapped with three blades, an inlet flow straightener with three straight blades, an outlet stator wrapped with three straight blades, all within a casing duct. The diameter of the casing duct is 12mm. Figure 4.2 shows the inlet and outlet sections of the axial pump. The hub of the pump rotor is conically shaped at both ends and cylindrical at the middle. The pump rotor is radially and axially supported by two ball-and-cup bearing located at both ends of the rotor hub. The pump rotor is actuated by an integrated motor, and a permanent magnet within the hub cooperates with field coils located outside the flow tube.

Figure 4.3 shows the experimental setup for our pump flow visualization. The pump was placed in a simplified circulatory simulator comprised of reservoir, restrictor valve, in series with a pneumatic pump to simulate the pulsatile contribution of the native heart. Pressure meter (P1 and P2) and flow meter were provided to measure pressure differential and flow through the pump. The region of interest for this study was the upstream pump stage (as circled in Figure 4.2), encompassing the leeward ball-cup bearing region and stay vanes. The region was illuminated with a laser sheet (appx 1mm thick) using a Diode-pumped solid-state laser (532 nm wavelength, DPSSL-1000), created by cylindrical lens (rod, 5 mm diameter, 3.7 mm focal length) in series with a convex lens (5mm focal length). Background glare was eliminated using an optical Longpass filter (550 nm, FGL550s, Thorlabs) providing excellent contrast of the fluorescent particles. Video was acquired using a high speed CMOS camera (Photron Fastcam SA4, Photron USA, Inc). Steady-state flow conditions were studied, defined previously in terms of non-dimensional coefficients as nominal, low flow and high flow.

A transparent blood analog fluid consisting of water/glycerin solution titrated to a viscosity of 3.5 cP and a density of 1.08 g/cm^3 at room temperature (approximately 20 ℃) was used as test

fluid for all of these studies. The resulting concentration of glycerol was approximately 33% by volume. Neutrally buoyant 30 µm fluorescent microspheres (Fluoro-Max Fluorescent Particles, Thermo Scientific) were seeded into the test fluid for visualization. Although this solution is a Newtonian fluid, it is suitable for these studies because of the high shear rates, in which the non-Newtonian properties of blood such as shear thinning and viscoelasticity are negligible.

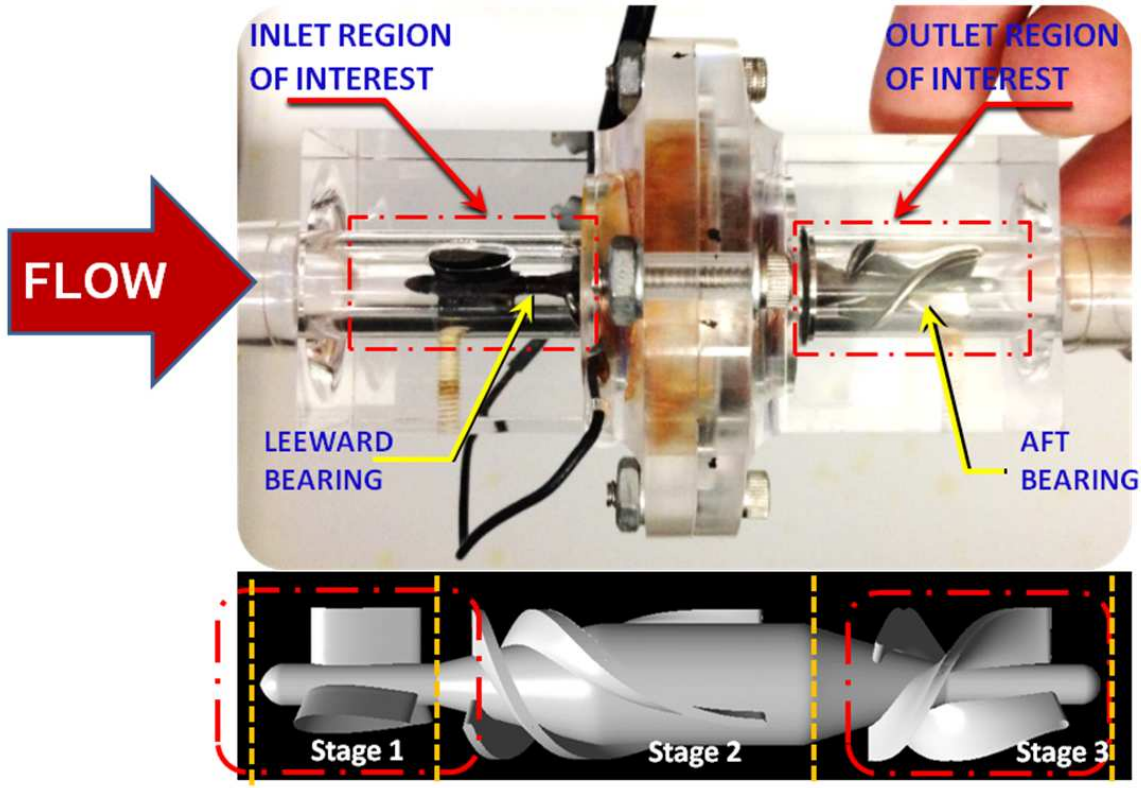

Figure 4.2. Transparent replica of the Heartmate II and schematic of visualization area

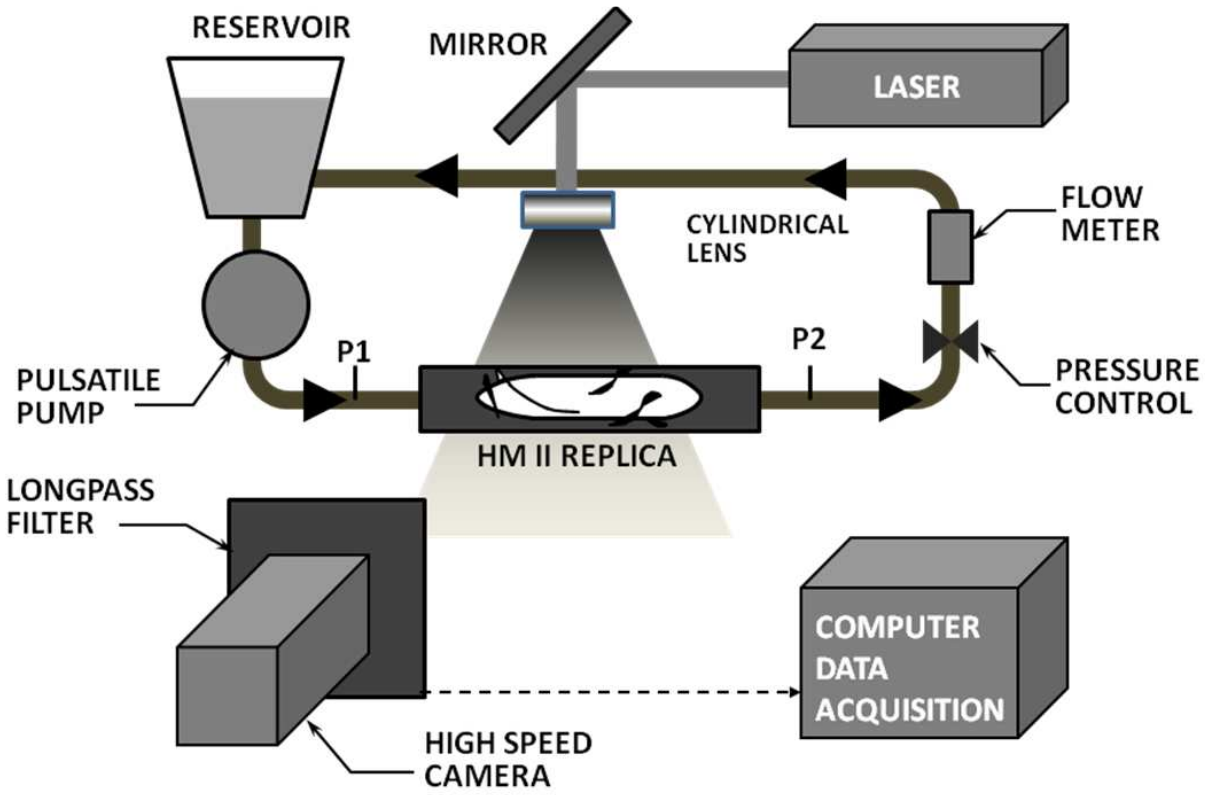

Figure 4.3. Experimental visualization setup

4.2.2 Results

Figure 4.4 shows the streamlines in rotational and stationary frame at the different inflow rate. It can be clearly seen that, with a same impeller rotational speed, at a low flow rate, streamlines tend to be distorted and there exits vortexes. At the low flow rate, in the impeller, the streamline circles for more times than at the high flow rate before leaving the impeller. This implies a greater dwell time for and repeated contact with the biomaterial surface. Figure 4.5 shows the streamlines comparison between numerical simulation and experiments, at different inflow rate. At nominal and high flow rates, the flow fields were found to be generally stable, well attached, and streamlined. As the flow rate was reduced, a rapid transition to disturbed velocity field occurred in which a large toroidal vortex was exhibited upstream of the flow straightener vanes,

and chaotic pathlines were observed in the region of the leeward bearing. It was common to observe particles trapped within recirculation bubbles, and drawn antegrade along the nose cone, causing repeated contact between particle and bearing surface. The addition of pulsatility shifted the transition between stable and disturbed flow to a higher flow rate. In general, the disturbed flow periodically became streamlined during the acceleration phase (dQ/dt >0), and was most chaotic during deceleration. This initial wave of pulsatility served to displace some vortices, washing them downstream. Particles trapped within recirculation bubbles, and drawn antegrade along the nose cone, causing repeated contact between particles and bearing surface.

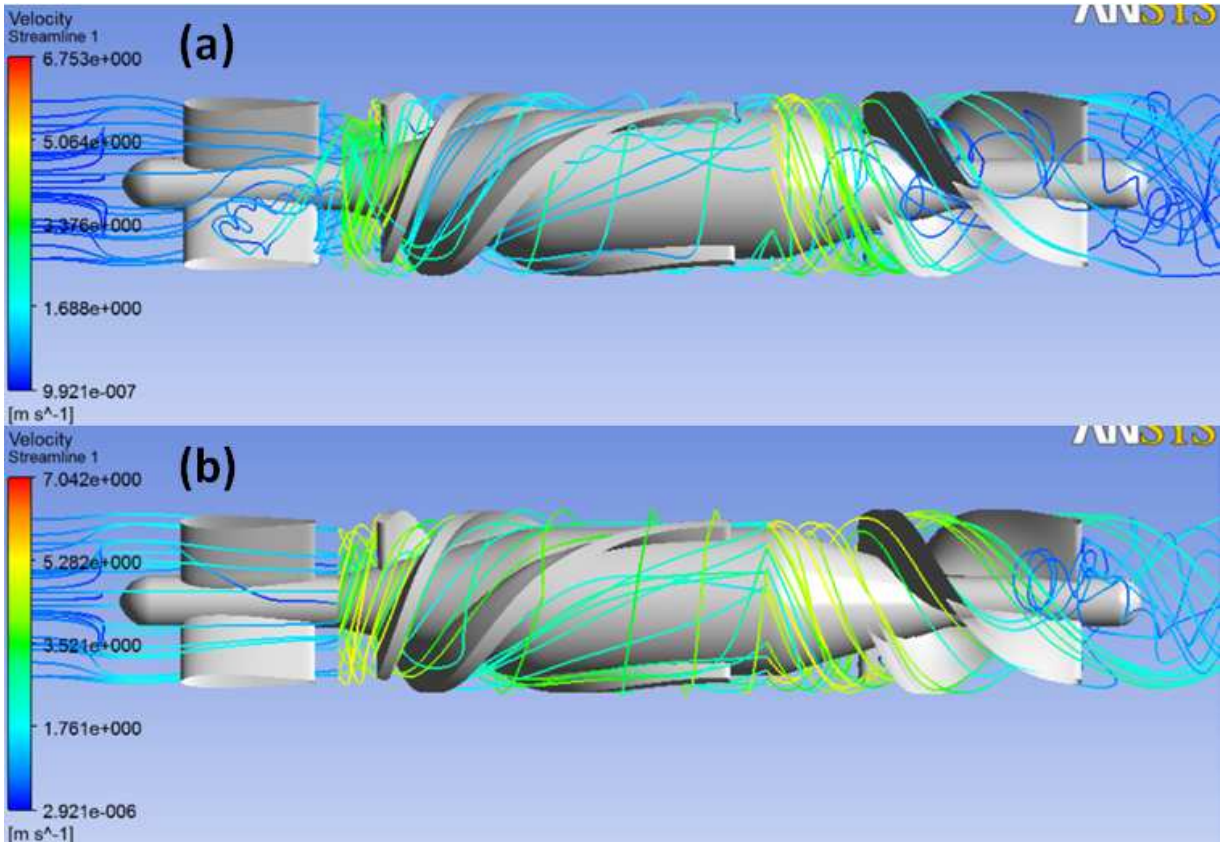

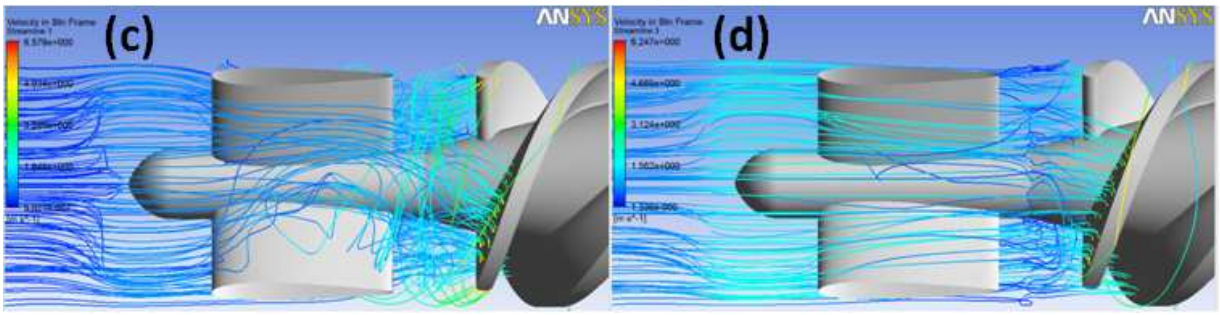

Figure 4.4. Streamlines: (a) Velocity in rotational frame when inflow rate is 2.0L/min and rorotational speed of impeller is 9000RPM; (b) Velocity in rotational frame when inflow rate is 4.5L/min and rorotational speed of impeller is 9000RPM; (c) Velocity in stationary frame when inflow rate is 2.0L/min and rorotational speed of impeller is 9000RPM; (d) Velocity in stationary frame when inflow rate is 4.5L/min and rorotational speed of impeller is 9000RPM.

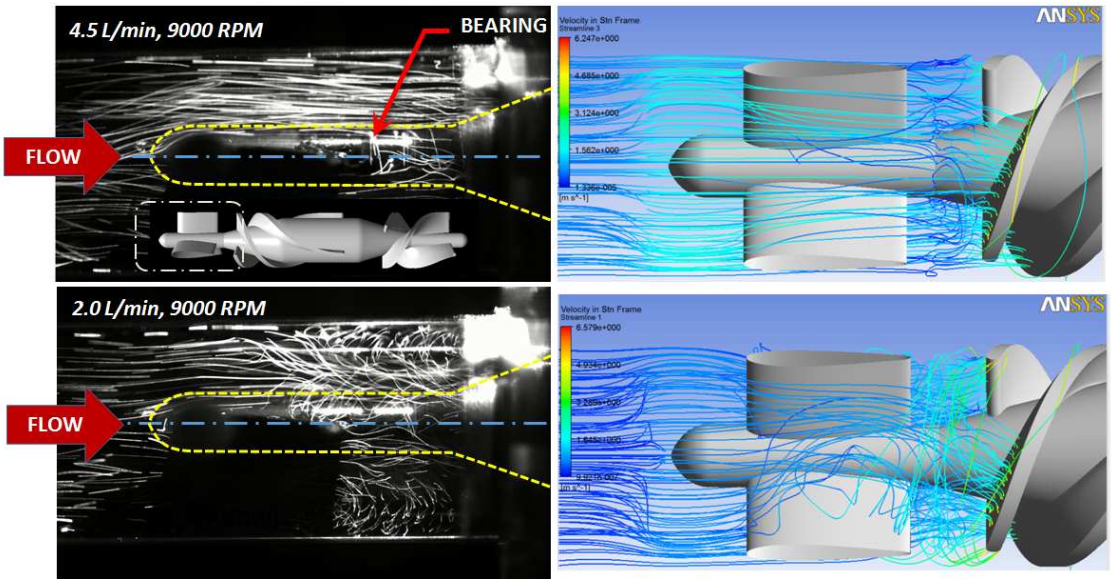

Figure 4.5. Fluorescent particle pathlines reveal and numerical simulation flow field near inlet duct inside the pump

4.2.3 Discussion

In this section, flow patterns were analyzed by numerical simulation and high speed camera in a transparent Heartmate II replica under different operating conditions. Numerical simulations shown reasonable agreement with the experimental observations. Flow condition was studied. Aberrant flow features caused by flow condition were observed. Under low-flow, pathlines

within the HM2 are chaotic and potentially prothrombotic. Through the study, it may can be concluded that a lower flow rate with high RPM may contribute to thrombus growth. In an axial blood pump, thrombus is commonly found at the rear of the inlet straightenor vane and at the beginning part of the impeller.

4.3 Direct prediction of thrombus growth in axial blood pump

Perhaps due to the complex flow field in axial blood pump and complicated biological and chemical procedure of thrombus growth, to our knowledge, no one has successfully directly predicted the thrombus deposition in a blood pump to date. Of course, a successful numerical prediction will be very essential for whole the area of axial blood pump. In this section, we apply the mathematical model developed and validated in chapter 3 to directly predict the procedure of the thrombus growth in HeartMate II.

4.3.1 Mathematical model and numerical setup

Due to the interaction between the blood and thrombus, the Navior-Stokes equation is modified form the last section. In the inertial frame, the incompressible Navior-Stokes equations reads,

$$\frac{d\boldsymbol{v}_{f,I}}{dt} = \frac{\partial \boldsymbol{v}_{f,I}}{\partial t} + \mathrm{div}\left(\boldsymbol{v}_{f,I} \otimes \boldsymbol{v}_{f,I}\right) = -\nabla\left(p/\rho_f\right) + \nu \cdot \mathrm{div}\left(\nabla\left(\boldsymbol{v}_{f,I}\right)\right) - C_2\left(\boldsymbol{v}_{f,I} - \boldsymbol{v}_T\right) \tag{4.12}$$

$$\mathrm{div}\left(\boldsymbol{v}_{f,I}\right) = 0 \tag{4.13}$$

where $\boldsymbol{v}_T$ is the velocity of the thrombus (detail about $\boldsymbol{v}_T$, see last chapter.), and C_2 is the resistance force coefficient. It should be emphasized that the velocity of the thrombus is a variable depending on the rotational properties of the original boundary it developed from. The incompressible Navior-Stokes equations including the interaction with the thrombus, in rotational frame with absolute velocity reads,

$$\frac{\partial \boldsymbol{v}_{f,R}}{\partial t} + \frac{d\boldsymbol{\omega}}{dt} \times \boldsymbol{r} + \mathrm{div}\left(\boldsymbol{v}_{f,R} \otimes \boldsymbol{v}_I\right) + \boldsymbol{\omega} \times \boldsymbol{v}_I = -\nabla\left(p/\rho_f\right) + \nu \cdot div\left(\nabla\left(\boldsymbol{v}_{f,I}\right)\right) - C_2\left(\boldsymbol{v}_{f,I} - \boldsymbol{v}_T\right) \tag{4.14}$$

$$\mathrm{div}\left(\boldsymbol{v}_{f,I}\right) = 0 \tag{4.15}$$

It should be emphasized that in the rotational frame, the velocity applied in the transport equations are relative velocity $\boldsymbol{v}_{f,R}$. The blood properties are set as same to the last section. Based on the equations above and also the thrombus model introduced in section 4, A CFD solver is developed using the solvers and the libraries of OpenFOAM®. Considering the high computational cost of current problem, for accelerating the thrombus formation, the deposition reaction related parameters are scaled: $k_{ra} = 2.0 \times 10^{-5}\mathrm{m/s}$, $k_{aa} = 1.0 \times 10^{-3}\mathrm{m/s}$, $k_{emb} = 3.0 \times 10^{-7}\mathrm{m/s}$, $k_{rpdb} = 1.0 \times 10^{-10}\mathrm{m/s}$, $k_{apdb} = 1.0 \times 10^{-4}\mathrm{m/s}$ and $k_{embb} = 6.0 \times 10^{-6}\mathrm{m/s}$; The inlet [RP] and [AP] is 3×10^{14} and 3×10^{12}. All the other parameters related to the thrombus model is summarized in Chapter 3.

4.3.2 Results

Procedure of the thrombus growth

Figure 3.4 shows an overview of the simulated thrombus distribution in the axial blood pump, HeartMateII, after 300s. The flow rate is 4.5L/min and the rotational speed is 9000 RPM. This simulation took about 2*24 hours, using 40 CPUs(2.4G). From the figure, we can see that the regions where thrombus accumulated most are the blades of the inlet straightener vane, the rear of the straightener and inlet part of the impeller, see Figure 4.1. These parts are the regions in which thrombus is most reported clinically (See Figure 4.7 [34, 108]). Comparing Figure 3.4 and Figure 4.7, it can be found that simulation also predicted region absent of thrombus, such as the leading edge of the blades of the inlet straightener vane. The Figure 4.8 shows thrombus

deposition in pump stage 1, namely the inlet straightener vane, after simulating for 2000s. We can see that along the downstream direction, at the rear of the thick thrombus, a sudden expansion like geometry comes out, see the dashed box. Similar to a crevice, thrombus can easily grow in such geometry as well. Furthermore from Figure 4.8 we can also infer that the thrombus will keep growing and potentially blocking the passageway of the pump, increasing the pressure, leading to hemolysis. Finally the thrombus will cause the malfunction of the blood pump, which implies a replacement surgery for patients.

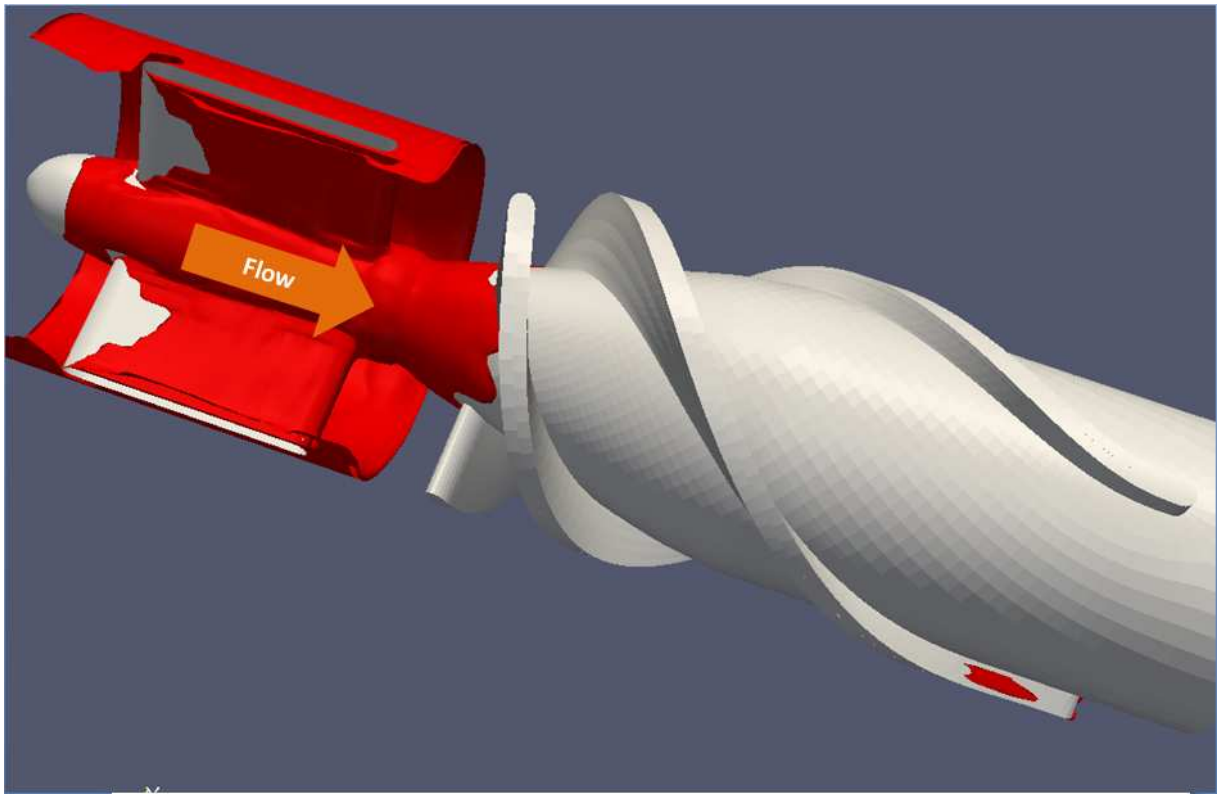

Figure 4.6 Thrombus deposition in axial blood pump after simulating for 300s. The inlet flow rate is 4.5L/min, and the rotational speed of impeller is 9000RPM. Stage 1 and stage 2 are simulated.

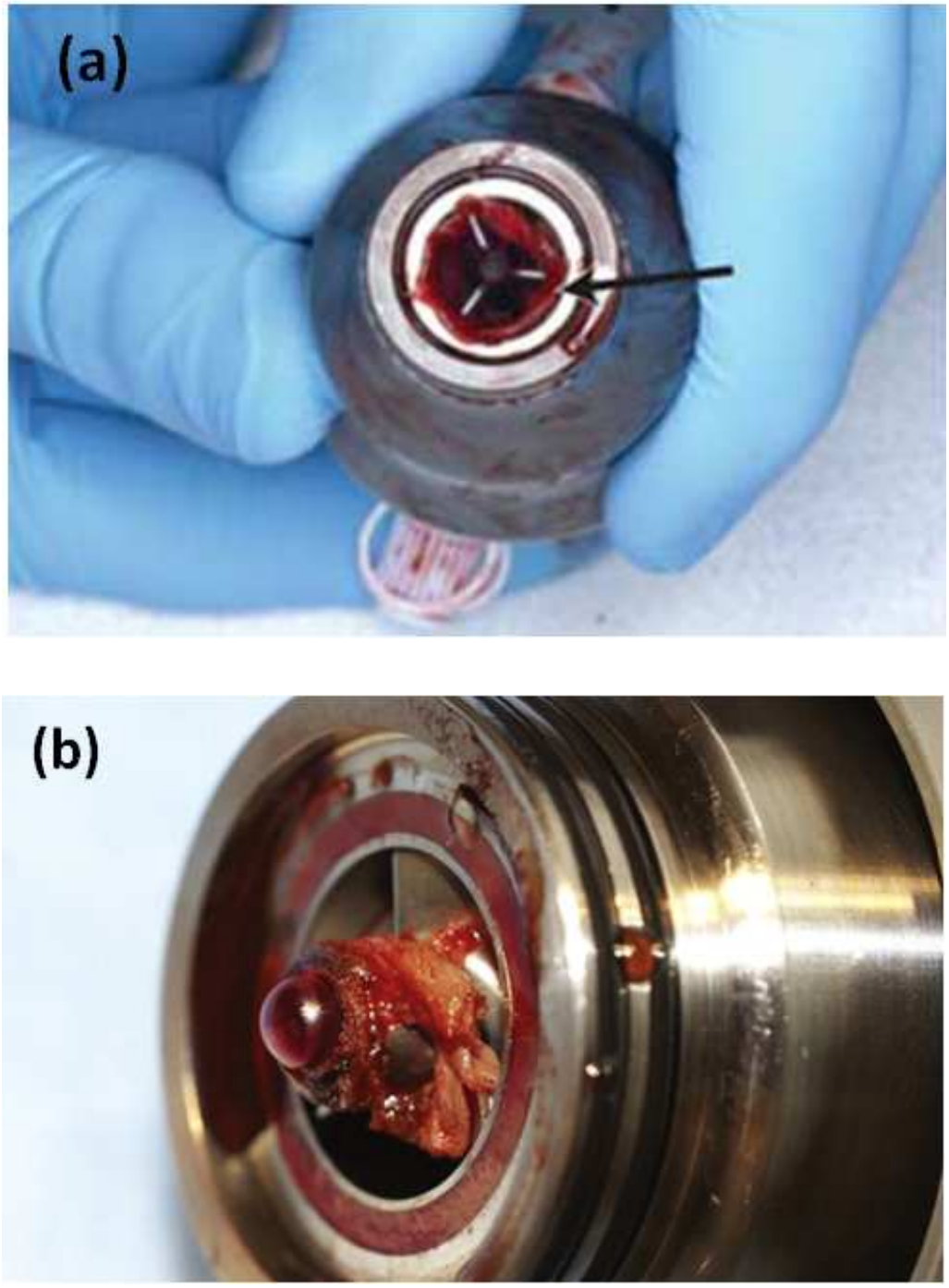

Figure 4.7 Clinical observation of thrombus deposition in axial blood pump. (a) Inlet of straightener vane; (b) Inlet of impeller. [34]

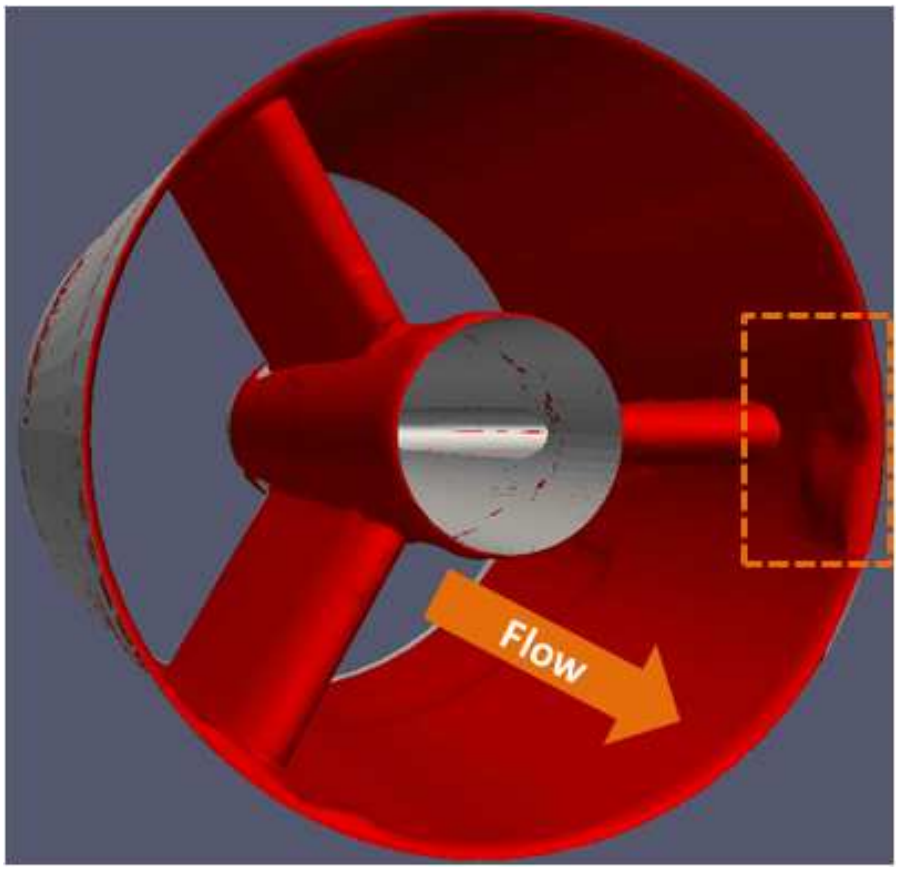

Figure 4.8 Thrombus deposition in axial blood pump after simulating for 2000s. The inlet flow rate is 4.5L/min, and the rotational speed of impeller is 9000RPM. Only stage 1 is simulated.

Figure 4.9 shows the evolution of the thrombus growth, which indicates the thrombus starting at the rear of the inlet straightener vane. This coincides to the region of lowest shear rate, see Figure 4.10. These early deposited thrombus provides base for incoming platelets, similar to the case of the thrombus deposition in blood vessel studied in chapter 3; concomitantly the agonists produced by deposited platelets activate the surround platelets. In the other words, the early thrombus provides the advantages for thrombus propagation, which of course is the disadvantages for blood pumps and patients.

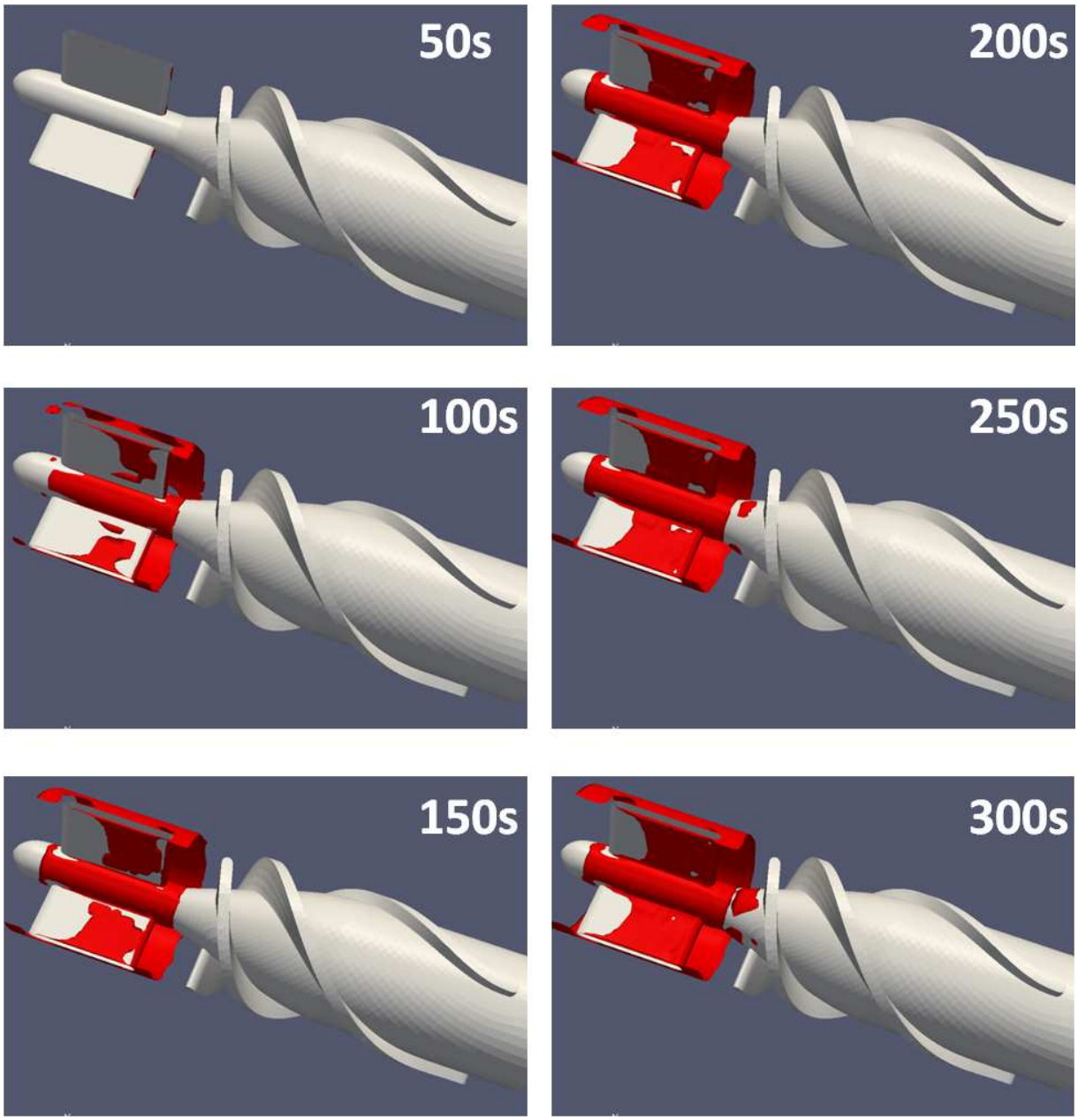

Figure 4.9 Thrombus deposition procedure in axial blood pump: the straightener vane and the impeller. The inlet flow rate is 4.5L/min. The rotational speed of impeller is 9000RPM.

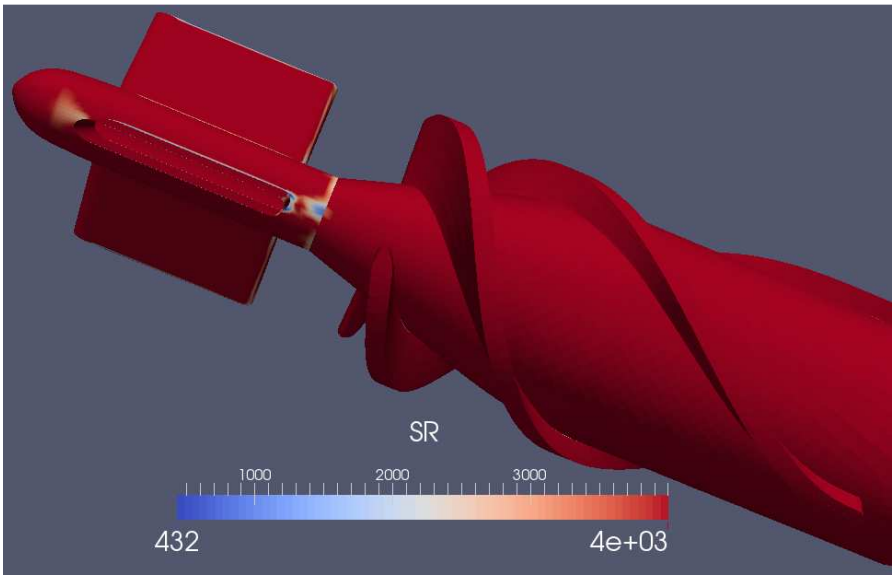

Figure 4.10 Wall shear rate field in pump. The inlet flow rate is 4.5L/min. The rotational speed of impeller is 9000RPM.

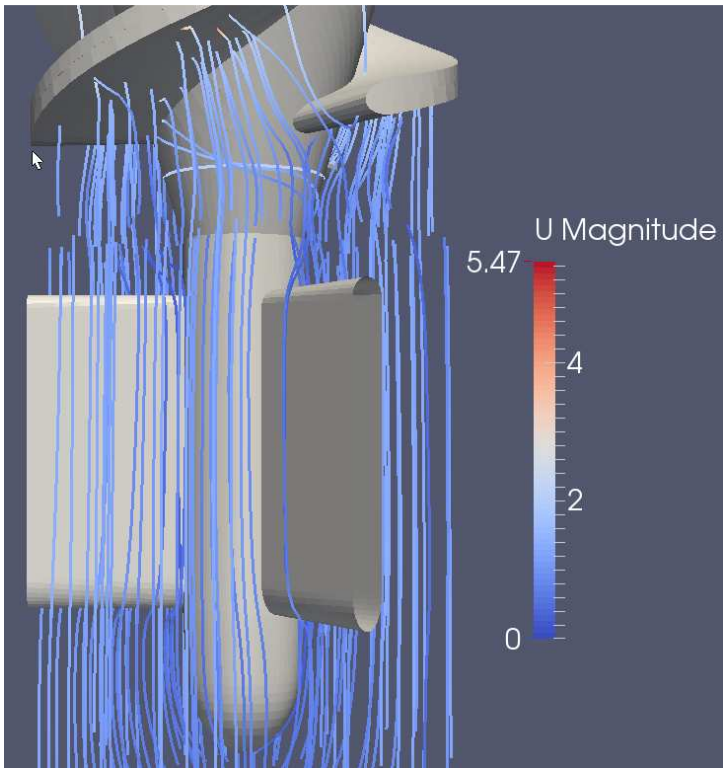

Figure 4.11 Streamlines near inlet duct inside pump. The inlet flow rate is 4.5L/min. The rotational speed of impeller is 9000RPM.

Effect of the flow rate

Figure 4.12 shows an overview of the thrombus distribution after simulating for 300s for two different inflow rates. It can be seen that at low flow rate, the amount of the accumulated thrombus is much larger than at high inflow rate, which agrees with the observation and conjecture we made in section 2. At the low inflow rate, at the rear of the inlet straightener vane and the inlet part of the impeller, a lot of vortexes develop and platelets, following the streamlines, repeatedly contact with the bearing surface (See Figure 4.16). Such repeated contact makes platelets have larger possibility to be activated and adhere with the bearing surface or deposited thrombus. Figure 4.13 shows the thrombus growth procedure at low inflow rates(2.0L/min). Similar to the high flow rate, in the low flow rate thrombus still starts at rear of the inlet straightener vane, however thrombus accumulated faster with the low flow rate.

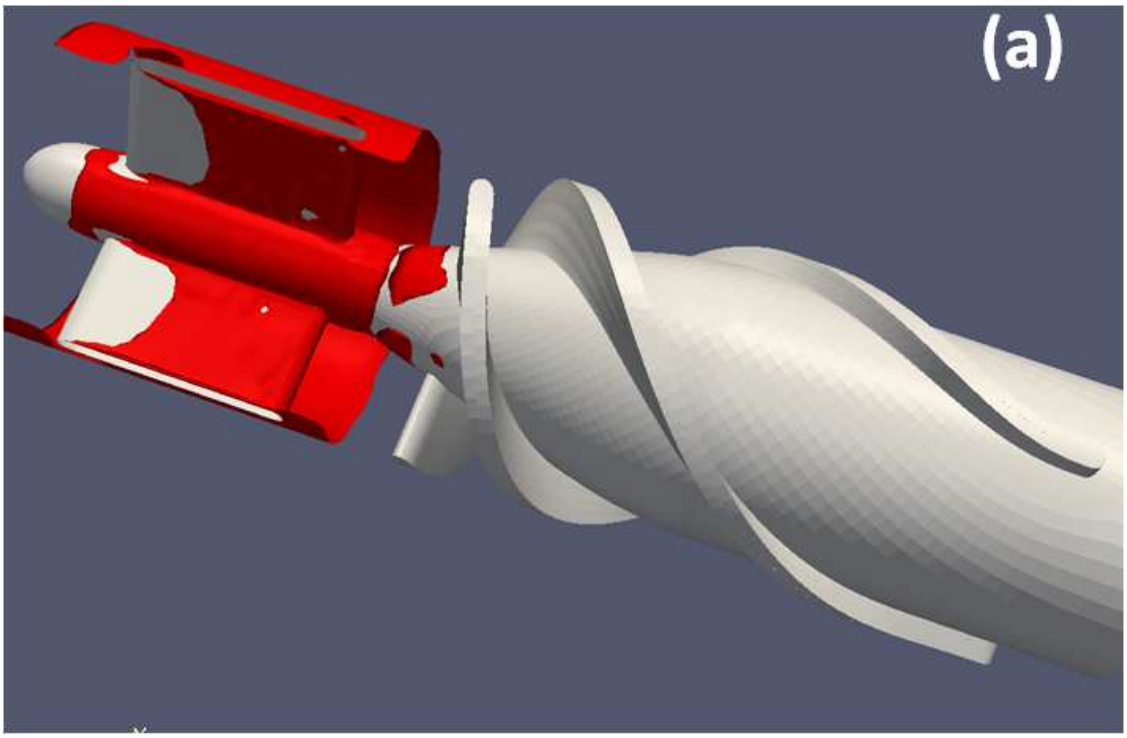

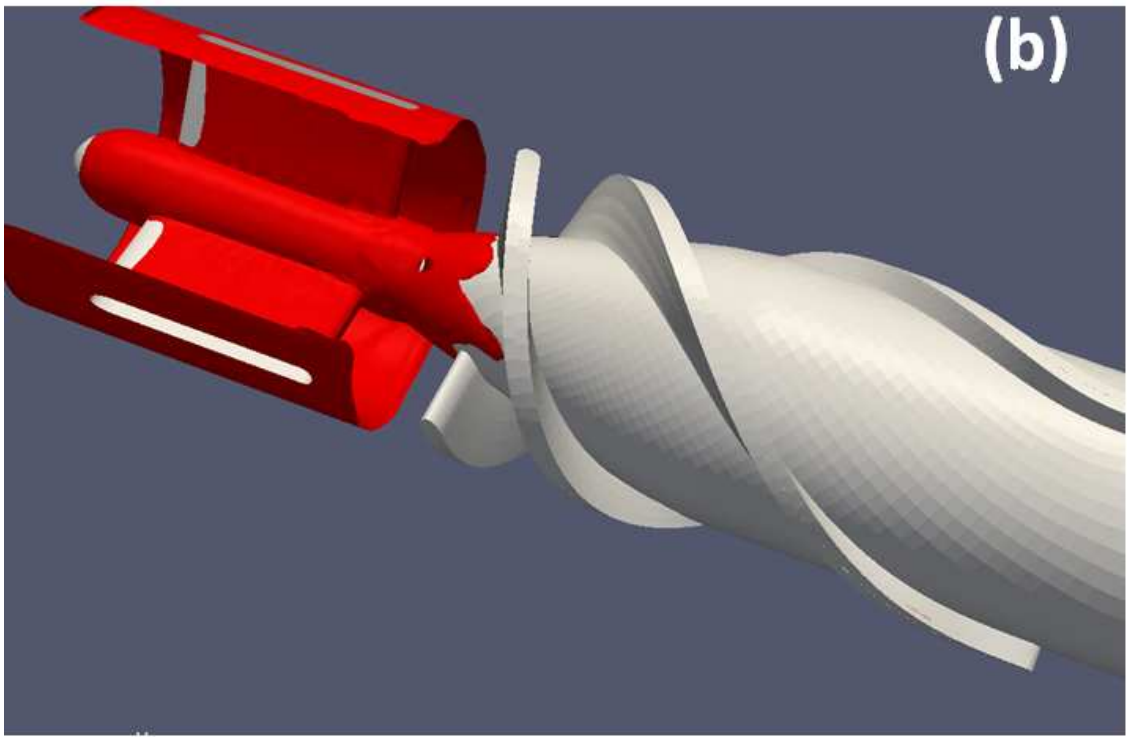

Figure 4.12 Thrombus deposition after simulating for 300s under two inflow rates: (a) 4.5L/min; (b) 2.0L/min. The rotational speed of impeller is 9000RPM.

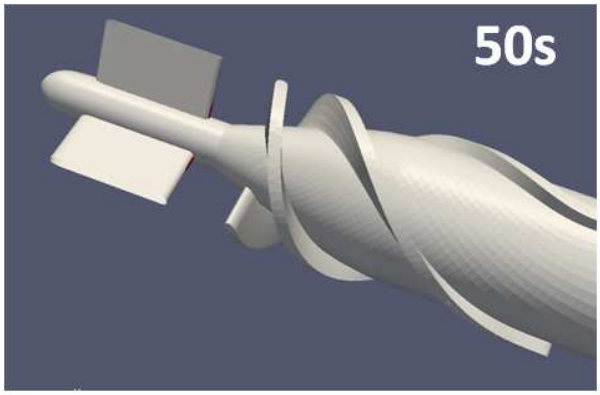

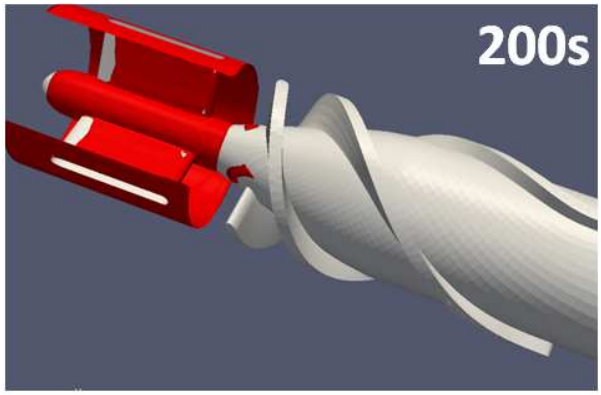

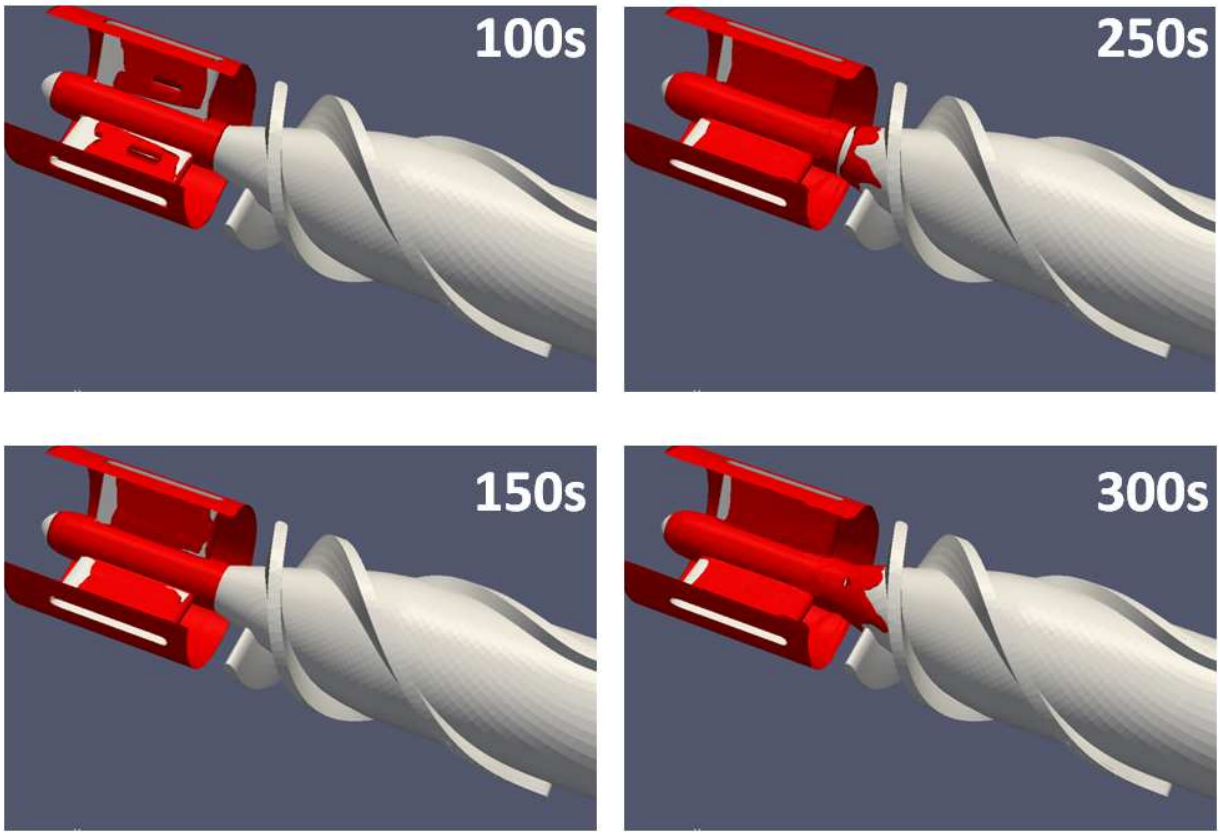

Figure 4.13 Thrombus deposition procedure in axial blood pump: the straightener vane and the impeller. The inlet flow rate is 2.0L/min. The rotational speed of impeller is 9000RPM.

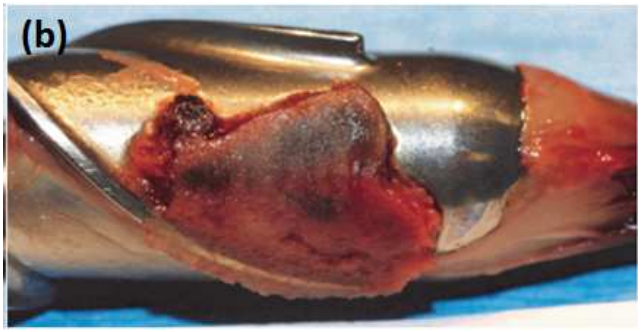

Figure 4.14 Clinical observation of thrombus deposition in impeller of axial blood pump.

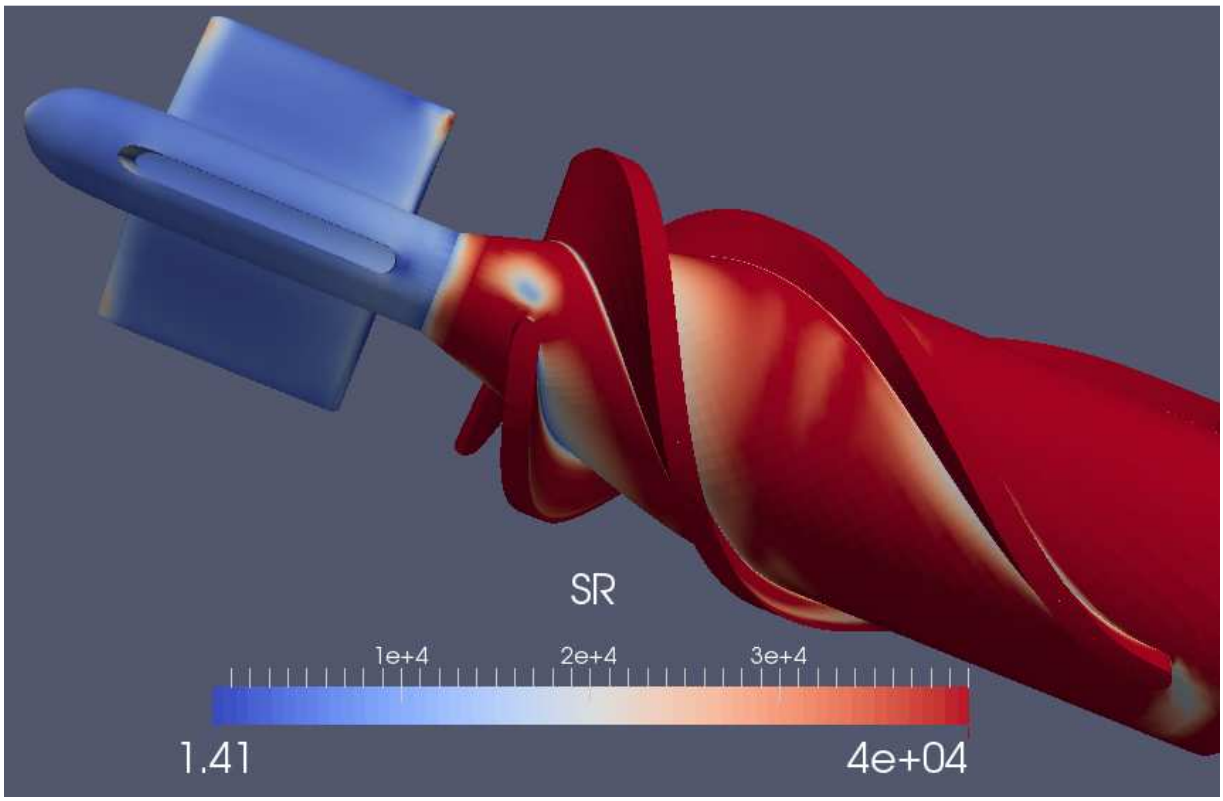

Figure 4.15 Wall shear rate field in pump. The inlet flow rate is 2.0L/min. The rotational speed of impeller is 9000RPM.

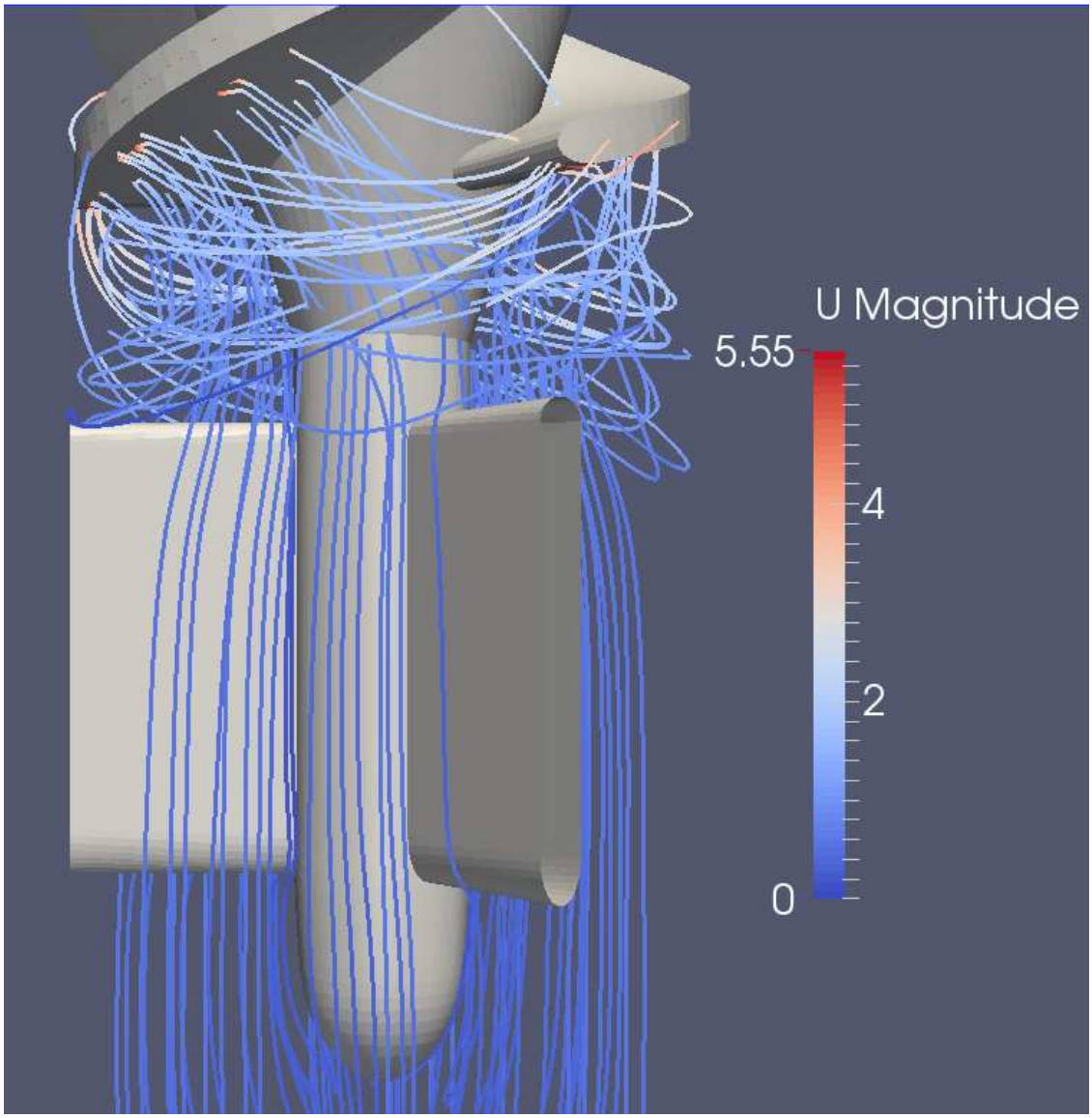

Figure 4.16 Streamlines near inlet duct inside pump. The inlet flow rate is 2.0L/min. The rotational speed of impeller is 9000RPM.

4.3.3 Discussion

In this section, we successfully predicted the thrombus growth in blood pump applying the mathematical model developed in chapter 3. The simulation results agree with the clinical observation very well: The simulations shown that thrombus mostly prefer accumulating at the straightener vane blades, rear of the straightener vane and the inlet part of the impeller; The

simulations also shown that with a same RPM, thrombus accumulates faster at a lower inflow rate. It should be emphasized that, in this section, it can be found that thrombus prefer to accumulated in the region where the shear rate is relatively low. We should also notice that shear rate plays complicated role during the procedure of the thrombus growth: 1. Platelets shear activation; 2 Deposited platelets shear embolization. We may infer that at a low shear rate, the effect of the shear activation is more obvious but the effect of the shear embolization is small and even negligible. At some high shear rate, the thrombus deposition is mainly controlled by the shear embolization. In other words, if shear rate is higher than some value, no newly deposited platelets will be stabilized and stay.

4.4 Direct prediction of thrombus growth in axial blood pump using a dimensionality-reduced model

In last section, we have performed a successful direct prediction on the thrombus growth in blood pump. The model used in the last section is computationally expensive(one case takes about 2 days and is far away from steady-state.) which is a disadvantage for engineering applications. Therefore, in this section, we present a dimensionality-reduced model. Similar to the idea of the Sorenson's model, we constrain that the thrombus is only able to developed in "boundaries" but not able to intrude into the flow field, which means we do not need to update the flow field, namely solving the Navior-Stokes equations, while the thrombus grows. It also can be expected that without blood-thrombus interaction, we may can use a larger time step to achieve the steady-state condition.

4.4.1 Mathematical model and numerical setup

Blood (RBCs and plasma)

In the dimensionality-reduced thrombus model, the thrombus will not intrude into the flow field. Therefore, the Navior-Stokes equations are same to those in section 2. In inertial frame,

$$\frac{d\boldsymbol{v}_{f,I}}{dt} = \frac{\partial \boldsymbol{v}_{f,I}}{\partial t} + \text{div}\left(\boldsymbol{v}_{f,I} \otimes \boldsymbol{v}_{f,I}\right) = -\nabla\left(p/\rho_f\right) + \nu \cdot \text{div}\left(\nabla\left(\boldsymbol{v}_{f,I}\right)\right) \tag{4.16}$$

$$\text{div}\left(\boldsymbol{v}_{f,I}\right) = 0 \tag{4.17}$$

In rotational frame,

$$\frac{\partial \boldsymbol{v}_{f,R}}{\partial t} + \frac{d\boldsymbol{\omega}}{dt} \times \boldsymbol{r} + \text{div}\left(\boldsymbol{v}_{f,R} \otimes \boldsymbol{v}_I\right) + \boldsymbol{\omega} \times \boldsymbol{v}_I = -\nabla\left(p/\rho_f\right) + \nu \cdot div\left(\nabla\left(\boldsymbol{v}_{f,I}\right)\right) \tag{4.18}$$

$$\text{div}\left(\boldsymbol{v}_{f,I}\right) = 0 \tag{4.19}$$

The blood properties are the same as the last section.

Thrombus: Chemical and biological species

Similar to the model introduced in chapter 3, in this dimensionality-reduced model, all the chemical and biological species are also described by convection-diffusion-reaction equations [1, 2]. In inertial frame,

$$\frac{\partial [C_i]}{\partial t} + div\left(\boldsymbol{v}_{f,I} \cdot [C_i]\right) = div(D_i \cdot \nabla [C_i]) + S_i \tag{4.20}$$

In rotational frame,

$$\frac{\partial [C_i]}{\partial t} + div\left(\boldsymbol{v}_{f,R} \cdot [C_i]\right) = div(D_i \cdot \nabla [C_i]) + S_i \tag{4.21}$$

D_i refers to the diffusivity of species i in blood; $[C_i]$ is the concentration of species i; and S_i is a reaction source term for species i. Table 4.1 lists the appropriate form for the source terms S_i, along with the abbreviation and units used for $[C_i]$, for each species included in the model. Similar to the model in chapter 3, the governing equations for deposited unactivated/activated

platelets and stabilized deposited activated platelets, which do not have convection and diffusion terms, are

$$\frac{\partial [C_i]}{\partial t} = S_i \tag{4.22}$$

The source terms, the abbreviation and units used for these two spices are listed in Table 4.2. The expressions and description of the species boundary conditions are listed in Table 4.3. For more detail about the values/expressions and descriptions of the terms appearing in the model, see chapter 3.

Table 4.1. Model species and reaction source terms.

Species	$[C_i]$ abbreviation	S_i form
Unactivated Resting PLT	[RP]	$-k_{apa}[RP] - k_{spa}[RP]$
Activated PLT	[AP]	$k_{apa}[RP] + k_{spa}[RP]$
PLT-released agonists (ADP)	$[\mathrm{a_{pr}}]$	$\lambda_j\left(k_{apa}[RP] + k_{spa}[RP]\right) - k_{1,j}[\mathrm{a_{pr}}]$
PLT-synthesized agonists (TxA_2)	$[\mathrm{a_{ps}}]$	$s_{pj}[AP] - k_{1,j} \cdot [\mathrm{a_{ps}}]$
Prothrombus	[PT]	$-\varepsilon[\mathrm{PT}](\phi_{at}[AP] + \phi_{rt}[RP])$
Thrombus	[T]	$-\Gamma \cdot [T] + [\mathrm{PT}](\phi_{at}[AP] + \phi_{rt}[RP])$
ATIII	[AT]	$-\Gamma \cdot \varepsilon[T]$

Table 4.2. Model species and reaction source terms.

Species	$[C_i]$ abbreviation	S_i form
Deposited Resting PLT	$[\mathrm{RP_d}]$	N/A
Deposited Activated PLT	$[\mathrm{AP_d}]$	N/A

Deposited and stabilized PLT	$[AP_s]$	N/A

Table 4.3 (a). Species boundary conditions.

Species $[C_i]$	j_i form	Description
[RP]	$-\left(Sk_{rpdb} + \frac{[AP_{db}]}{PLT_{s,max}} k_{ra}\right)[RP] + f_{embb}[RP_d]$	Consumption due to [RP]-Surface and $[RP] - [AP_{db}]$ adhension; Generation due to shear embolization.
[AP]	$-\left(Sk_{apdb} + \frac{[AP_{db}]}{PLT_{s,max}} k_{aa}\right)[AP] + f_{embb}[AP_d]$	Consumption due to [AP]-Surface and $[AP] - [AP_{db}]$ adhesion; Generation due to shear embolization.
$[a_{pr}]$	$\lambda_j\left(k_{apa}[RP_d] + k_{spa}[RP_d] + \theta\left(Sk_{rpdb} + \frac{[AP_{db}]}{PLT_{s,max}} k_{ra}\right)[RP]\right)$	Generation due to agonists and shear activation of $[RP_d]$; Generation due to surface contact activation of [RP]-Surface adhesion.
$[a_{ps}]$	$s_{pj}[AP_d]$	Platelet-synthesized generation due to $[AP_d]$
[PT]	$-\varepsilon[\mathrm{PT}](\phi_{at}[AP_d] + \phi_{rt}[RP_d])$	Consumption due to thrombus, [T], generation.
[T]	$[\mathrm{PT}](\phi_{at}[AP_d] + \phi_{rt}[RP_d])$	Generation from prothrombus [PT] due to deposited platelets.
[AT]	0.0	No reaction flux

Table 4.3 (b). Species boundary conditions.

$[RP_d]$	$\int_0^t (1-\theta)\left(Sk_{rpdb} + \min\left(1.0, \frac{[AP_{db}]}{PLT_{s,max}}\right)k_{ra}\right)[RP] - k_{apa}[RP_d] - k_{spa}[RP_d] - f_{embb}[RP_d]dt$	Generation due to [RP]-Surface and $[RP]-[AP_{db}]$ adhesion; Consumption due to agonists and shear activation; Consumption due to shear embolization.
$[AP_d]$	$\int_0^t \left(Sk_{apdb} + \min\left(1.0, \frac{[AP_{db}]}{PLT_{s,max}}\right)k_{aa}\right)[AP] + \theta\left(Sk_{rpdb} + \min\left(1.0, \frac{[AP_{db}]}{PLT_{s,max}}\right)k_{ra}\right)[RP] + k_{apa}[RP_d] + k_{spa}[RP_d] - \left(f_{embb} + f_{stb}\right)[AP_d]\,dt$	Generation due to [AP]-Surface and $[AP]-[AP_{db}]$ adhesion; Generation due to surface contact activation of [RP]-Surface adhesion; Generation due to agonists and shear activation of [RP]; Consumption due to shear embolization and stabilization.
$[AP_s]$	$\int_0^t f_{stb}[AP_d]\,dt$	Generation due to stabilization.

4.4.2 Results and Discussion

All the parameters related to the thrombus model is summarized in Chapter 3 and last section. The geometry, meshes and all the numerical settings are same to the last two sections. The simulations are considered as steady-state and stopped, when the relative change of $[AP_d]$ are less then $1 \times 10^{-3} s^{-1}$.

Using the same number of the CPUs to the simulations in section 3, the steady-state solutions are achieved by simulating for 3 hours, which is 16 times faster than using complete model. Figure 4.17 and Figure 4.18 shows the thrombus distribution by complete and dimensionality-reduced model at 4.5LPM inflow rate. We can see that the thrombus distributions agree with each other well: the high thrombus concentration regions coincide. This means the dimensionality-reduced model is able to catch the thrombus deposition, and it can therefore be a potential tool for designing or optimizing a blood pump with less thrombus deposition. Of course, from the figures, it also can be found that the total accumulated thrombus predicted dimensionality-reduced model is different to the results by complete model. This is expected due to the difference between two models.

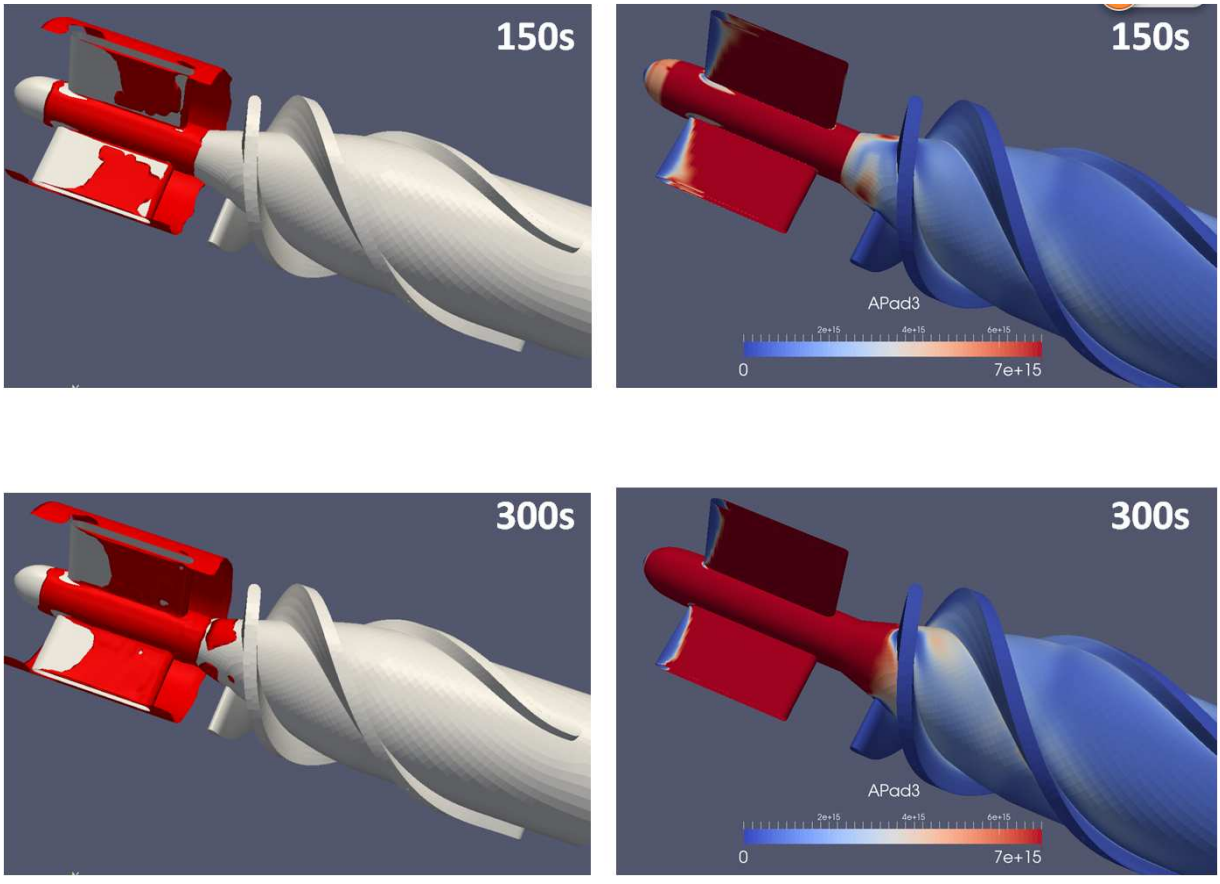

Figure 4.17 Numerical simulation of thrombus deposition in axial blood pump: (a) Complete model; (b) Dimensionality-reduced model. The flow rate is 4.5L/min. The rotational speed of impeller is 9000RPM.

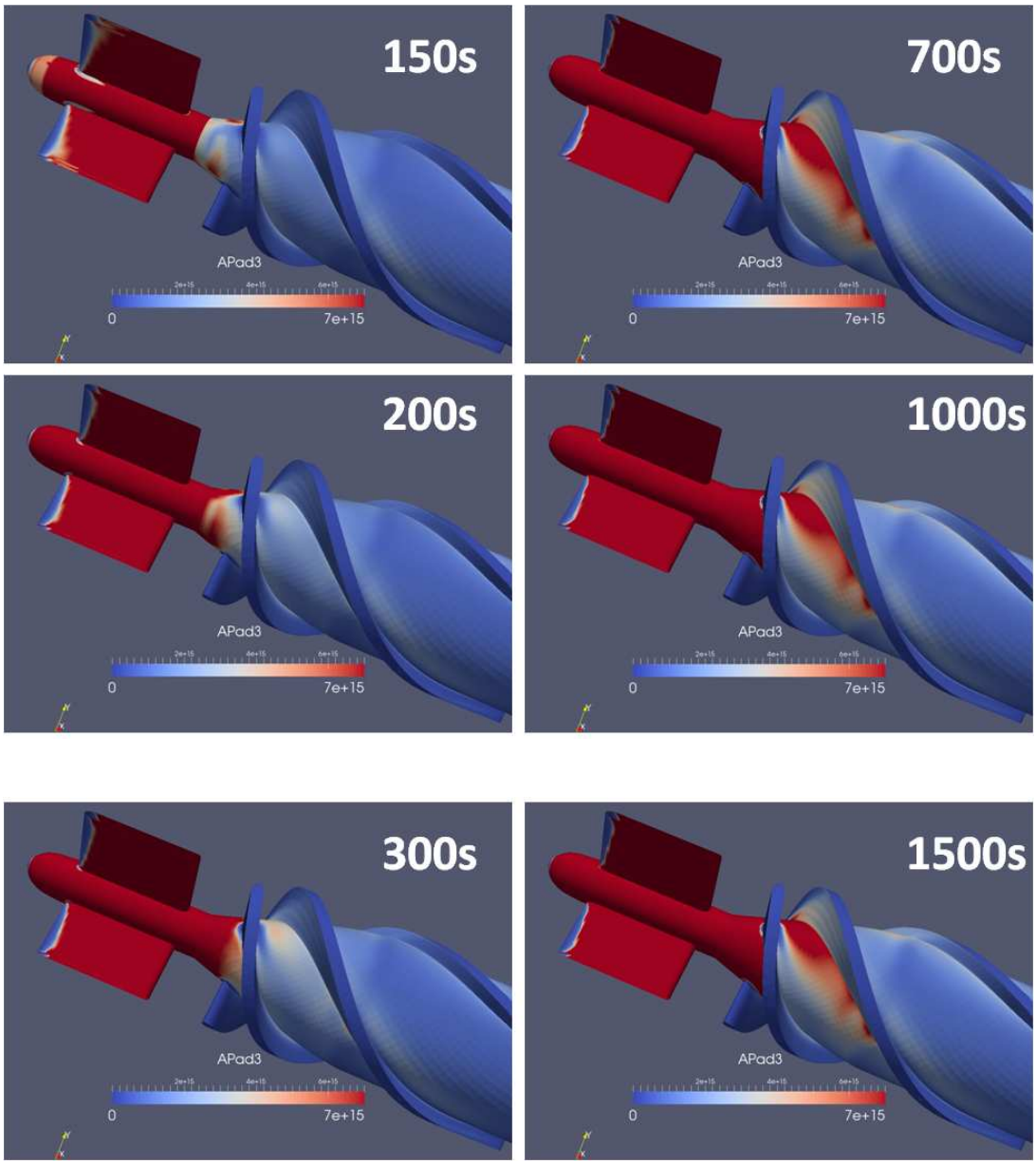

Figure 4.18 Thrombus deposition procedure in axial blood pump using dimensionality-reduced model. The flow rate is 4.5L/min. The rotational speed of impeller is 9000RPM.

4.5 Summary

In this chapter, we studied the thrombus growth in an axial blood pump. In section two, before applying the model developed in chapter 3 to directly predict the thrombus growth, we did flow field analysis in the blood pump using visualization and numerical simulation firstly. Through analysis, we found that at the rear of inlet straightener vane and inlet part of impeller, streamlines are distorted and vortexes tend to come out, which implies thrombus may tend to deposit there. In section 3, applying the mathematical model in chapter 3, we successfully predicted the thrombus growth in blood pump. The simulation results agree with the clinical observation very well. Due to the expensive computational expense of the model applied in section 3, in section 4 a dimensionality-reduced model was employed where agreed well with the complete model.

Chapter 5 Study of blood flow using a two-fluid approach

5.1 Introduction

Blood-related diseases, including cardiovascular, cerebrovascular diseases and malaria, are the leading causes of death in the world [109]. For increasing the survival rates of the patients and also improving their life quality, numerous medical devices and therapies have been developed. Their safety and efficacy is intimately related to the properties and behavior of flowing blood. Comparing with the costly experimental trial-and-error, especially at the initial phase of a project, numerical simulations have been emphasized for their high efficiency and low costs in the design of medical devices [63].

Whole blood is a suspension of red blood cells (RBCs), white blood cells (WBCs) and platelets, in plasma. The volume fraction (hematocrit) of RBCs is about 45%, therefore the properties of whole blood is greatly influenced by their rheological behavior. The most prominent properties are their aggregation and disaggregation as a function of shear rate, their deformability, and their alignment responding to extensional flow. (For additional detail, the reader is directed to [49, 66, 110-112]). These properties are manifested on a bulk scale as shear-thinning and stress relaxation [113]. At the micro-scale, for example in a vessel whose diameter in the range of 20 to 500 microns (and shear rates below 100 s^{-1}), these non-Newtonian phenomena blood are responsible for the trafficking of RBCs (hence their distribution of volume fraction) [114-116].

The multi-component features of blood are considered to be important for many blood related phenomena, such as thrombus and atherogenesis. Thrombus deposition is closely related to the distribution of the platelets, which in turn is influenced by the distribution of RBCs, hence the

collisions between the RBCs and platelets [17, 35-37, 39]. In addition, in the past several decades many important multi-component phenomena have been revealed through the various investigations on blood flow in micro-scale channels. Blood flowing in small tubes exhibits a thin layer of pure plasma, which is called the depletion layer of RBCs [51], and as a result, plasma-skimming occurs in the branch vessel downstream of the depletion layer [54]. Because of the depletion of RBCs, this phenomenon may impair transport of oxygen in distal capillaries [51]. The Fahraeus effect occurs when blood flows into a narrow and long vessel from a larger vessel (for vessel diameters ranging from 0.05 to 1.5 mm.) The hematocrit in the narrow tube reduces compared with that of the larger feeding tube [117, 118]. The Fahraeus–Lindqvist effect is a result of Fahraeus effect, which corresponds to a decrease of the viscosity in the narrow tube compared with that of the feeding (larger) tube [117]. In summary, it is evident that blood flow at micro-scales acts as a multi-component material, and exhibits more complex behavior than can be described by a single phase model.

In the past several decades, various multiphase models for blood have been developed. Mesoscale simulations, such as the *Immersed Boundary Method* (IBM) combined with the *Lattice Boltzmann Method* (LBM), are useful methods for investigating the complex behavior of blood or RBCs in micro-scale flow, particularly due to the deformation, aggregation of the RBCs, see [56, 57, 69]. In these studies, the RBC cytoskeleton and membrane are modeled as a network of springs in combination with bending rigidity and constraints for surface-area and volume conservation. The fluid forces experienced by RBCs are then calculated by integrating the pressure and shear stresses along the RBCs surface [119]. Although these mesoscale simulations have been useful in displaying non-Newtonian behavior of blood, they are still prohibitive for industrial and engineering scale simulations due to the high computational cost [64]. An

alternative method, the two-fluid approach two phase model overcomes the limitation of high computational cost but still provides useful information, such as the volume fraction distribution of the RBCs [58, 120]. For the two-phase formulation, two methods have been widely used: the *Averaging Method* [60, 65, 121] and *Mixture Theory* (or the Theory of Interacting Continua) which is applied in current chapter [59, 122, 123]. The mixture theory is a homogenization approach within the framework of continuum mechanics, first presented by Truesdell[124], in which the phenomena of diffusion, dissociation, combination, and chemical reaction in the broadest sense can be represented [125]. For the basics of the theory, the historical development and applications, the reader is directed to review articles by Atkin and Craine [44, 126, 127], Bowen [128], Bedford and Drumheller [129], Massoudi [130, 131] and the books by Truesdell [125] and Rajagopal and Tao [59, 123].

A two-fluid model for blood, based on mixture theory, was previously introduced Massoudi and Antaki [132], and further detailed in Massoudi et al., [61], and Wu et al.,[66, 133]. The model treats plasma as a Newtonian fluid while the RBCs are treated as a shear-thinning fluid whose viscosity depends on the volume fraction according to experimental observations of Brooks [134]. For studying this two-component system, a three dimensional CFD solver is implemented based on the solvers and libraries in the OpenFOAM®.

5.2 Methods

5.2.1 Governing equations

In the absence of thermo-chemical and electromagnetic effects, the governing equations consist of the conservation of mass, linear momentum and angular momentum. The equations for the conservation of mass in the Eulerian form are [128],

$$\frac{\partial \rho_f}{\partial t} + div\left(\rho_f \boldsymbol{v}_f\right) = 0 \tag{5.1}$$

$$\frac{\partial \rho_s}{\partial t} + div(\rho_s \boldsymbol{v}_s) = 0 \tag{5.2}$$

where $\frac{\partial}{\partial t}$ is the derivative with respect to time, *div* is the divergence operator, the subscript 'f' refers to the fluid (plasma) phase, and 's' to the solid particles (the RBC) phase, where $\rho_f = (1-\phi)\rho_{f0}, \rho_s = \phi\rho_{s0}$, ρ_{f0} and ρ_{s0} are the pure density of the plasma and the RBCs in the reference configuration, respectively, ϕ is the volume fraction (hematocrit) of RBCs and $\boldsymbol{v}$ is the velocity field. The balance of the linear momentum can be written as,

$$\rho_f \frac{D^f \boldsymbol{v}_f}{Dt} = div\left(\boldsymbol{T}_f\right) + \rho_f \boldsymbol{b}_f + \boldsymbol{f}_I \tag{5.3}$$

$$\rho_s \frac{D^s \boldsymbol{v}_s}{Dt} = div(\boldsymbol{T}_s) + \rho_s \boldsymbol{b}_s - \boldsymbol{f}_I \tag{5.4}$$

where in general for any scalar β, $\frac{D^\alpha \beta}{Dt} = \frac{\partial \beta}{\partial t} + \boldsymbol{v}^\alpha \cdot grad\beta, \alpha = f, s$, and (for any vector $\boldsymbol{w}$), $\frac{D^\alpha \boldsymbol{w}}{Dt} = \frac{\partial \boldsymbol{w}}{\partial t} + (\text{grad}\boldsymbol{w})\boldsymbol{v}^\alpha$, where 'grad' is the gradient operator, $\boldsymbol{T}_f$ and $\boldsymbol{T}_s$stand for the Cauchy stress tensors for the plasma and the RBCs, respectively, $\mathbf{f_I}$ represents the interaction forces (exchange of momentum) between the components, and $\boldsymbol{b}_f$ and $\boldsymbol{b}_s$ refer to the body forces. The balance of the angular momentum implies that, in the absence of couple stresses, the total Cauchy stress tensor is symmetric. The above relations for ρ_f and ρ_s follow from the definition of mixture density, i.e., $\rho_{mix} = \rho_1 + \rho_2$ and the 'volume additivity constraint'. This puts a restriction on the motion of the mixture [135], where it is assumed that the volume of the mixture is the sum of the volumes of the individual constituents in their reference configurations. A mixture stress tensor can be defined as [136]: $\boldsymbol{T}_m = \boldsymbol{T}_1 + \boldsymbol{T}_2$, where, $\boldsymbol{T}_1 = (1-\phi)\boldsymbol{T}_f$ and $\boldsymbol{T}_2 = \phi\boldsymbol{T}_s$, so that the mixture stress tensor reduces to that of a pure fluid as $\phi \rightarrow 1$. Obviously

this is an idealization. At a certain ϕ_m called the maximum packing fraction, the particles are in such a close proximity to each other that unless they are crushed or deformed, ϕ can no longer change. Therefore, in the numerical solution to all the practical problems of interest, we have to set certain limits or restrictions on ϕ so that ϕ can never be greater than ϕ_m.

To close these equations, constitutive relations are needed for the individual stress tensors and for the interaction force. These are described in the following section.

5.2.2 Constitutive equations

Mathematically, the purpose of the constitutive relations is to provide connections between kinematic, mechanical, and thermal fields that are compatible with the balance equations and that, in conjunction with them, provide a theory that is useful and solvable for properly posed problems. Deriving constitutive relations for the stress tensors and the interaction forces are among the outstanding issues of research in multiphase flows. The non-linearities in the constitutive relations give rise to a host of interesting problems from a computational point of view. In general, the constitutive expressions for $\boldsymbol{T}_f$ and $\boldsymbol{T}_s$ depend on the kinematical quantities associated with both the constituents. However, we assume that $\boldsymbol{T}_s$ and $\boldsymbol{T}_f$ depend only on the kinematical quantities associated with the solid and fluid phases, respectively. This assumption is sometimes called "the principle of phase separation" and was first put forward by Adkins [137, 138]. In this chapter, we assume that the plasma behaves as a linear viscous fluid

$$\boldsymbol{T}_f = \left[-p(1-\phi) + \lambda_f(1-\phi)tr\boldsymbol{D}_f\right]\boldsymbol{I} + 2\mu_f(1-\phi)\boldsymbol{D}_f \tag{5.5}$$

where p is the pressure of the mixture, λ_f and μ_f are the (constant) first and second coefficients of viscosity of the pure plasma, where $\boldsymbol{D}_f = \frac{1}{2}\left[\left(grad\ \boldsymbol{v_f}\right) + \left(grad\ \boldsymbol{v_f}\right)^T\right]$, '*tr*' stands for the trace of a second order tensor, and $\boldsymbol{I}$ is the identity tensor. (See [61, 66] for more details). The

RBCs are assumed to behave as a shear-thinning fluid, whose viscosity is also a function of the volume fraction,

$$\boldsymbol{T}_s = [-p\phi + \beta_{20}(\phi + \phi^2)tr\boldsymbol{D}_s]\boldsymbol{I} + \mu_s(\phi, tr\boldsymbol{D}_s)\phi\boldsymbol{D}_s \tag{5.6}$$

$$\mu_s(\phi, tr\boldsymbol{D}_s)\phi = \left(\mu_\infty(\phi) + \left(\mu_0(\phi) - \mu_\infty(\phi)\right)\frac{1 + ln\left(1 + k(\phi)\left(2tr\boldsymbol{D}_s{}^2\right)^{1/2}\right)}{1 + k(\phi)\left(2tr\boldsymbol{D}_s{}^2\right)^{1/2}}\right) \tag{5.7}$$

The material parameters, μ_0, μ_∞ and k are assumed to depend on ϕ in the form of polynomial function and β_{20} is a constant. The mixture viscosity is assumed to be the weighted sum:

$$\mu_{mix} = \mu_f(1 - \phi) + \mu_s\phi \tag{5.8}$$

These equations are calibrated based on experimental measurements of viscosity of suspensions of RBCs in ACD-plasma reported by Brooks [134](See Figure 5.1).

$$\mu_0 = 537.002\phi^3 + 55.006\phi^2 - 0.129\phi \tag{5.9a}$$

$$\mu_\infty = 27.873\phi^3 - 21.218\phi^2 + 14.439\phi \tag{5.9b}$$

$$k = 11 \tag{5.9c}$$

It is noted that equations (5.9a) and (5.9b) imply that the viscosity of RBCs approaches zero when the hematocrit approaches zero. The value of the k is suggested by Yeleswarapu et al. [139]. Compared with the correlations used by Jung and Hassanein [120] and Wu et al. [140], considering the larger set of experimental data used here, this correlation is better for studying the problem when the hematocrit is relatively low, for example blood flow in micro-scale vessel where the hematocrit is about 20%.

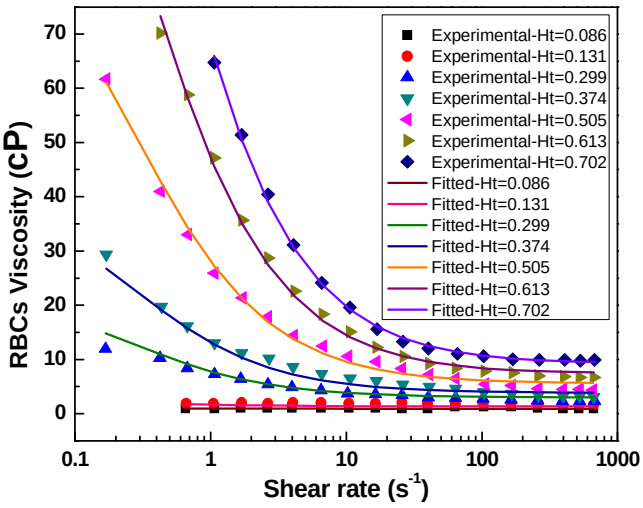

Figure 5.1 RBCs viscosity as a function of the shear rate. Experimental data is by Brooks [134].

For the interaction force between the two components, we only consider terms which would correspond to the Stokes drag force and Saffman's shear- lift force. [94, 141]

$$\boldsymbol{f}_I = \frac{9\mu_f}{2a^2} f(\phi)(\boldsymbol{v}_s - \boldsymbol{v}_f) + \frac{3(6.46)(\rho_f \mu_f)^{1/2}}{4\pi a} \phi (2tr\boldsymbol{D}_f{}^2)^{-1/4} \boldsymbol{D}_f (\boldsymbol{v}_s - \boldsymbol{v}_f) \tag{5.10}$$

where a is the diameter of RBCs, here assumed as $8\mu m$, and $f(\phi) = \exp(2.68\phi) + \phi^{0.43}$ is the drag model (hindrance function) measured by Rusche and Issa [72]. For more discussions on the interaction force, see [66, 132].

5.3 Results and Discussion

In this section, several problems are studied numerically. Comparisons between the numerical and the experimental data are presented for the velocity and the volume fraction profiles. The velocity and the volume fraction fields are, in general, given by:

$$\begin{cases} \boldsymbol{v}_f = v_{fx}(x,y,z;t)\boldsymbol{e_x} + v_{fy}(x,y,z;t)\boldsymbol{e_y} + v_{fz}(x,y,z;t)\boldsymbol{e_z} \\ \boldsymbol{v}_s = v_{sx}(x,y,z;t)\boldsymbol{e_x} + v_{sy}(x,y,z;t)\boldsymbol{e_y} + v_{sz}(x,y,z;t)\boldsymbol{e_z} \\ \phi = \phi(x,y,z;t) \end{cases} \tag{5.11}$$

Using equation (5.11), substituting equations (2.4) ~ (5.10) into equations (5.3) and (5.4), the momentum equations in the vectorial form are obtained (here we have assumed that both phases are incompressible). For the plasma phase,

$$(1-\phi)\rho_f\left[\frac{\partial \boldsymbol{v}_f}{\partial t}+(grad\ \boldsymbol{v}_f)\boldsymbol{v}_f\right]$$
$$=-grad\big((1-\phi)\,p\big)+div\left(2\mu_f(1-\phi)\boldsymbol{D}_f\right)+\rho_f(1-\phi)\boldsymbol{b}_f \tag{5.12}$$
$$+\frac{9\mu_f}{2a^2}f(\phi)\big(\boldsymbol{v}_s-\boldsymbol{v}_f\big)+\frac{3(6.46)\big(\rho_f\mu_f\big)^{1/2}}{4\pi a}\phi\big(2tr\boldsymbol{D}_f{}^2\big)^{-1/4}\boldsymbol{D}_f\big(\boldsymbol{v}_s-\boldsymbol{v}_f\big)$$

For the RBCs phase,

$$\phi\rho_s\left[\frac{\partial \boldsymbol{v}_s}{\partial t}+(grad\ \boldsymbol{v}_s)\boldsymbol{v}_s\right]$$
$$=-grad(\phi p)+div\left(\left(\mu_\infty(\phi)+\big(\mu_0(\phi)-\mu_\infty(\phi)\big)\frac{1+ln\left(1+k\big(2tr\boldsymbol{D}_s{}^2\big)^{1/2}\right)}{1+k\big(2tr\boldsymbol{D}_s{}^2\big)^{1/2}}\right)\boldsymbol{D}_s\right) \tag{5.13}$$
$$+\rho_s\phi\boldsymbol{b}_s-\frac{9\mu_f}{2a^2}f(\phi)\big(\boldsymbol{v}_s-\boldsymbol{v}_f\big)-\frac{3(6.46)\big(\rho_f\mu_f\big)^{1/2}}{4\pi a}\phi\big(2tr\boldsymbol{D}_f{}^2\big)^{-1/4}\boldsymbol{D}_f\big(\boldsymbol{v}_s-\boldsymbol{v}_f\big)$$

A CFD solver for the mathematical model described above, i.e. equations (5.1), (5.2), (5.12), and (5.13), is developed using the solvers and the libraries of OpenFOAM®. This is a C++ toolbox for the development of customized numerical solvers, and pre-/post-processing utilities for the solution of continuum mechanics problems, including computational fluid dynamics (CFD) [95]. The details of the numerical algorithms dealing with the two-fluid (Eulerian-Eulerian) approach have been discussed in various publications (e.g. [63, 142, 143]). For all the cases studied in this chapter, we use the following values for the material properties: $\mu_f = 0.96$cP, $\rho_f = 1027\text{kg/m}^3$ and $\rho_s = 1093\text{kg/m}^3$. The boundary conditions are listed in Table 5.1 (For details see [142]).

Boundary	Pressure	Velocity	Volume Fraction
Inlet	Fixed flux	Fixed value	Fixed value
Outlet	Fixed value (reference)	Zero gradient	Zero gradient
Wall	Fixed flux	Fixed value (0)	Zero gradient
Symmetric Plane	symmetryPlane	symmetryPlane	symmetryPlane

Table 5.1 Boundary conditions for simulations in this study. [95, 142]

For each geometry studied, the domain was discretized as hexahedral meshes using ICEM. In each of the cases, mesh-dependence studies were performed to assure insensitivity. To save computational time and expense, for cases 4.1, 4.3 and 4.4 we have taken advantage of the symmetric characteristics of the problems; therefore the meshes used in the simulations are 1/4 of the geometries for cases 4.1 and 4.3, and 1/2 of the geometries for case 4.4.

Velocity distribution in a tubular sudden expansion channel for low inlet hematocrit

The initial benchmark problem was to reproduce the results of the classic experiment of Karino and Goldsmith [144] which entails of water and 1% hardened RBCs through a tubular sudden expansion channel (See Figure 5.2). Two flow rates were simulated, corresponding to inlet velocity of 0.0757m/s (Re=12.2) and 0.233m/s (Re=37.8). Because hardened RBCs were used for this study, the effect of deformability on viscosity was ignored. Figure 5.3 shows the resulting streamlines and the velocity fields. Figure 5.4a and Figure 5.4b show the velocity distribution along the radial line (A-B) from the center of the tube to the wall, crossing the vortex center, illustrating excellent agreement between the simulation and experimental observations.

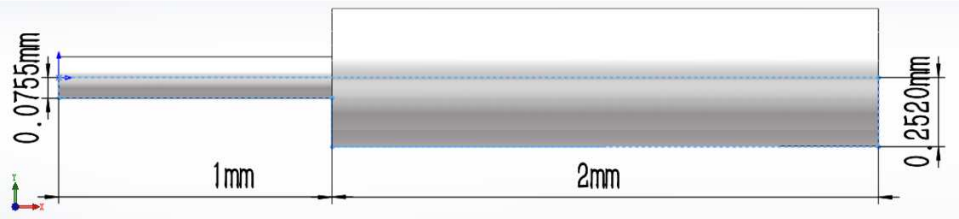

Figure 5.2. The geometry of the tubular sudden expansion channel. The radius of the tube before and after the sudden expansion is 0.0755mm and 0.252mm, and the length before and after the sudden expansion is 1mm and 2mm.

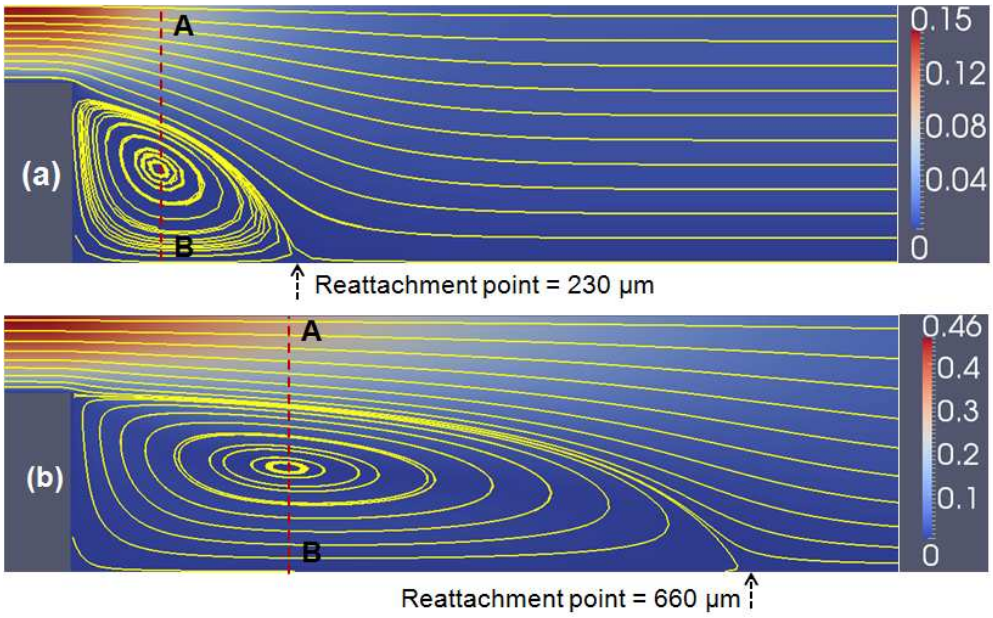

Figure 5.3. Streamlines and velocity field following sudden expansion. Re=12.2(a) and 37.8(b) respectively. The measured positions of the reattachment points are $230\mu m$ for Re=12.2 and $715\mu m$ for Re=37.8. The scale bars represent the velocity magnitude.

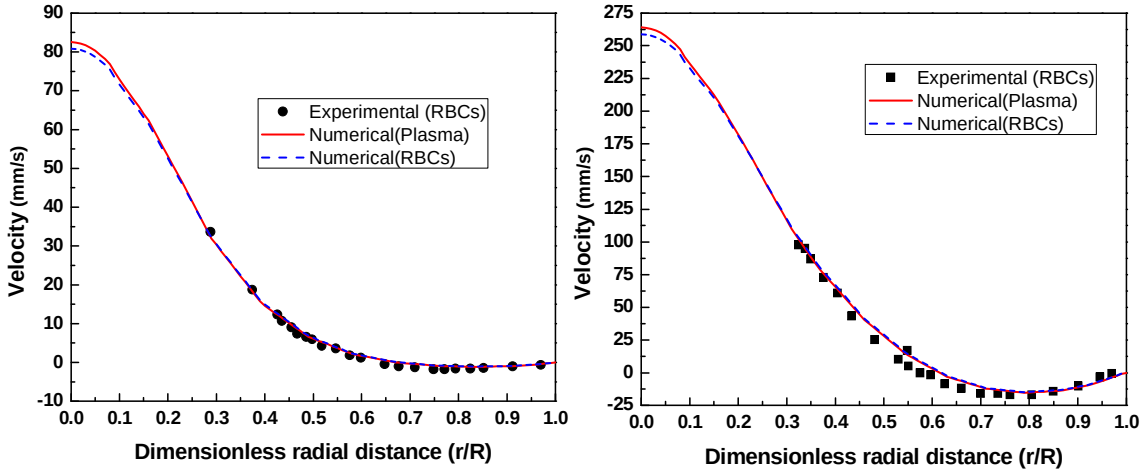

Figure 5.4. a. Velocity profile along the A-B line, when Re=12.2; b. Velocity profile along the A-B line, when Re=37.8 (Experimental data from [144])

Blood flow in a rectangular channel

The second simulation aimed to reproduce the experimental observations of Patrick et al. [145] in a rectangular micro channel. Figure 5.5 shows the cross section of the computational domain. The inlet velocity as prescribed as 350 $\mu m/s$ and the inlet hematocrit were 0.45. Figure 5.6 shows very good agreement between the numerically and experimentally obtained values of the velocity of the RBCs for the conditions of steady and fully developed flow.

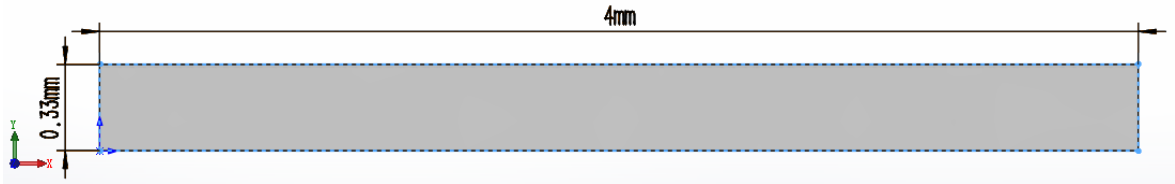

Figure 5.5. Schematic of the rectangular micro-channel, with a depth of 100 μm (z direction).

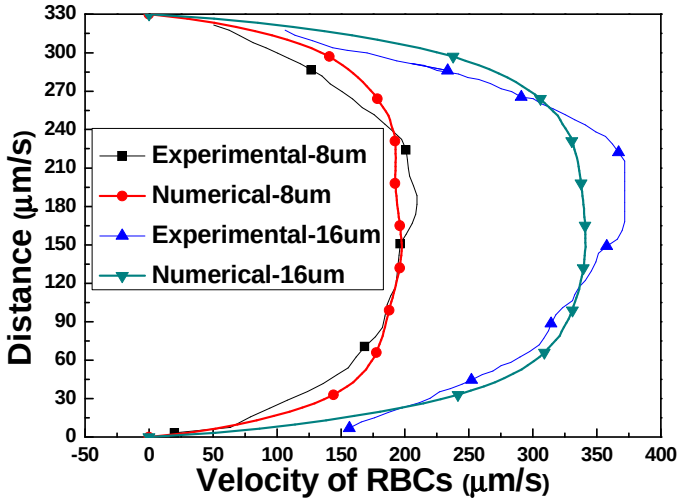

Figure 5.6. (Left) Numerical and experimental [145] streamwise (x) velocity distribution of the RBCs as a function of the distance to the wall y at the depths z=8 μm and z=16 μm.

Volume fraction distribution in a rectangular sudden expansion channel

The third benchmark study was aimed to replicate the experiments of Zhao et al. [62] involving flow of blood in a microchannel sudden expansion (See Figure 5.7). The hematocrit was prescribed to be 0.20 and the inlet velocity was 0.167m/s 0.833m/s. Figure 5.8 shows the comparison of the volume fraction of the RBCs obtained from the simulation after the flow has reached steady-state (corresponding to 0.15s and 0.035s for low flow rate and high flow rate, respectively.) To account for the finite depth-of-field of the experimental images, the numerical results shown in Figure 5.8 are averaged in the z-direction corresponding to the dimensions shown in Zhao et al. [62]. Comparison of the simulated RBC volume fraction with the microscopically observed RBC concentration reveals very good qualitative agreement, particularly with respect to the depletion zones. Comparison of simulated streamlines (Figure 3) with the experimental images also indicates similar increase in the size and intensity of the recirculation zone.

Figure 5.10 shows the results of a mesh sensitivity study for this problem. The average volume fraction profile of the RBCs is plotted as a function of mesh size (number of nodes) at t=0.035s. The profiles illustrate convergence between 68256 and 125544 nodes. Accordingly, 125544 nodes as used for all subsequent simulations to ensure accuracy.

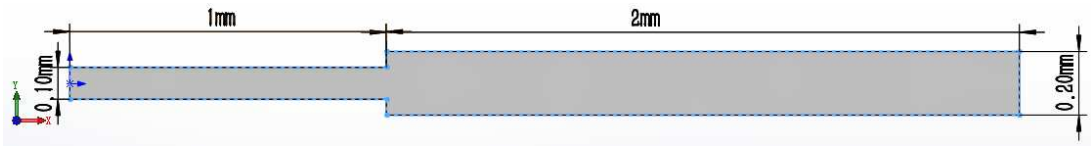

Figure 5.7. Schematic of the sudden expansion micro-channel, with a depth of 100 μm (z direction).

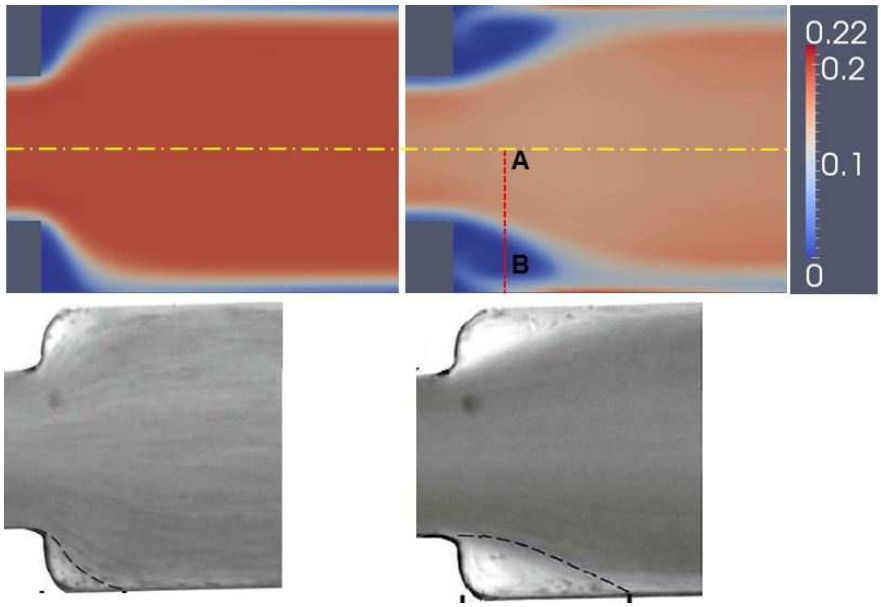

Figure 5.8. Volume fraction of the RBCs obtained from simulation (top) compared to experimental observation of Zhao et al. [62](bottom). Left: inlet velocity = 0.167 m/s; right: 0.833 m/s. Hematocrit = 0.2. The scale bar represents the volume fraction magnitude of the RBCs.

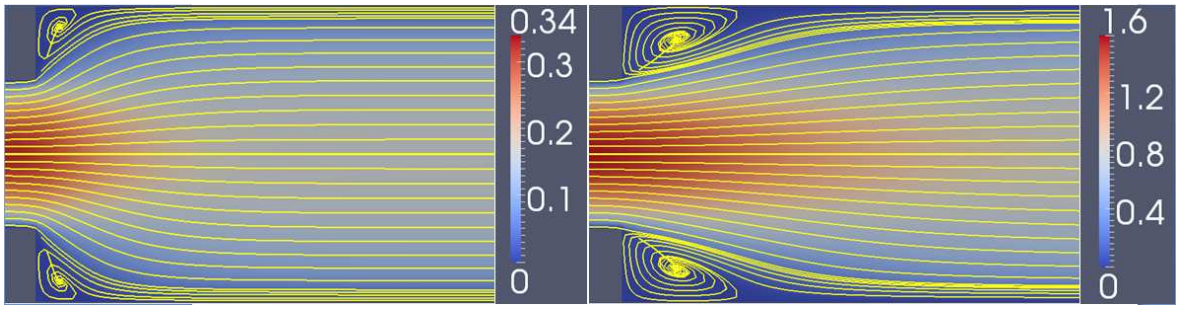

Figure 5.9 Streamline of the mixture velocity for inlet velocity = 0.167 m/s(left) and 0.833 m/s (right), at the depth z = 50μm, for hematocrit = 0.2. The scale bars represent the velocity magnitude.

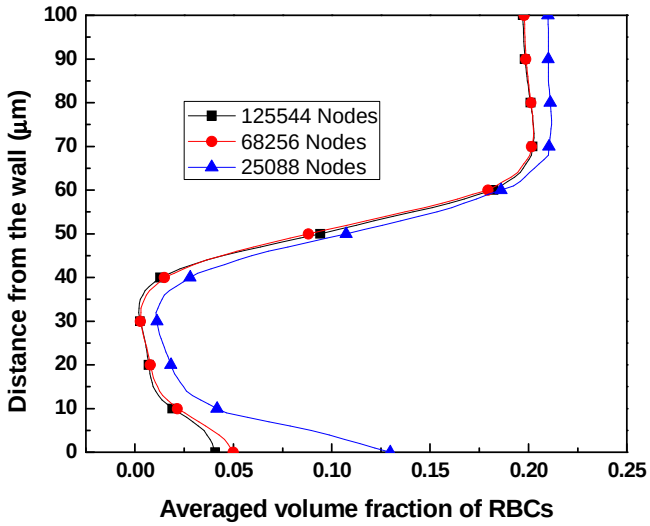

Figure 5.10. Averaged volume fraction profile of RBCs along y direction from center of the channel to the wall, at x=1.03mm (the line A-B shown in Figure 5.8), when the inlet velocity is 0.833 m/s.

Volume fraction distribution in a rectangular channel with crevices

Based on the satisfactory performance of the model on the preceding benchmark problems, a final simulation study was performed to simulate flow over a series of driven slots and crevices. This is motivated by a persistent problem involved in most blood wetted devices, namely the seams and joints between component parts of a device or flow circuit which are predisposed to thrombus deposition (See Figure 5.11). For this case, the inlet hematocrit was prescribed to be 0.40 and the inlet velocity was 0.0238 m/s. Figure 5.12 shows the comparison of the volume

fraction for the RBCs after the flow has reached the steady-state condition (simulated for 7s.). The numerical field was averaged along the z-direction similar to the previous case to account for depth-of-field of the experimental images.

These results are juxtaposed to microscopic images obtained using the method of Zhao et al. [62] in microchannels of the same dimensions, and under similar conditions. Briefly, platelets-sized fluorescent particles (3 μm, Duke Scientific) was added to a suspension of RBC ghost cells (hematocrit = 40%) in a ratio of approximately 1:10. The sample solution was delivered by syringe pump (Harvard PHD) at the prescribed flow rate, corresponding to the velocity indicated above in the simulations. The fluorescence signal was captured by a sensitive, high-resolution CCD camera (SensiCam-QE, Cooke Corp). The qualitative agreement between simulation and experiment is readily apparent. In particular, both results reveal a deficit of RBCs in the depths of the narrow crevices and slots, see Figure 5.12 (a) (e) (f) and (g). Counter-rotating recirculation bubbles were also apparent in the crevices of Figure 5.12 (c) (d) and (h) adjacent to the main flow path. (See also video examples in supplemental materials.) Further detail is provided in Figure 5.13 which indicates the streamlines and RBCs volume fraction field in the deep rectangular crevice shown in Figure 6c.

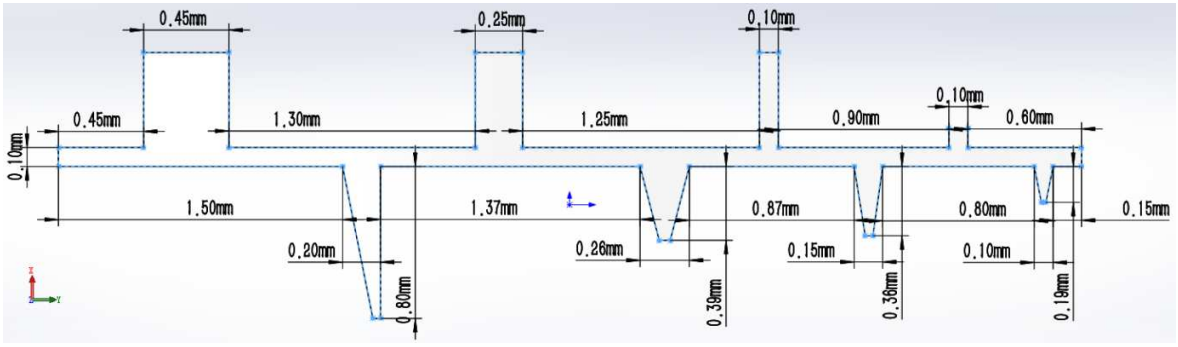

Figure 5.11. Schematic of the channel with deep gaps, with a depth of 70 μm (z direction).

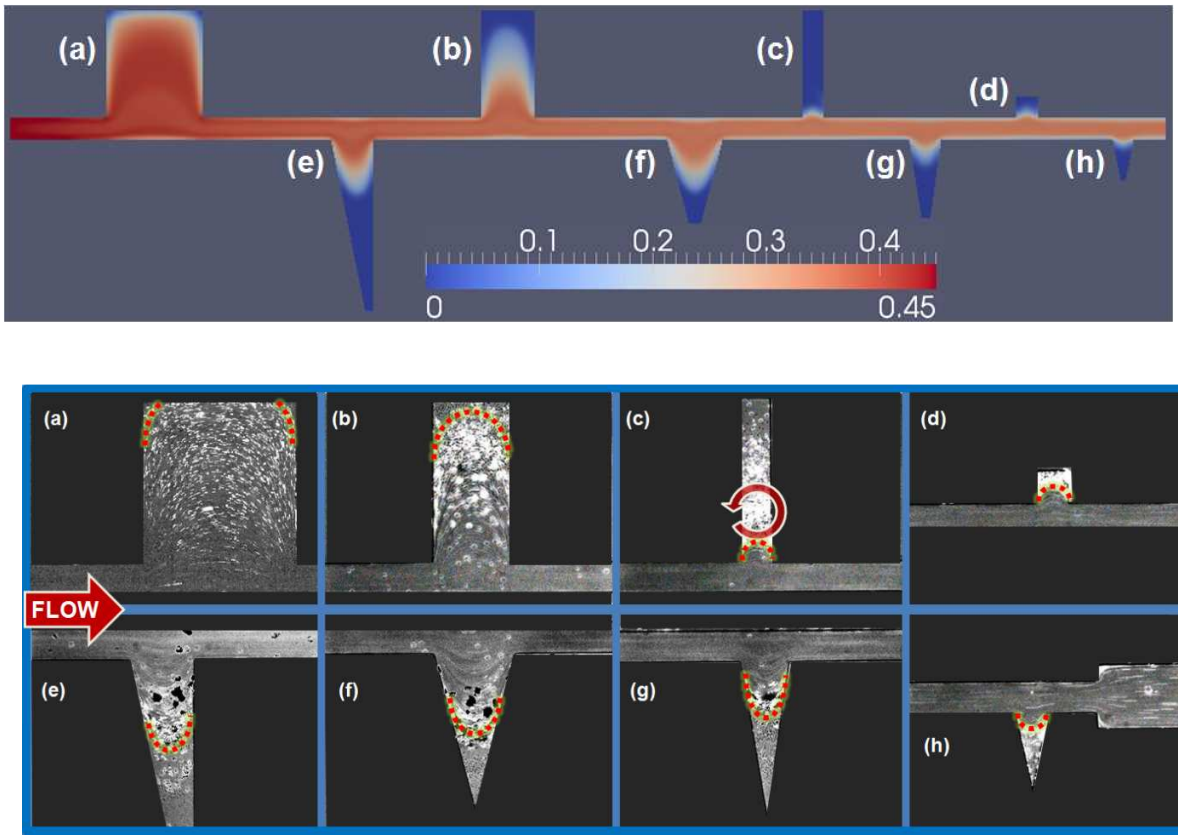

Figure 5.12. Volume fraction of the RBCs obtained from simulation (top) compared with experimental observations of RBC ghosts seeded with 3µm fluorescent particles (bottom). Both simulation and experiment correspond to inlet velocity = 0.0238 m/s and hematocrit = 0.4. Occasionally a portion of RBCs and fluorescent particles (bright points) are observed to deviate from the main stream and migrate into the depths of the crevices, and become trapped. The highly bright regions correspond to concentrated accumulation of fluorescent particles. (Additional details can be seen in the videos provided in the supplemental materials.) The scale bar represents the volume fraction magnitude of the RBCs.

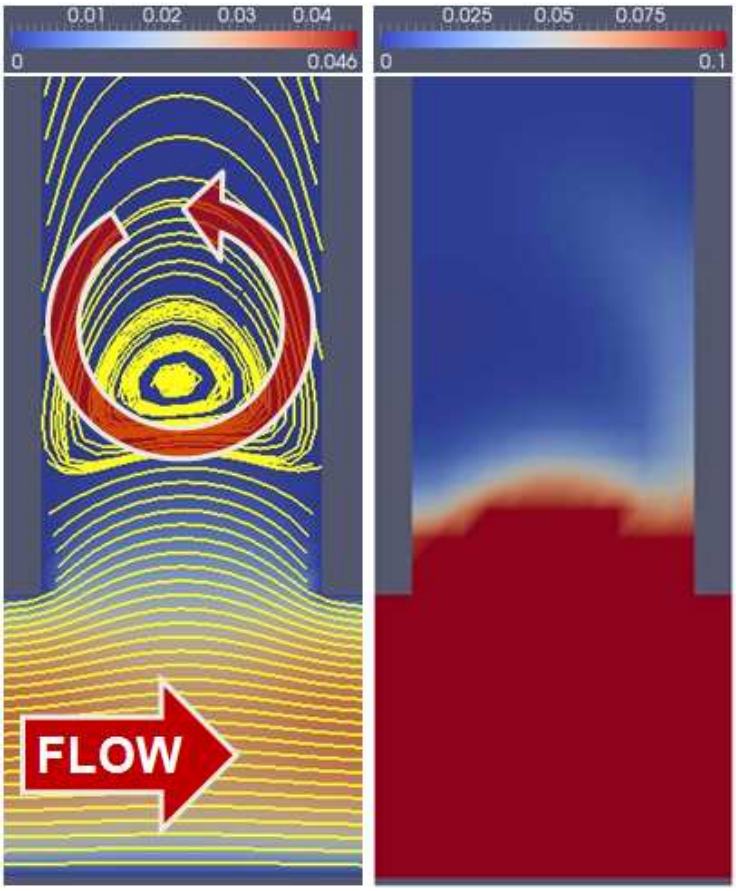

Figure 5.13. Simulated streamlines (A) and volume fraction (B) in crevice of Figure 6c, at depth z= 35 μm. The scale bars represent the velocity magnitude (A) and the volume fraction magnitude of the RBCs(B).

5.4 Summary

In this chapter, the multiphase characteristics of blood flow are studied using a two-fluid approach. The mathematical model is developed based on the framework of the mixture theory, and the model is solved numerically by a CFD solver built based on OpenFOAM®. The mathematical model is applied to several benchmark problems and compared favorably with the available experimental data. In particular, the value of the model was illustrated by the accurate prediction of volume fraction distribution of RBCs – which is essential for developing a

predictive model for thrombus in blood-wetted devices. This represents the ongoing and future objectives of this research.

Chapter 6 Summary and future work

6.1 Summary

Malaria infected RBCs separation

A malaria infected RBCs (pRBCs) separation system, mPharesis™ (magnetic aphaeresis) system, is studied and channels with constriction/constrictions. The CFD-DEM approach is applied to model the problem. Through the study, we found that because the magnitude of magnetic force decays very quickly as the distance between the pRBCs and magnet increases, therefore using the channel without any design, namely the rectangular channel, only has a little improvement on the pRBCs separation. But when the constriction is added, which enforces the pRBCs to experience larger magnetic force field, and diffuser, which reduces the re-mixing at the outlet of constriction, the separation efficiency highly increases. Therefore it should be emphasized that the channel with a diffuser after a constriction can be a promising design for practical design.

Thrombus model development and thrombus growth in an axial blood pump

Then based on the model by Sorensen**,** a thrombus model which incorporates the thrombus-blood interaction, shear induced platelets activation, shear induced platelets embolization and deposited platelets stabilization, is developed. Based on the mathematical model, a CFD solver based on OpenFOAM® is developed. Using the developed solver, some specific problems, such as thrombus formation in blood vessel and channel with crevice et al., are studied. Good agreements between the experimental date and numerical results confirm the validation of our thrombus model. Applying the mathematical model in chapter 3, we successfully directly predicted the thrombus growth in blood pump. The simulation results agree with the clinical

observation very well: most thrombus accumulated at the rear of inlet straightener vane and inlet part of impeller. Due to the expensive computational expense of the model developed in chapter 3, which is a disadvantage for engineering application, a dimensionality-reduced model is developed. Through study, the dimensionality-reduced model also shows good ability to predict the thrombus deposition in blood pump, which implies it is a promising tool for thrombus related engineering application.

Multiphase modeling of blood flow

A two-phase model of blood flow using mixture theory is formulated and validated by applying the model to study some fundamental problems and comparing with existing experimental data. Based on the two-phase model, a mathematical model of thrombus growth also has been developed. Using mixture theory, in current work, blood flow is treated as a two phase system, where the RBCs are modeled as a non-Newtonian fluid, which not only considers the effects of volume fraction (hematocrit) but also has a viscosity which depends on the shear rate, and plasma is assumed to behave as a linear viscous fluid. Based on some experimental data, a new correlation of the viscosity of the RBCs is fitted. A three dimensional CFD solver based on OpenFOAM® is developed. Applying the solver, blood flow in some fundamental geometries are studied. The numerical results exhibited good agreement with the experimental observations with respect to both the velocity field and the volume fraction distribution of RBCs. In the further, based on the velocity and volume fraction fields of RBCs got by Mixture Theory, a RBCs-platelets collision induced platelets transportation flux term can be developed for more accurately describing the platelets spatial distribution which is essential for thrombus formation.

6.2 Future work

After the platelets are activated and deposits, aggregated platelets start consolidation, which makes the aggregated platelets more stable and not embolized by hydrodynamic forces easily. This stabilization procedure is especially important for studying the problems having high shear rate. In this thesis, we also have introduced the stabilization equation for deposited platelets, but this stabilization equation only having a constant stabilization rate term is simple. Many related chemical species should be included are not considered. Therefore for improving the thrombus model, the procedure of deposited platelets stabilization will be further developed.

Furthermore, in current work thrombus in vivo are not widely studied, such as thrombus disposition on injured vessel wall and hemostasis related problems which are absolutely worth a deep study. Besides some other possible topics can be the agonists and medicines having strong effect on thrombus formation. For example, aspirin can greatly inhibit platelets activation by inhibiting the GPVI which plays a major role in collagen induced platelets activation. Studying on these agonists and medicines related problem may provide us deeper understanding on the thrombus formation and improve the model developed in current thesis.

In addition, in current thesis only the geometry of channel with crevice has been studied. In practical, many other representative geometries, see , are common in various blood wetted medical devices and vulnerable to thrombus.

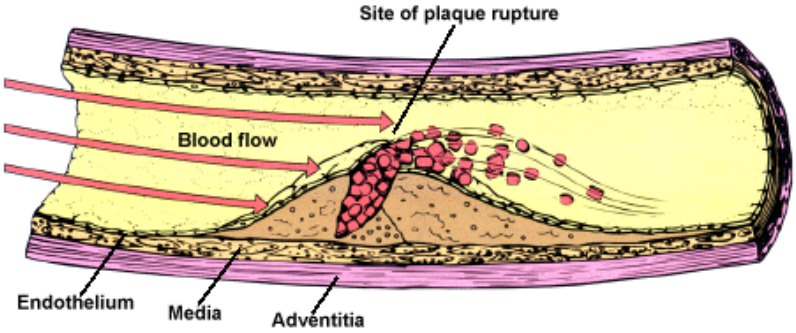

Figure 6.1Diagram of arterial thrombus responsible for acute myocardial infarction. [146]

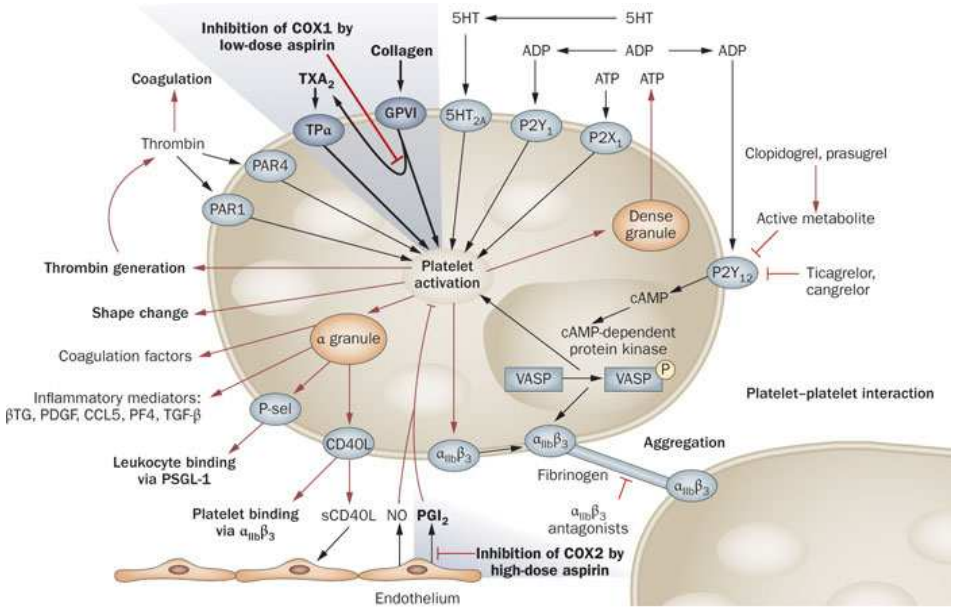

Figure 6.2 Overview of platelet activation and its inhibition by antiplatelet drugs. [147]

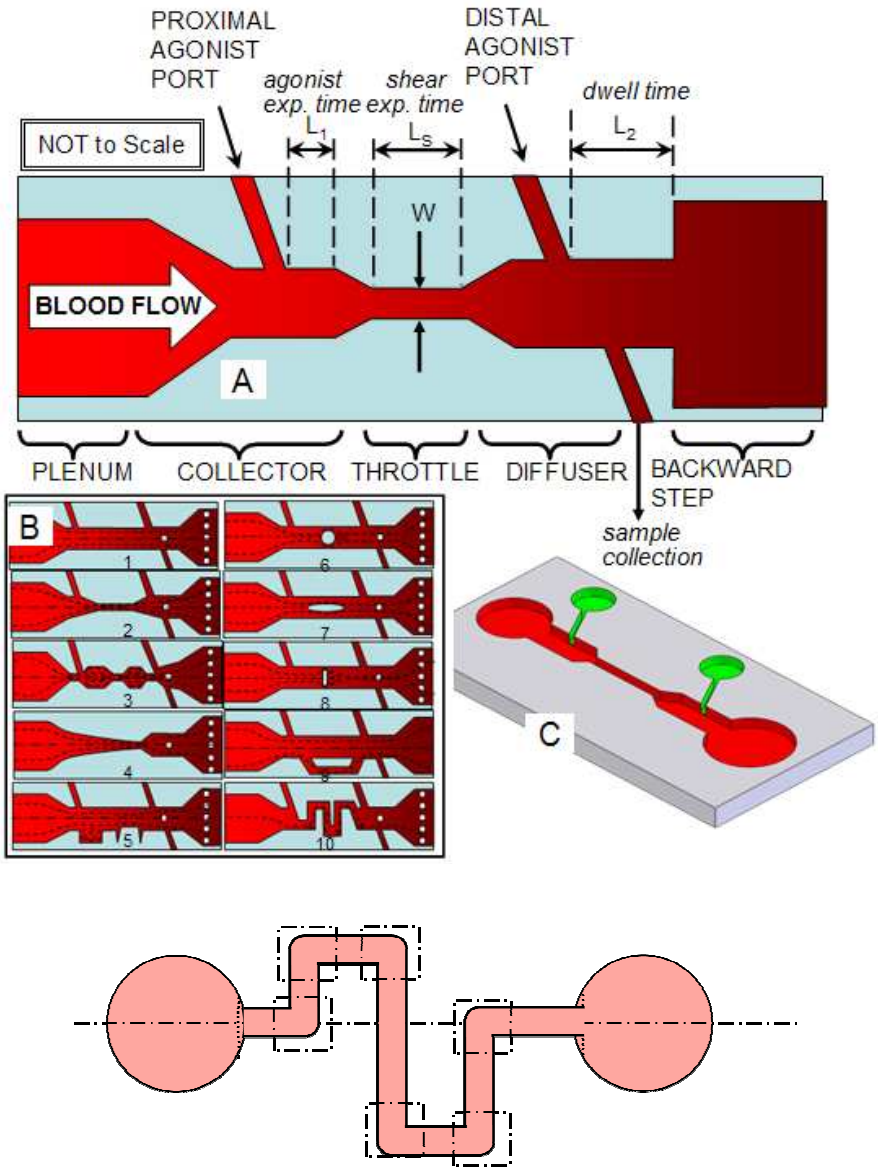

Figure 6.3 Representative geometries common in blood wetted medical devices.

References

1. Sorensen, E.N., et al., Computational simulation of platelet deposition and activation: I. Model development and properties. Ann Biomed Eng, 1999. **27**(4): p. 436-48.

2. Sorensen, E.N., et al., Computational simulation of platelet deposition and activation: II. Results for Poiseuille flow over collagen. Ann Biomed Eng, 1999. **27**(4): p. 449-58.

3. Middleman, S., Transport phenomena in the cardiovascular system. 1972: Wiley-Interscience New York.

4. Obonyo, C.O., et al., In-hospital morbidity and mortality due to severe malarial anemia in western Kenya. The American journal of tropical medicine and hygiene, 2007. **77**(6 Suppl): p. 23-28.

5. Snow, R.W., et al., Relation between severe malaria morbidity in children and level of Plasmodium falciparum transmission in Africa. The Lancet, 1997. **349**(9066): p. 1650-1654.

6. Campagna, A.M. and M.M. Patnaik, Advances in global biotechnology and local resources to treat malaria. Minnesota medicine, 2009. **92**(2): p. 44-45.

7. Trampuz, A., et al., Clinical review: Severe malaria. CRITICAL CARE-LONDON-, 2003. **7**(4): p. 315-323.

8. Genton, B. and V. D'Acremont, Clinical features of malaria in returning travelers and migrants. Travelers' malaria. Hamilton: BC, Ontario, Canada, Decker, 2001: p. 371-92.

9. Van Genderen, P.J., et al., Efficacy and safety of exchange transfusion as an adjunct therapy for severe Plasmodium falciparum malaria in nonimmune travelers: a 10-year single-center experience with a standardized treatment protocol. Transfusion, 2010. **50**(4): p. 787-794.

10. Paul, F., et al., Separation of malaria-infected erythrocytes from whole blood: use of a selective high-gradient magnetic separation technique. The Lancet, 1981. **318**(8237): p. 70-71.

11. Nilsson, L., Malaria parasites infect two blood cells. 2012, SMITHSONIAN MAGAZINE.

12. Vyas, J.M., Malaria transmission cycle. 2013, U.S. National Library of Medicine.

13. Epstein, F.H., et al., The pathogenesis of coronary artery disease and the acute coronary syndromes. New England journal of medicine, 1992. **326**(4): p. 242-250.

14. Fuster, V., et al., Insights into the pathogenesis of acute ischemic syndromes. Circulation, 1988. **77**(6): p. 1213-1220.

15. Cito, S., M.D. Mazzeo, and L. Badimon, A review of macroscopic thrombus modeling methods. Thrombosis research, 2013. **131**(2): p. 116-124.

16. Merino, A., et al., Echocardiographic “smoke” is produced by an interaction of erythrocytes and plasma proteins modulated by shear forces. Journal of the American College of Cardiology, 1992. **20**(7): p. 1661-1668.

17. Badimon, L., R.F. Storey, and G. Vilahur, Update on lipids, inflammation and atherothrombosis. Thrombosis and haemostasis, 2011. **105**(1): p. S34.

18. Patrono, C., et al., Antiplatelet agents for the treatment and prevention of atherothrombosis. European heart journal, 2011. **32**(23): p. 2922-2932.

19. Kirklin, J.K., et al., The fourth INTERMACS annual report: 4,000 implants and counting. The Journal of Heart and Lung Transplantation, 2012. **31**(2): p. 117-126.

20. Slaughter, M.S., et al., Advanced heart failure treated with continuous-flow left ventricular assist device. New England Journal of Medicine, 2009. **361**(23): p. 2241-2251.

21. Hund, S.J., A Computational Model of Platelet Mediated Thrombosis for the Evaluation and Design of Medical Devices. 2010, Carnegie Mellon University.

22. Patnaik, J.L., et al., Cardiovascular disease competes with breast cancer as the leading cause of death for older females diagnosed with breast cancer: a retrospective cohort study. Breast Cancer Res, 2011. **13**(3): p. R64.

23. Lloyd-Jones, D., et al., Heart disease and stroke statistics—2010 update A report from the American Heart Association. Circulation, 2010. **121**(7): p. e46-e215.

24. Mauthner, O., et al., Life on the Heart Transplant Waiting List: Life on Hold? Life at All? The Journal of Heart and Lung Transplantation, 2013. **32**(4, Supplement): p. S196.

25. Levin, R.L., et al., Systemic Ventricular Assistance Using a HeartMate 2 Device as Bridge to Transplant in a Congenitally Corrected Transposition of the Great Vessels. 2012. Vol. 80. 2012.

26. Rose, E.A., et al., Long-term use of a left ventricular assist device for end-stage heart failure. New England Journal of Medicine, 2001. **345**(20): p. 1435-1443.

27. Griffith, B.P., et al., HeartMate II left ventricular assist system: from concept to first clinical use. The Annals of Thoracic Surgery, 2001. **71**(3, Supplement 1): p. S116-S120.

28. Song, X., et al., Computational Fluid Dynamics Prediction of Blood Damage in a Centrifugal Pump. Artificial Organs, 2003. **27**(10): p. 938-941.

29. Starling, R.C., et al., Unexpected Abrupt Increase in Left Ventricular Assist Device Thrombosis. New England Journal of Medicine, 2014. **370**(1): p. 33-40.

30. Wang, Y., et al., Decision tree for adjuvant right ventricular support in patients receiving a left ventricular assist device. The Journal of heart and lung transplantation, 2012. **31**(2): p. 140-149.

31. Almond, C.S., et al., The Berlin Heart EXCOR® pediatric ventricular assist device for bridge to heart transplantation in US children. Circulation, 2013: p. CIRCULATIONAHA. 112.000685.

32. Yamazaki, K., et al., An implantable centrifugal blood pump for long term circulatory support. ASAIO Journal, 1997. **43**(5): p. M691.

33. Macha, M., et al., Survival for up to six months in calves supported with an implantable axial flow ventricular assist device. ASAIO journal, 1997. **43**(4): p. 311-315.

34. Najib, M.Q., et al., An unusual presentation of left ventricular assist device thrombus. European Heart Journal-Cardiovascular Imaging, 2012: p. jes011.

35. Adams, P.C., et al., Platelet/vessel wall interactions, rheologic factors and thrombogenic substrate in acute coronary syndromes: preventive strategies. Am J Cardiol, 1987. **60**(12): p. 9G-16G.

36. Badimon, L., et al., Thrombosis: Studies under flow conditions. Annals of the New York Academy of Sciences, 1987. **516**(1): p. 427-540.

37. Badimon, L., et al., Characterization of a tubular flow chamber for studying platelet interaction with biologic and prosthetic materials: deposition of indium 111-labeled platelets on collagen, subendothelium, and expanded polytetrafluoroethylene. The Journal of laboratory and clinical medicine, 1987. **110**(6): p. 706-718.

38. Merino, A., et al., Synergistic action of severe wall injury and shear forces on thrombus formation in arterial stenosis: definition of a thrombotic shear rate threshold. Journal of the American College of Cardiology, 1994. **24**(4): p. 1091-1097.

39. Sing, C.E. and A. Alexander-Katz, Elongational flow induces the unfolding of von Willebrand factor at physiological flow rates. Biophysical journal, 2010. **98**(9): p. L35-L37.

40. Skorczewski, T., L.C. Erickson, and A.L. Fogelson, Platelet motion near a vessel wall or thrombus surface in two-dimensional whole blood simulations. Biophysical journal, 2013. **104**(8): p. 1764-1772.

41. AlMomani, T., et al., Micro-scale dynamic simulation of erythrocyte–platelet interaction in blood flow. Annals of biomedical engineering, 2008. **36**(6): p. 905-920.

42. Goldsmith, H. and V. Turitto, Rheological aspects of thrombosis and haemostasis: basic principles and applications. ICTH-Report-Subcommittee on Rheology of the International Committee on Thrombosis and Haemostasis. Thrombosis and haemostasis, 1986. **55**(3): p. 415-435.

43. Turitto, V.T., A.M. Benis, and E.F. Leonard, Platelet diffusion in flowing blood. Industrial & engineering chemistry fundamentals, 1972. **11**(2): p. 216-223.

44. Reasor Jr, D.A., et al., Determination of critical parameters in platelet margination. Annals of biomedical engineering, 2013. **41**(2): p. 238-249.

45. Cadroy, Y. and S.R. Hanson, Effects of red blood cell concentration on hemostasis and thrombus formation in a primate model. Blood, 1990. **75**(11): p. 2185-2193.

46. Joist, J.H., J.E. Bauman, and S.P. Sutera, Platelet adhesion and aggregation in pulsatile shear flow: effects of red blood cells. Thrombosis research, 1998. **92**(6): p. S47-S52.

47. Peerschke, E.I., et al., Ex vivo evaluation of erythrocytosis-enhanced platelet thrombus formation using the cone and plate (let) analyzer: effect of platelet antagonists. British journal of haematology, 2004. **127**(2): p. 195-203.

48. Turitto, V. and H. Weiss, Red blood cells: their dual role in thrombus formation. Science, 1980. **207**(4430): p. 541-543.

49. Robertson, A.M., A. Sequeira, and M.V. Kameneva, Hemorheology, in Hemodynamical flows. 2008, Springer. p. 63-120.

50. Thompson, L.O., M. Loebe, and G.P. Noon, What price support? Ventricular assist device induced systemic response. ASAIO journal, 2003. **49**(5): p. 518-526.

51. Marhefka, J., et al., Drag reducing polymers improve tissue perfusion via modification of the RBC traffic in microvessels. Biorheology, 2009. **46**(4): p. 281-292.

52. Carr, R.T. and L.L. Wickham, Plasma skimming in serial microvascular bifurcations. Microvascular research, 1990. **40**(2): p. 179-190.

53. Krogh, A., Studies on the physiology of capillaries: II. The reactions to local stimuli of the blood-vessels in the skin and web of the frog. The Journal of physiology, 1921. **55**(5-6): p. 412.

54. Skalak, R., N. Ozkaya, and T.C. Skalak, Biofluid mechanics. Annual review of fluid mechanics, 1989. **21**(1): p. 167-200.

55. Aidun, C.K. and J.R. Clausen, Lattice-Boltzmann method for complex flows. Annual review of fluid mechanics, 2010. **42**: p. 439-472.

56. Dupin, M.M., et al., Modeling the flow of dense suspensions of deformable particles in three dimensions. Physical Review E, 2007. **75**(6): p. 066707.

57. Zhang, J., P.C. Johnson, and A.S. Popel, Effects of erythrocyte deformability and aggregation on the cell free layer and apparent viscosity of microscopic blood flows. Microvascular research, 2009. **77**(3): p. 265-272.

58. Jung, J., A. Hassanein, and R.W. Lyczkowski, Hemodynamic computation using multiphase flow dynamics in a right coronary artery. Annals of biomedical engineering, 2006. **34**(3): p. 393-407.

59. Rajagopal, K.R., Mechanics of mixtures. 1995: World scientific.

60. Ishii, M., Thermo-fluid dynamic theory of two-phase flow. NASA STI/Recon Technical Report A, 1975. **75**: p. 29657.

61. Massoudi, M., J. Kim, and J.F. Antaki, Modeling and numerical simulation of blood flow using the theory of interacting continua. International journal of non-linear mechanics, 2012. **47**(5): p. 506-520.

62. Zhao, R., et al., Micro-flow visualization of red blood cell-enhanced platelet concentration at sudden expansion. Annals of biomedical engineering, 2008. **36**(7): p. 1130-1141.

63. Kim, J., Multiphase CFD Analysis and Shape-Optimization of Blood-Contracting Medical Devices. 2012.

64. Van der Hoef, M., et al., Multiscale modeling of gas-fluidized beds. Advances in Chemical Engineering, 2006. **31**: p. 65-149.

65. Gidaspow, D. and J. Huang, Kinetic theory based model for blood flow and its viscosity. Annals of biomedical engineering, 2009. **37**(8): p. 1534-1545.

66. Wu, W.-T., et al., A numerical study of blood flow using mixture theory. International journal of engineering science, 2014. **76**: p. 56-72.

67. Fenech, M., et al., A particle dynamic model of red blood cell aggregation kinetics. Annals of biomedical engineering, 2009. **37**(11): p. 2299-2309.

68. Chesnutt, J. and J. Marshall, Effect of particle collisions and aggregation on red blood cell passage through a bifurcation. Microvascular research, 2009. **78**(3): p. 301-313.

69. Clausen, J.R., D.A. Reasor Jr, and C.K. Aidun, Parallel performance of a lattice-Boltzmann/finite element cellular blood flow solver on the IBM Blue Gene/P architecture. Computer Physics Communications, 2010. **181**(6): p. 1013-1020.

70. Hoomans, B., et al., Discrete particle simulation of bubble and slug formation in a two-dimensional gas-fluidised bed: a hard-sphere approach. Chemical Engineering Science, 1996. **51**(1): p. 99-118.

71. Link, J., et al., Flow regimes in a spout–fluid bed: A combined experimental and simulation study. Chemical Engineering Science, 2005. **60**(13): p. 3425-3442.

72. Rusche, H. and R. Issa. The effect of voidage on the drag force on particles, droplets and bubbles in dispersed two-phase flow. in Proc. 2nd Japanese-European Two-Phase Flow Group Meeting. Tsukuba, Japan. 2000. Citeseer.

73. Cundall, P.A. and O.D. Strack, A discrete numerical model for granular assemblies. Geotechnique, 1979. **29**(1): p. 47-65.

74. McNamara, S. and W. Young, Inelastic collapse and clumping in a one-dimensional granular medium. Physics of Fluids A: Fluid Dynamics (1989-1993), 1992. **4**(3): p. 496-504.

75. Su, J., Z. Gu, and X.Y. Xu, Discrete element simulation of particle flow in arbitrarily complex geometries. Chemical Engineering Science, 2011. **66**(23): p. 6069-6088.

76. Dean, D., et al., Frictional behavior of individual vascular smooth muscle cells assessed by lateral force microscopy. Materials, 2010. **3**(9): p. 4668-4680.

77. Tsuji, Y., T. Tanaka, and T. Ishida, Lagrangian numerical simulation of plug flow of cohesionless particles in a horizontal pipe. Powder technology, 1992. **71**(3): p. 239-250.

78. Han, K.-H. and A.B. Frazier, Continuous magnetophoretic separation of blood cells in microdevice format. Journal of Applied Physics, 2004. **96**(10): p. 5797-5802.

79. Kim, J., et al., Removal of malaria-infected red blood cells using magnetic cell separators: a computational study. Applied mathematics and computation, 2012. **218**(12): p. 6841-6850.

80. Hackett, S., et al., Magnetic susceptibility of iron in malaria-infected red blood cells. Biochimica et Biophysica Acta (BBA)-Molecular Basis of Disease, 2009. **1792**(2): p. 93-99.

81. Dulińska, I., et al., Stiffness of normal and pathological erythrocytes studied by means of atomic force microscopy. Journal of biochemical and biophysical methods, 2006. **66**(1): p. 1-11.

82. Malaria, R.B., The global malaria action plan. Roll Back Malaria partnership, 2008.

83. Yin, X., T. Thomas, and J. Zhang, Multiple red blood cell flows through microvascular bifurcations: cell free layer, cell trajectory, and hematocrit separation. Microvascular research, 2013. **89**: p. 47-56.

84. Han, K.-H. and A.B. Frazier, Paramagnetic capture mode magnetophoretic microseparator for high efficiency blood cell separations. Lab on a Chip, 2006. **6**(2): p. 265-273.

85. Harrison, P., Platelet function analysis. Blood reviews, 2005. **19**(2): p. 111-123.

86. Hellums, J.D., 1993 Whitaker Lecture: biorheology in thrombosis research. Annals of biomedical engineering, 1994. **22**(5): p. 445-455.

87. Wootton, D.M. and D.N. Ku, Fluid mechanics of vascular systems, diseases, and thrombosis. Annual review of biomedical engineering, 1999. **1**(1): p. 299-329.

88. Bizzozero, J., Ueber einen neuen Formbestandtheil des Blutes und dessen Rolle bei der Thrombose und der Blutgerinnung. Archiv für pathologische Anatomie und Physiologie und für klinische Medicin, 1882. **90**(2): p. 261-332.

89. Anand, M., K. Rajagopal, and K. Rajagopal, A model incorporating some of the mechanical and biochemical factors underlying clot formation and dissolution in flowing blood: review article. Journal of Theoretical Medicine, 2003. **5**(3-4): p. 183-218.

90. Hockin, M.F., et al., A model for the stoichiometric regulation of blood coagulation. Journal of Biological Chemistry, 2002. **277**(21): p. 18322-18333.

91. Kuharsky, A.L. and A.L. Fogelson, Surface-mediated control of blood coagulation: the role of binding site densities and platelet deposition. Biophysical journal, 2001. **80**(3): p. 1050-1074.

92. Ataullakhanov, F.I. and M.A. Panteleev, Mathematical modeling and computer simulation in blood coagulation. 2005: Karger.

93. Leiderman, K. and A.L. Fogelson, Grow with the flow: a spatial–temporal model of platelet deposition and blood coagulation under flow. Mathematical Medicine and Biology, 2011. **28**(1): p. 47-84.

94. Johnson, G., M. Massoudi, and K. Rajagopal, Flow of a fluid—solid mixture between flat plates. Chemical Engineering Science, 1991. **46**(7): p. 1713-1723.

95. OpenCFD, OpenFOAM Programmer's Guide Version 2.1.0, OpenCFD, Editor. 2011, CFD online Web Site.

96. Begent, N. and G. Born, Growth rate in vivo of platelet thrombi, produced by iontophoresis of ADP, as a function of mean blood flow velocity. Nature, 1970. **227**: p. 926-930.

97. Born, G. and P. Richardson, Activation time of blood platelets. The Journal of membrane biology, 1980. **57**(2): p. 87-90.

98. Goodman, P.D., et al., Computational model of device-induced thrombosis and thromboembolism. Annals of biomedical engineering, 2005. **33**(6): p. 780-797.

99. Frojmovic, M.M., R.F. Mooney, and T. Wong, Dynamics of platelet glycoprotein IIb-IIIa receptor expression and fibrinogen binding. I. Quantal activation of platelet subpopulations varies with adenosine diphosphate concentration. Biophysical journal, 1994. **67**(5): p. 2060.

100. Richardson, P.D., Effect of blood flow velocity on growth rate of platelet thrombi. Nature, 1973. **245**: p. 103-104.

101. Krabatsch, T., et al., Ventricular assist devices for all? European Journal of Cardio-Thoracic Surgery, 2012. **42**(6): p. 918-919.

102. Snyder, T.A., et al., Leukocyte–Platelet Aggregates and Monocyte Tissue Factor Expression in Bovines Implanted With Ventricular Assist Devices. Artificial organs, 2007. **31**(2): p. 126-131.

103. Wilson, K.M., Choosing the right line for the right time. Nursing2013, 2013. **43**(12): p. 66-68.

104. LaRose, J.A., et al., Design concepts and principle of operation of the HeartWare ventricular assist system. ASAIO Journal, 2010. **56**(4): p. 285-289.

105. Krishnamani, R., D. DeNofrio, and M.A. Konstam, Emerging ventricular assist devices for long-term cardiac support. Nat Rev Cardiol, 2010. **7**(2): p. 71-76.

106. Schoephoerster, R.T. and K.B. Chandran, Velocity and turbulence measurements past mitrial valve prostheses in a model left ventricle. Journal of biomechanics, 1991. **24**(7): p. 549-562.

107. Bluestein, D., E. Rambod, and M. Gharib, Vortex Shedding as a Mechanism for Free Emboli Formation in Mechanical Heart Valves. Journal of Biomechanical Engineering, 1999. **122**(2): p. 125-134.

108. Chiu, W.-C., et al., Thromboresistance Comparison of the HeartMate II Ventricular Assist Device With the Device Thrombogenicity Emulation-Optimized HeartAssist 5 VAD. Journal of biomechanical engineering, 2014. **136**(2): p. 021014.

109. Poulter, N., Coronary heart disease is a multifactorial disease. American Journal of Hypertension, 1999. **12**(S6): p. 92S-95S.

110. Bäumler, H., et al., Basic phenomena of red blood cell rouleaux formation. Biorheology, 1999. **36**(5): p. 439-442.

111. Chien, S., Shear dependence of effective cell volume as a determinant of blood viscosity. Science, 1970. **168**(3934): p. 977-979.

112. Popel, A.S. and P.C. Johnson, Microcirculation and hemorheology. Annual review of fluid mechanics, 2005. **37**: p. 43.

113. Bagchi, P., Mesoscale simulation of blood flow in small vessels. Biophysical journal, 2007. **92**(6): p. 1858-1877.

114. Kameneva, M., et al., Red blood cell aging and risk of cardiovascular diseases. Clinical hemorheology and microcirculation, 1998. **18**(1): p. 67-74.

115. Middleman, E., J. Luce, and E. Frei, Clinical trials with adriamycin. Cancer, 1971. **28**(4): p. 844-850.

116. Rourke, M.D. and A.C. Ernstene, A method for correcting the erythrocyte sedimentation rate for variations in the cell volume percentage of blood. Journal of Clinical Investigation, 1930. **8**(4): p. 545.

117. Fahraus, R. and T. Lindqvist, The viscosity of the blood in narrow capillary tubes. American Journal of Physiology, 1931. **96**(3): p. 562-568.

118. Fahraus, R., The suspension stability of the blood. Physiological Reviews, 1929. **9**(2): p. 241-274.

119. Pan, W., et al., Predicting dynamics and rheology of blood flow: a comparative study of multiscale and low-dimensional models of red blood cells. Microvascular research, 2011. **82**(2): p. 163-170.

120. Jung, J. and A. Hassanein, Three-phase CFD analytical modeling of blood flow. Medical engineering & physics, 2008. **30**(1): p. 91-103.

121. Huang, J., R.W. Lyczkowski, and D. Gidaspow, Pulsatile flow in a coronary artery using multiphase kinetic theory. Journal of biomechanics, 2009. **42**(6): p. 743-754.

122. Rajagopal, K., On a hierarchy of approximate models for flows of incompressible fluids through porous solids. Mathematical Models and Methods in Applied Sciences, 2007. **17**(02): p. 215-252.

123. Rajagopal, K. and L. Tao, Mechanics of Mixtures, Series on Advances in Mathematics for Applied Sciences, vol. 35. 1995, World Scientific, Singapore.

124. Truesdell, C., Sulle basi della thermomeccanica. 1957: Rendiconti Lincei.

125. Truesdell, C., Rotational Thermodynamics. 2nd ed. 1984, New York: Springer-Verlag. 578.

126. Atkin, R. and R. Craine, Continuum theories of mixtures: applications. IMA Journal of Applied Mathematics, 1976. **17**(2): p. 153-207.

127. Atkin, R. and R. Craine, Continuum theories of mixtures: basic theory and historical development. The Quarterly Journal of Mechanics and Applied Mathematics, 1976. **29**(2): p. 209-244.

128. Bowen, R., Theory of Mixtures, in Continuum Physics A. Eringen, Editor. 1976, Academic Press: New York. p. 11-32.

129. Bedford, A. and D.S. Drumheller, Theories of immiscible and structured mixtures. International Journal of Engineering Science, 1983. **21**(8): p. 863-960.

130. Massoudi, M., A note on the meaning of mixture viscosity using the classical continuum theories of mixtures. International Journal of Engineering Science, 2008. **46**(7): p. 677-689.

131. Massoudi, M., A Mixture Theory formulation for hydraulic or pneumatic transport of solid particles. International Journal of Engineering Science, 2010. **48**(11): p. 1440-1461.

132. Massoudi, M. and J.F. Antaki, An anisotropic constitutive equation for the stress tensor of blood based on mixture theory. Mathematical Problems in Engineering, 2008. **2008**.

133. Wu, W.-T., N. Aubry, and M. Massoudi, On the coefficients of the interaction forces in a two-phase flow of a fluid infused with particles. International Journal of Non-Linear Mechanics, 2014. **59**: p. 76-82.

134. Brooks, D., J. Goodwin, and G. Seaman, Interactions among erythrocytes under shear. J. appl. Physiol, 1970. **28**(2).

135. Mills, N., Incompressible mixtures of Newtonian fluids. International Journal of Engineering Science, 1966. **4**(2): p. 97-112.

136. Green, A.E. and P.M. Naghdi, On basic equations for mixtures. The Quarterly Journal of Mechanics and Applied Mathematics, 1969. **22**(4): p. 427-438.

137. Adkins, J., Non-linear diffusion II. Constitutive equations for mixtures of isotropic fluids. Philosophical Transactions of the Royal Society of London. Series A, Mathematical and Physical Sciences, 1963. **255**(1064): p. 635-648.

138. Adkins, J.E., Non-linear diffusion i. diffusion and flow of mixtures of fluids. Philosophical Transactions of the Royal Society of London. Series A, Mathematical and Physical Sciences, 1963. **255**(1064): p. 607-633.

139. Yeleswarapu, K.K., et al., A Mathematical Model for Shear-Induced Hemolysis. Artificial Organs, 1995. **19**(7): p. 576-582.

140. Wu, W.-T., N. Aubry, and M. Massoudi. Channel flow of a mixture of granular materials and a fluid. in ASME 2013 International Mechanical Engineering Congress and Exposition. 2013. American Society of Mechanical Engineers.

141. Massoudi, M., Constitutive relations for the interaction force in multicomponent particulate flows. International Journal of Non-Linear Mechanics, 2003. **38**(3): p. 313-336.

142. Rusche, H., Computational fluid dynamics of dispersed two-phase flows at high phase fractions. 2003, Imperial College London (University of London).

143. Weller, H., Derivation, modelling and solution of the conditionally averaged two-phase flow equations. 2002, Technical Report TR/HGW/02, Nabla Ltd.

144. Karino, T. and H. Goldsmith, Flow behaviour of blood cells and rigid spheres in an annular vortex. Philosophical Transactions of the Royal Society of London. B, Biological Sciences, 1977. **279**(967): p. 413-445.

145. Patrick, M.J., et al., Cellular-level near-wall unsteadiness of high-hematocrit erythrocyte flow using confocal μPIV. Experiments in fluids, 2011. **50**(4): p. 887-904.

146. Califf, R.M., Acute myocardial infarction and other acute ischemic syndromes. Vol. 8. 2001: Current Medicine.

147. Pignone, M. and C.D. Williams, Aspirin for primary prevention of cardiovascular disease in diabetes mellitus. Nature Reviews Endocrinology, 2010. **6**(11): p. 619-628.